bioRxiv preprint first posted online May. 15, 2019; doi: http://dx.doi.org/10.1101/639898. The copyright holder for this preprint (which was not peer-reviewed) is the author/funder, who has granted bioRxiv a license to display the preprint in perpetuity. It is made available under a CC-BY 4.0 International license.

A comparative epigenome analysis of gammaherpesviruses suggests cis-acting sequence features as critical mediators of rapid polycomb recruitment

Thomas Günther[1], Jacqueline Fröhlich[1], Christina Herrde[1], Shinji Ohno[2,#a], Lia Burkhardt[1], Heiko Adler[2*], Adam Grundhoff[1,*]

[1] Heinrich Pette Institute, Leibniz Institute for Experimental Virology, Hamburg, Germany

[2] Comprehensive Pneumology Center, Research Unit Lung Repair and Regeneration, Helmholtz Zentrum München - German Research Center for Environmental Health (GmbH), Munich, Germany, and University Hospital Grosshadern, Ludwig-Maximilians-University, Munich, Germany; Member of the German Center of Lung Research (DZL)

[#a]current address: Department of Virology, Graduate School of Medicine, University of the Ryukyus, Okinawa, Japan

[*] Corresponding authors

E-mail: adam.grundhoff@hpi.uni-hamburg.de (AG), h.adler@helmholtz-muenchen.de (HA)

Running Title: Polycomb recruitment by gammaherpesvirus genomes

bioRxiv preprint first posted online May. 15, 2019; doi: http://dx.doi.org/10.1101/639898. The copyright holder for this preprint (which was not peer-reviewed) is the author/funder, who has granted bioRxiv a license to display the preprint in perpetuity. It is made available under a CC-BY 4.0 International license.

Abstract

Latent Kaposi sarcoma-associated herpesvirus (KSHV) genomes rapidly acquire distinct patterns of the activating histone modification H3K4-me3 as well as repressive H3K27-me3 marks, a modification linked to transcriptional silencing by polycomb repressive complexes (PRC). Interestingly, PRCs have recently been reported to restrict viral gene expression in a number of other viral systems, suggesting they may play a broader role in controlling viral chromatin. If so, it is an intriguing possibility that latency establishment may result from viral subversion of polycomb-mediated host responses to exogenous DNA.

To investigate such scenarios we sought to establish whether rapid repression by PRC constitutes a general hallmark of herpesvirus latency. For this purpose, we performed a comparative epigenome analysis of KSHV and the related murine gammaherpesvirus 68 (MHV-68). We demonstrate that, while latently replicating MHV-68 genomes readily acquire distinct patterns of activation-associated histone modifications upon *de novo* infection, they fundamentally differ in their ability to efficiently attract H3K27-me3 marks. Statistical analyses of ChIP-seq data from *in vitro* infected cells as well as *in vivo* latency reservoirs furthermore suggest that, whereas KSHV rapidly attracts PRCs in a genome-wide manner, H3K27-me3 acquisition by MHV-68 genomes may require spreading from initial seed sites to which PRC are recruited as the result of an inefficient or stochastic recruitment, and that immune pressure may be needed to select for latency pools harboring PRC-silenced episomes *in vivo*.

Using co-infection experiments and recombinant viruses, we also show that KSHV'S ability to rapidly and efficiently acquire H3K27-me3 marks does not depend on the host cell environment or unique properties of the KSHV-encoded LANA protein, but rather requires specific cis-acting sequence features. We show that the non-canonical PRC1.1 component KDM2B, a factor which binds to unmethylated CpG motifs, is efficiently recruited to KSHV genomes, indicating that CpG island characteristics may constitute these features. In accord with the fact that, compared to MHV-68, KSHV genomes exhibit a fundamentally higher density of CpG motifs, we furthermore demonstrate efficient acquisition of H2AK119-ub by KSHV and H3K36-me2 by MHV-68 (but not vice versa), furthermore

bioRxiv preprint first posted online May. 15, 2019; doi: http://dx.doi.org/10.1101/639898. The copyright holder for this preprint (which was not peer-reviewed) is the author/funder, who has granted bioRxiv a license to display the preprint in perpetuity. It is made available under a CC-BY 4.0 International license.

supporting the notion that KSHV genomes rapidly attract PRC1.1 complexes in a genome-wide fashion. Collectively, our results suggest that rapid PRC silencing is not a universal feature of viral latency, but that some viruses may rather have adopted distinct genomic features to specifically exploit default host pathways that repress epigenetically naive, CpG-rich DNA.

bioRxiv preprint first posted online May. 15, 2019; doi: http://dx.doi.org/10.1101/639898. The copyright holder for this preprint (which was not peer-reviewed) is the author/funder, who has granted bioRxiv a license to display the preprint in perpetuity. It is made available under a CC-BY 4.0 International license.

Author Summary

During herpesvirus latency, viral genomes persists as partially repressed nuclear episomes which do not express genes required for progeny production. Latently infected cells not only form a reservoir of lifelong persistence but also represent the driving force in cancers associated with tumorigenic herpesviruses such as KSHV. Hence, it is fundamentally important to understand the mechanisms controlling latency. We have shown previously that latent KSHV episomes rapidly acquire H3K27-me3, a histone mark associated with polycomb repressive complexes (PRC). PRCs play a pivotal role in the control of developmental genes but are also involved in the pathogenesis of several tumors. We here investigated whether PRC-repression represents a general feature of herpesvirus latency. By performing side-by-side analyses of KSHV and the related MHV-68 we show that the latter indeed has a fundamentally lower propensity to acquire H3K27-me3, and that KSHV'S ability to rapidly attract this mark is most likely the result of a specific sequence composition that promotes recruitment of non-canonical PRC1 (a complex which is important for the regulation of cellular CpG islands). Our results have widespread implications for nuclear DNA viruses and suggest that some viruses have specifically evolved to exploit common host responses to epigenetically naive DNA.

bioRxiv preprint first posted online May. 15, 2019; doi: http://dx.doi.org/10.1101/639898. The copyright holder for this preprint (which was not peer-reviewed) is the author/funder, who has granted bioRxiv a license to display the preprint in perpetuity. It is made available under a CC-BY 4.0 International license.

Introduction

Herpesvirus latency is characterized by nuclear persistence of viral episomes in the absence of viral progeny production. To establish latency, herpesviruses must ensure that genes required for productive/lytic infection are efficiently silenced, while expression of those required for episomal persistence must be preserved. Given these requirements, epigenetic modifications of viral DNA or chromatin have long been suspected to play an important role during establishment and maintenance of herpesvirus latency.

Kaposi Sarcoma-associated herpesvirus (KSHV) is the etiologic agent of several tumors, including Kaposi sarcoma (KS), primary effusion lymphoma (PEL) and the plasmablastic variant of multicentric Castleman disease (MCD) [reviewed in 1, 2]. The tumor cells in these malignancies unequivocally express the major latency cassette of KSHV to produce several viral microRNAs (miRNAs) and at least four proteins. Among the latter, the multifunctional latency-associated nuclear antigen (LANA, encoded by ORF73) is especially important for viral persistence: LANA recruits the host cell replication machinery to viral origins of replication and tethers KSHV genomes to host chromosomes to ensure proper episome segregation [reviewed in 3]. While latent KSHV transcription and replication have first been studied in B cell lines derived from PEL tumors, later studies have shown that the virus readily establishes latency in a wide variety of adherent cells [4, 5]. Using such models, we have previously shown that methylation of viral DNA is a late and secondary event that is preceded by the establishment of distinct histone modification patterns [6]. Most notable among these are the global acquisition of the repressive histone mark H3K27-me3 (a modification deposited by the EZH2 component of polycomb repressive complex 2, PRC2) and formation of distinct peaks of activation-associated histone marks (H3K4-me3 and H3K9/K15-ac) not only at the major latency promoter, but also various regions encoding transcriptionally silent lytic genes. While the latter are generally anti-correlated with H3K27-me3, they co-exist with the repressive mark on a few loci (including the promoter of the major lytic transactivator Rta, encoded by ORF50) to form bivalent chromatin, a type of facultative heterochromatin poised for rapid re-expression. The putative function of the remaining

bioRxiv preprint first posted online May. 15, 2019; doi: http://dx.doi.org/10.1101/639898. The copyright holder for this preprint (which was not peer-reviewed) is the author/funder, who has granted bioRxiv a license to display the preprint in perpetuity. It is made available under a CC-BY 4.0 International license.

activation-associated histone marks in transcriptionally silent latent chromatin, however, remains unknown. Later studies have confirmed and extended above findings to demonstrate, for example, that acquisition of activating and repressive histone marks represent temporally separate processes, with the former already being fully present at 24h post infection, whereas H3K27-me3 marks require approximately 3 days to reach peak levels [7-9]. H3K27-me3 patterns furthermore evolve uniformly over the entire genome, sparing only some of the regions which already carry activation-associated modifications [8]. This observation strongly suggests that KSHV episomes attract PRCs via a global mechanism, rather than spreading from initial sites to which they are recruited by sequence-specific transcription factors (as is likely the case for activation-associated marks). In addition to de novo infected cells and tumor-derived cell lines, widespread H3K27-me3 marks have also been found to decorate KSHV genomes in primary KS tumors [10]. The fact that knock-down or pharmacological inhibition of PRC2 or PRC1 results in an increase of lytically reactivating cells furthermore supports the hypothesis that polycomb repression plays an important role in the maintenance of KSHV latency [6, 7, 11, 12].

An important question that remains, however, is what cellular mechanisms shape the viral epigenome and to what extent such mechanisms, in particular PRC recruitment, are influenced by viral factors. Indeed, although a recent study by Toth and colleagues elegantly demonstrated a principal requirement for LANA during H3K27-me3 acquisition, the kinetics of H3K27-me3 accumulation and LANA expression suggest that other, as of yet unknown factors are critically involved in the initial global recruitment process [13]. Since polycomb group proteins (PcG) have recently emerged as important factors that restrict viral gene expression of diverse viral species including CMV, HSV-1 and HIV, it is an intriguing possibility that polycomb repression and H3K27-me3 deposition may represent a default host response to the nuclear presence of non-chromatinized and/or unmethylated DNA. In such scenarios, latency establishment may result from viral subversion of host cell mechanisms which serve to silence epigenetically naive DNA. Apart from KSHV, however, the chromatin landscape associated with the early phase of herpesvirus latency remains unknown.

bioRxiv preprint first posted online May. 15, 2019; doi: http://dx.doi.org/10.1101/639898. The copyright holder for this preprint (which was not peer-reviewed) is the author/funder, who has granted bioRxiv a license to display the preprint in perpetuity. It is made available under a CC-BY 4.0 International license.

This is also true for murine gammaherpesvirus-68 (MHV-68), a virus which shares a co-linear genome organization as well as significant functional and sequence conservation across a large fraction of its protein products with KSHV. Since MHV-68 is furthermore able to establish persistent infections in laboratory mice it represents a valuable model system to study infection by KSHV and related γ-herpesviruses. Similar to KSHV, MHV-68 persists in CD19+ B-cells, with germinal center and marginal zone B-cells exhibiting the highest frequency of latent infection [14]. While the virus can induce lymphoproliferative disease under certain experimental conditions, the clonal lymphoma cells are typically MHV-68-negative, suggesting tumor induction via hit-and-run mechanisms, paracrine effects or chronic inflammation [15]. Indeed, to date only a single persistently infected B cell line (S11) has been established from infected mice [16]. Since (unlike KSHV) MHV-68 by default enters the lytic cycle upon *in vitro* infection of permissive cells, S11 and its derivative sub-clones continue to serve as the predominant tissue culture model to study MHV-68 latency.

Epigenetic analyses of latent MHV-68 episomes thus far has been limited to the ORF50 promoter region. Although this region is generally poor in CpG dinucleotides, Gray and colleagues found that the distal ORF50 promoter undergoes CpG-methylation at later stages of latency in mice [17]. In accord with this, Yang et al. found the ORF50 promoter to be methylated in mouse derived splenocytes as well as in S11E (a sub-clone of S11 which shows a lower rate of spontaneous reactivation) cells [18]. However, treatment with the DNA-methyltransferase inhibitor 5'-Azacytidine failed to induce lytic replication, suggesting that DNA methylation is not the primary or only block of ORF50 expression during latent MHV-68 infection.

Given the above, we set out to perform a comparative and comprehensive analysis of epigenetic modifications in latent KSHV and MHV-68 genomes. In particular, we aimed at elucidating whether latently replicating MHV-68 episomes would attract polycomb repressive complexes (PRCs) with similar efficiency as KSHV, thus arguing for PRC recruitment representing a general characteristic of gammaherpesvirus latency. Indeed, our results show that, even in the same host background, MHV-68 genomes acquire H3K27-me3 marks much slower and less efficiently than KSHV, suggesting that

bioRxiv preprint first posted online May. 15, 2019; doi: http://dx.doi.org/10.1101/639898. The copyright holder for this preprint (which was not peer-reviewed) is the author/funder, who has granted bioRxiv a license to display the preprint in perpetuity. It is made available under a CC-BY 4.0 International license.

148 virus specific cis-acting features, most likely the presence of a high frequency of unmethylated CpG
149 motifs, regulate the recruitment of PRCs to epigenetically naïve viral DNA.
150
151

152 ## Results

153 **Comparative analysis of gammaherpesvirus epigenomes in tumor-derived B-cell lines**

154 Although MHV-68 establishes latency in the spleen of infected mice, the low frequency of such cells
155 against a high background of uninfected cells greatly complicates direct ChIP-seq analysis of primary
156 splenic lymphocytes. We therefore sought to first investigate the epigenetic landscape of MHV-68
157 genomes in the established B-cell line S11E and compare it to that of KSHV in BCBL-1 cells, a cell line
158 derived from primary effusion lymphoma. As shown in Fig 1A, our ChIP-Seq analysis of BCBL1 cells
159 produced profiles of activating H3K4-me3 and repressive H3K27-me3 marks which were highly similar
160 to those of previous ChIP on microarray analyses [6, 11]. In contrast, ChIP-seq profiles of MHV-68
161 genomes in S11E cells were markedly different (see Fig 1B). Although, like KSHV, MHV-68 epigenomes
162 exhibited peaks of activation-associated histone marks outside of the latency region, the total number
163 as well as relative enrichment of such peaks was substantially lower. Overall, MACS14 peak detection
164 found only three regions to be significantly enriched for H3K4-me3: two peaks upstream of M2 and
165 M7 and another peak in the 3' region of ORF75A (Fig 1B, black bars). Two additional sites upstream of
166 ORF18b and M11 (marked with an asterisk in Fig 1B) were also enriched in the IgG control (Fig S1A)
167 and thus considered false positives.
168 In stark contrast to KSHV, we did not detect a distinct profile or abundant levels of the facultative
169 heterochromatin mark H3K27-me3 on MHV-68 episomes in S11E cells. The constitutive
170 heterochromatin mark H3K9-me3 was also absent (see S1 Fig A for H3K9-me3 and H3K9/K14-ac
171 profiles). To further investigate whether the weak signals of repressive histone marks may
172 nevertheless reflect a biologically significant modification profile we calculated correlation coefficients
173 (cc) for the different data sets (see S1 and S2 Dataset for coverage data and pairwise correlation

bioRxiv preprint first posted online May. 15, 2019; doi: http://dx.doi.org/10.1101/639898. The copyright holder for this preprint (which was not peer-reviewed) is the author/funder, who has granted bioRxiv a license to display the preprint in perpetuity. It is made available under a CC-BY 4.0 International license.

174 coefficients, respectively, across all ChIP-seq experiments in this study). Since H3K4-me3 and H3K27-
175 me3 are (except at bivalent loci) generally anti-correlated, the absence of such a correlation would
176 indicate that the H3K27-me3 profiles represent pure background. Indeed, consistent with our previous
177 findings [6], KSHV showed profound anti-correlation between H3K4-me3 and H3K27-me3 (cc: -0.55).
178 In contrast, our MHV-68 data show no anti-correlation of both histone marks (cc: 0.08) indicating that
179 the signal of H3K27-me3 is not distinguishable from the background ChIP signal. Hence, our analysis
180 suggests that the majority of MHV-68 episomes in S11E cells do not carry significant levels of repressive
181 histone marks and appear to be decorated by only a small number of activation associated peaks.
182
183 **RNA-seq analysis suggests that lytic gene products dominate the viral transcriptome in S11E cells**
184 In KSHV-positive cells, reactivation of productive replication does result in only minor alterations of
185 the bulk epigenetic profile. During late stages of the lytic cycle, accumulation of large numbers of *de*
186 *novo* replicated genomes (which do not carry any histones and thus only contribute to the input)
187 furthermore decreases relative ChIP enrichment values. We therefore wondered whether the sparsity
188 of detectable ChIP signals as shown in Fig 1B may, at least in part, result from spontaneously
189 reactivating cells carrying a disproportionally large fraction of epigenetically naive episomes which
190 mask the authentic epigenetic profile of latent episomes. Although a predominantly latent expression
191 profile of the original S11E had been shown by array hybridization [19], we wished to compare the
192 transcription profile of our S11E subculture to lytic MHV-68 transcription during the course of a *de*
193 *novo* infection. For this purpose, we performed RNA-seq of our S11E cells and murine cultures of the
194 epithelial cell line MLE12 undergoing lytic replication after *de novo* infection with MHV-68 (Fig 2, see
195 S2 Fig for additional time points post infection).
196 Surprisingly, the bulk transcription profile of our S11E cultures was highly similar to that of the lytically
197 infected MLE12 cells, indicating that the transcriptional activity of viral episomes in spontaneously
198 reactivating cells greatly outweighs that of the numerically more abundant latently infected cells.
199 Although we cannot directly determine the ratio of productively and latently replicating episomes in

bioRxiv preprint first posted online May. 15, 2019; doi: http://dx.doi.org/10.1101/639898. The copyright holder for this preprint (which was not peer-reviewed) is the author/funder, who has granted bioRxiv a license to display the preprint in perpetuity. It is made available under a CC-BY 4.0 International license.

this population, these data indicate that the epigenetic profiles observed in the S11E cells may only partially reflect the authentic chromatin state of latent MHV-68 genomes. The fact that H3K27me3 profiles of latent KSHV genomes remain clearly detectable even in BCBL1 cultures that are induced by TPA [11], however, argues for the assumption that the latent fraction of MHV-68 genomes in S11E cells does indeed not carry abundant levels of this mark.

An ORF50 deletion mutant (MHV-68Δ50) establishes a strictly latent gene expression profile

To circumvent the experimental and interpretational limitations imposed by S11-derived cultures, we sought to establish a strictly latent *de novo* infection system. For this purpose, we generated a mutant MHV-68 clone (MHV-68Δ50) with a deletion encompassing the region encoding Rta, the master lytic transactivator (see methods section for information on generation of the mutant and production of infectious viral particles). We reasoned that, due to its inability to enter the lytic cycle, the mutant should allow us to observe the epigenetic profile acquired by latently replicating episomes, in particular with regard to the hallmark traits of latent KSHV genomes, namely activation-associated marks outside of latent transcription units and global acquisition of repressive H3K27-me3 marks.

Infection of murine lung epithelial MLE12 cells with MHV-68Δ50 resulted in fully viable cultures which, similar to *de novo* latently infected KSHV cell lines [4], spontaneously lost viral episomes at an estimated rate of approx. 5-10% per cell generation. We maintained a highly positive culture by repeated sorting for GFP-positive cells over a period of more than three weeks and subsequently analyzed the transcriptome in these long-term infected cells by strand-specific RNA-seq. As shown in Fig 2B and -C (see also S3 Dataset), in contrast to our S11E cells MHV-68Δ50 infected cells indeed exhibited a viral gene expression profile that was highly restricted. The highest level of viral gene expression could be assigned to ORF73, an ORF which encodes the MHV-68 homologue of LANA (mLANA). Additionally, abundant coverage was detected in the region encompassing ORFs 75a to 75c, likely due to the presence of unspliced variants of ORF73-coding transcripts that originate at the terminal repeats. Notably, a weak (note logarithmic scale in Fig 2B) but distinct transcription signature

bioRxiv preprint first posted online May. 15, 2019; doi: http://dx.doi.org/10.1101/639898. The copyright holder for this preprint (which was not peer-reviewed) is the author/funder, who has granted bioRxiv a license to display the preprint in perpetuity. It is made available under a CC-BY 4.0 International license.

226 was detectable at two broader sites of the genome between ORFs M1 and 11 as well as ORFs 49 and
227 69.
228
229 **Epigenetic analysis of MHV-68Δ50 reveals distinct profiles of activation-associated histone marks**
230 **and suggests that viral genomes do not efficiently recruit PRCs**
231 Given the highly restricted transcription patterns described above, we concluded that MHV-68Δ50
232 infected cells provide a uniform population of latently replicating episomes and proceeded to analyze
233 the distribution of activating and repressive histone modifications by ChIP-seq. In parallel, we
234 performed ChIP-seq from long-term *in vitro* infected SLK cells (SLK_P) [4] to allow direct comparison with
235 a strictly latent KSHV infection. Similar to BCBL1, the ChIP-seq results for SLK_P cells were highly
236 congruent with our previous ChIP on microarray data [6], exhibiting profound anti-correlation (cc: -
237 0.58) of strongly enriched H3K4-me3 and H3K27-me3 profiles (Fig 3A). Hence, as noted before [6, 8],
238 while a few H3K4-m3 peaks differ between BCBL1 and SLK_P cells (likely due to differences in the cell
239 type-specific transcription factor repertoire), all regions not already decorated by H3K4-me3 acquire
240 abundant H3K27-me3 marks, indicating that global affinity for PRCs is a fundamental property of latent
241 KSHV episomes.
242 As shown in Fig 3B, MHV-68Δ50 indeed also acquired a highly distinct profile of activating histone
243 marks (H3K4-me3 and H3K9/K14-ac), with MACS14 peak detection revealing 15 significantly enriched
244 H3K4-me3 positive sites (black bars in Fig 3B). Interestingly, while latently replicating MHV-68Δ50 and
245 KSHV episomes were similar in their recruitment of activation-associated histone marks, MHV-68Δ50
246 did not attract abundant levels of H3K27-me3. Nevertheless, despite overall low enrichment the
247 resulting profiles showed anti-correlation with H3K4-me3 and H3K9/K14-ac (cc: -0.25 and -0.34,
248 respectively), indicating a baseline signature of H3K27-me3 that may result from slow recruitment of
249 PRCs by a subset of viral episomes. The constitutive heterochromatin mark H3K9-me3 was likewise not
250 widely distributed throughout the MHV-68Δ50 genome, but also showed slight anti-correlation with
251 H3K9/K14-ac (cc: -0.25). While a region encompassing ORFs M1 to M4 at the left end of the genome

bioRxiv preprint first posted online May. 15, 2019; doi: http://dx.doi.org/10.1101/639898. The copyright holder for this preprint (which was not peer-reviewed) is the author/funder, who has granted bioRxiv a license to display the preprint in perpetuity. It is made available under a CC-BY 4.0 International license.

was noticeably enriched for H3K9-me3 marks, mapping of the ChIP-seq reads to the BAC (which is inserted upstream of M1) also revealed profound H3K9-me3 enrichment along the integrated cassette (S1 Fig B). Hence, at least a subset of the BAC sequences undergo heterochromatinization, and it is thus possible that the observed signals in the M1-M4 region result from spreading of such heterochromatin into the neighboring viral regions.

To further elucidate the timeframe during which activation-associated histone mark patterns are established we infected MLE12 cells with MHV-68Δ50 and analyzed episomes at day five post infection by ChIP-Seq (Fig 3C). Indeed, the H3K4-me3 patterns observed at this early time point were highly similar (average cc: 0.55), but not completely identical to those detected after long-term infection. ChIP-peak calling using MACS14 on the H3K4-me3 samples detected a total of 9 uniquely enriched sites (marked by asterisks in Fig 3B and C) located upstream of M2, ORF18b, ORF23, ORF37, ORF69/M10 ORF73/74 in long-term infected cells, or upstream of M3/M4, ORF42 and ORF59 at day five post infection (see S4 Dataset for a list of all H3K4-me3 peaks identified during our experiments). Interestingly, although we did not experimentally interrogate H3K4me3-marked regions for promoter activity, cross-comparison of peak location with transcription cassettes predicted from our RNA-seq data (see S1 Protocol, S5 Dataset) suggests that these peaks are preferentially found upstream of genes expressed immediately after *de novo* infection or reactivation (S3 Fig).

Statistical analysis of ChIP-seq data results confirms overall absence of H3K27-me3 from MHV-68Δ50 genomes

Although we did not observe that MHV-68Δ50 genomes were strongly enriched for H3K27-me3 (Fig 3), the anti-correlation with H3K4-me3 suggests that the weak H3K27-me3 signals did not purely represent background. We therefore set out to perform a statistical analysis designed to provide a better estimate of the actual H3K27-me3 levels acquired by MHV-68 and KSHV episomes via direct comparison with strongly enriched host regions. For this purpose, we mapped the ChIP-seq and input reads from two independent experiments of long-term MHV-68Δ50-infected MLE12 or KSHV-infected

bioRxiv preprint first posted online May. 15, 2019; doi: http://dx.doi.org/10.1101/639898. The copyright holder for this preprint (which was not peer-reviewed) is the author/funder, who has granted bioRxiv a license to display the preprint in perpetuity. It is made available under a CC-BY 4.0 International license.

278 SLK_P cells to the appropriate host genome assemblies and, using enrichment detection with SICER/EPIC
279 [20], identified the 200 host regions most significantly enriched for H3K27-me3. Conversely, as a
280 negative control we randomly selected 200 regions with a similar length distribution from the host
281 genome, excluding all regions previously identified as H3K27-me3 enriched by SICER/EPIC2 as well as
282 excluding regions blacklisted according to ENCODE. Viral H3K27-me3 enrichment values were
283 subsequently calculated by sliding a window of 10 kb (to reflect broad regions comparable to detected
284 host regions) across the viral genome. To allow cross-comparison between individual samples, all data
285 were then normalized to the median value of the negative control regions. The data shown in Fig 4
286 thus represent fold enrichment over the negative control loci (cellular ChIP background) and allow a
287 direct assessment of H3K27-me3 occupancy on viral genomes in the overall context of the host
288 epigenome (note that this is an assessment of global H3K27-me3 acquisition across the viral genome,
289 rather than recruitment to individual and discrete sites). For more details, see the materials and
290 methods section. As shown in the right panel of Fig 4, enrichment of H3K27-me3 on KSHV genomes in
291 SLK_P cells was significantly higher compared to not only the negative, but even the positive host control
292 loci, underlining our previous notion that efficient and global recruitment of PRCs is a hallmark of KSHV
293 latency. In stark contrast, average H3K27-me3 enrichment levels on MHV-68Δ50 genomes (left panel)
294 were comparable to those of the negative control set. Thus, our statistical analysis strongly supports
295 the conclusion that, even after prolonged *in vitro* infection, the majority of latently replicating MHV-
296 68Δ50 genomes does not efficiently attract H3K27-me3 marks.
297
298 **The ability to rapidly recruit PRC2 is a virus- but not a host cell-specific feature**
299 Since the lack of H3K27-me3 (and thus, most likely, PRC2-) recruitment to MHV-68Δ50 episomes was
300 in striking contrast to the mechanisms observed in latent KSHV infection, we sought to investigate
301 whether this disparate behavior indeed reflected intrinsic properties of the two viruses or may rather
302 be caused by the host cell background (i.e., a potentially general impairment of polycomb recruitment
303 pathways in the murine system). We therefore performed a superinfection of long-term MHV-68Δ50-

bioRxiv preprint first posted online May. 15, 2019; doi: http://dx.doi.org/10.1101/639898. The copyright holder for this preprint (which was not peer-reviewed) is the author/funder, who has granted bioRxiv a license to display the preprint in perpetuity. It is made available under a CC-BY 4.0 International license.

304 infected MLE12 cells with KSHV for five days, a timeframe that allows full establishment of latency
305 associated chromatin structures on KSHV episomes after *de novo* infection of human cells [6, 8]. We
306 subsequently analyzed the ability of KSHV to recruit H3K27-me3 marks in the MHV-68Δ50 positive
307 murine cell system by ChIP-seq (Fig 5), normalizing read counts by input for each virus to correct for
308 differences in copy numbers per cell. Although slightly noisier compared to the previous analysis,
309 H3K4-me3 patterns on MHV-68Δ50 genomes were highly similar to the data shown in Fig 3B (cc: 0.85).
310 Likewise, despite the heterologous host species background, KSHV acquired activation mark patterns
311 that overall correlated well with the profiles observed in SLK_P cells (cc: 0.76), with the highest
312 enrichment detectable in the latency associated region. A number of prominent peaks observed in
313 SLKp cells (e.g., the peak upstream of vIRF3), however, were less pronounced in MLE12 cells, likely due
314 to differences with which murine transcription factors bind to specific target sites in the KSHV genome.
315 To determine the extent of H3K27-me3 recruitment by KSHV and MHV-68Δ50 genomes, we performed
316 the same statistical analysis as for the previous dataset (Fig 5B). Indeed, while MHV-68Δ50 genomes
317 were again not significantly different from the background, the enrichment of H3K27-me3 on KSHV
318 genomes was highly significant and (similar to the observations made in SLK_P cells) exceeded that of
319 the endogenous murine positive controls. As before, global H3K27-me3 patterns were anti-correlated
320 with H3K4-me3 marks (cc: -0.32).
321 In complete agreement with our ChIP-seq analysis, ChIP-qPCR for a number of viral and host loci
322 confirmed that enrichment of H3K27-me3 on KSHV was about three fold higher when compared to
323 positive control regions, whereas the selected MHV-68Δ50 loci were negative (Fig 5C). Additionally,
324 the ChIP-qPCR confirmed the patterns of activation-associated histone marks in both viruses.
325
326 **Unique properties of KSHV LANA are not responsible for rapid H3K27-me3 acquisition**
327 A recent report by Toth et al. [13] demonstrated that acquisition of H3K27-me3 marks by KSHV is
328 critically dependent on the presence of an intact LANA molecule, suggesting that KSHV LANA (kLANA)
329 itself may mediate PRC recruitment. Given this, we wondered whether unique properties of kLANA

bioRxiv preprint first posted online May. 15, 2019; doi: http://dx.doi.org/10.1101/639898. The copyright holder for this preprint (which was not peer-reviewed) is the author/funder, who has granted bioRxiv a license to display the preprint in perpetuity. It is made available under a CC-BY 4.0 International license.

that are not conserved in murine homolog (mLANA) may be required for rapid acquisition of H3K27-me3, potentially explaining the absence of this mark from MHV-68 episomes in singly or co-infected cells. Although KSHV and MHV-68 LANA preferentially bind to their cognate sites within the terminal repeats, a number of recent studies have suggested that they can also reciprocally support genome replication and maintenance [21-24]. We therefore sought to investigate the ability of a recombinant MHV-68 genome harboring a kLANA gene to attract H3K27-me3 marks. For this purpose, we introduced the ORF50 deletion in the background of a chimeric MHV-68 mutant (recently generated by Habison and colleagues [21]) in which mLANA was replaced by kLANA, permitting us to investigate the chromatin landscape of latently replicating MHV-68 genomes that are maintained by kLANA instead of mLANA. As expected, MLE12 cells infected with either the mLANA-expressing MHV-68Δ50 virus or the MHV-68Δ50-kLANA mutant showed readily detectable expression of the respective LANA protein (Fig 6D). As shown in Figs 6A and B, however, ChIP-seq analysis did not find any significant differences between H3K27-me3 enrichment levels at 5 days post-infection, yielding profiles that were very close to background regardless of whether MHV-68 genomes expressed m- or kLANA proteins. Quantitative ChIP-PCR from chromatin harvested after 5 and 35 days post-infection confirmed these results and demonstrated that, even after prolonged infection, kLANA-mediated episome maintenance did not confer the ability to rapidly attract polycomb repressive complexes to MHV-68 genomes (Fig 6C).

While kLANA has been shown to support episome maintenance of MHV-68 genomes [21-23], it seemed formally possible that it may be selectively defective for PRC recruitment in a non-syngeneic context, for example due to differential binding stoichiometry at the terminal repeats or the lack of low affinity binding sites in the coding region. We therefore also tested whether trans-complementation of a LANA-deleted KSHV genome with either kLANA or mLANA would result in differential behavior towards PRC repression, expecting that mLANA-maintained KSHV genomes may be unable to acquire H3K27-me3 marks. Accordingly, we generated MLE12 cells stably expressing either mLANA or kLANA (Fig 7D) and infected the cultures with a BAC16-derivative virus with a deletion

bioRxiv preprint first posted online May. 15, 2019; doi: http://dx.doi.org/10.1101/639898. The copyright holder for this preprint (which was not peer-reviewed) is the author/funder, who has granted bioRxiv a license to display the preprint in perpetuity. It is made available under a CC-BY 4.0 International license.

356 encompassing the LANA-encoding region (KSHV-BAC16Δ73). Due to relatively low titers of the KSHV-
357 BAC16Δ73 virus (~1% initial infection efficiency) we were unable to perform ChIP-Seq analysis
358 immediately after infection. However, as shown in the upper panels of Fig 7A, ChIP-qPCR performed
359 after 5 days p.i. did not indicate any significant changes of H3K4-me3 or H3K27-me3 patterns across a
360 number of human and viral marker loci. In particular, all viral loci that had acquired significant levels
361 of H3K27-me3 in KSHV wt infected cells did so in transcomplemented KSHV-BAC16Δ73, regardless of
362 whether cells were expressing kLANA or mLANA.
363 Under antibiotic selection, kLANA as well as mLANA-expressing cells (but not the parental ML12 cells)
364 yielded hygromycin-resistant cultures, as was expected based on the previously reported ability of
365 mLANA to support maintenance of episomes harboring KSHV terminal repeats [21]. We repeated our
366 ChIP-qPCR analysis and additionally performed ChIP-Seq from the bulk-selected cultures at 33 days
367 p.i., a similar late time point as in our previous MHV-68Δ50 or MHV-68Δ50-kLANA experiments. As
368 shown in the lower panels of Fig 7A, ChIP-qPCR suggested that KSHV-BAC16Δ73 had maintained
369 patterns of H3K4-me3- and H3K27-me3-positive loci as already observed after 5 days if infection. These
370 results were furthermore confirmed by the ChIP-seq data presented in Fig 7B, which in both cases
371 yielded very similar patterns of distinct H3K4-me3 peaks and broad, anti-correlated zones of H3K27-
372 me3 as previously observed during KSHV wild type infection of MLE12 cells (Fig 5A; note that the
373 additional peaks near the center in Fig 7B map to the bacmid cassette in BAC16 which constitutively
374 expresses GFP and hygromycin resistance markers). Statistical analysis of H3K27-me3 levels on KSHV-
375 BAC16Δ73 likewise indicated that KSHV-BAC16Δ73 episomes were able to efficiently attract H3K27-
376 me3 in kLANA as well as mLANA-expressing cells (Fig 7C). The only appreciable difference was that
377 input coverage across the left half of the KSHV genome was noticeably lower in MLE12: mLANA cells
378 (see bottom panel in Fig 7C), an observation which is reminiscent of the loss of sub-genomic material
379 recently observed with KSHV mutants expressing an oligomerization-deficient kLANA protein [25].
380 Nonetheless, our experiments consistently demonstrate that both KSHV and MHV-68 genomes
381 maintain original dynamics of H3K27-me3 acquisition when (trans-)complemented with a non-

bioRxiv preprint first posted online May. 15, 2019; doi: http://dx.doi.org/10.1101/639898. The copyright holder for this preprint (which was not peer-reviewed) is the author/funder, who has granted bioRxiv a license to display the preprint in perpetuity. It is made available under a CC-BY 4.0 International license.

382 syngeneic LANA protein, underlining our previous notion that cis-acting mechanisms are of pivotal
383 importance and suggesting that kLANA does not possess unique properties which mediate rapid PRC
384 recruitment.
385
386
387 **Analysis of MHV-68 infected splenocytes suggests that wildtype genomes in long-term latency pools**
388 **are marked by H3K27-me3 *in vivo***
389 While our data show that MHV-68 genomes are unable to efficiently acquire H3K27me3 in a rapid
390 fashion, the slight anti-correlation between H3K27-me3 and H3K4-me3 profiles in long-term infected
391 cultures suggested that a small fraction of MHV-68 genomes nevertheless attract PRC, either as a result
392 of an effective (but rare) stochastic event, or a constitutive (but generally weak) recruitment
393 mechanism. If so, one may hypothesize that immune pressure *in vivo* could select or enrich for
394 polycomb-repressed genomes during establishment of latency reservoirs. To investigate this
395 possibility, we infected two mice with wildtype MHV-68 and isolated splenocytes and latently infected
396 B-cells from the spleens 17 days after infection. Since the fraction of infected cells among the total
397 population is very low we subjected the chromatin directly to ChIP-qPCR for H3K4-me3 and H3K27-
398 me3 (Fig 8A), using a set of MHV-68 and host-specific primers from our previous *in vitro* infection
399 experiments. Overall, the ChIP-qPCR results from both mice were highly concordant for both histone
400 marks and across all loci, strongly arguing for the validity of the data. As shown in the top panel of Fig
401 8A, in both mice H3K4-me3 was readily detectable in three of the regions which had also tested
402 positive in MHV-68Δ50 infected MLE12 cells (mORF72, M13 and downstream of M5), whereas the
403 regions close to ORF4 and ORF64 were not enriched *in vivo* . Additionally, analysis of H3K27me3
404 demonstrate that *in vivo* latency reservoirs of MHV-68 indeed exhibit enrichment of repressive H3K27-
405 me3 marks at most of the tested viral loci, at levels that were comparable to the endogenous positive
406 control MYT1 (center panel of Fig 8A). The only loci which appeared completely devoid of H3K27-me3
407 were M13 and the region downstream of ORF72, i.e. the same loci which showed the strongest

bioRxiv preprint first posted online May. 15, 2019; doi: http://dx.doi.org/10.1101/639898. The copyright holder for this preprint (which was not peer-reviewed) is the author/funder, who has granted bioRxiv a license to display the preprint in perpetuity. It is made available under a CC-BY 4.0 International license.

enrichment for H3K4-me3. The negative correlation of H3K4-me3 and H3K27-me3 at these loci indicates that the profiles originate from the same chromatin and do not represent differentially modified episomes.

Encouraged by these results, we next aimed to enrich latently infected splenocytes for ChIP-seq analysis. For this purpose, we infected six mice with MHV-68-H2BYFP, a recombinant virus expressing an EYFP-H2B fusion gene for *in vivo* tracking of MHV68-infected cells [26], and performed FACS sorting of splenocytes isolated after 17 days of infection. As the recovered cell numbers per animal (approximately 3000) were too low for individual analysis we pooled cells from three animals each and performed RNA-seq as well as ultra-low input ChIP-seq for H3K27-me3 on the resulting pools. Transcriptomic Immgen cluster analysis of the 200 most highly expressed host genes in YFP-positive splenocytes confirmed that the cells showed typical expression patterns of germinal center B cells, as expected for authentic splenic latency reservoirs (S4 Fig). Mapping of RNA-seq reads to the MHV-68 genome furthermore revealed readily detectable transcription of ORF73 (the gene encoding mLANA) together with viral expression patterns that were highly restricted when compared to S11E or productively infected MLE12 cells (See S2 Fig D and E for coverage plots and expression analysis). Although gene expression profiles suggest the presence of a reactivated sub-fraction of cells, the splenocytes clearly cluster with MHV-68Δ50 infected MLE12 cells and away from S11E or lytically infected MLE12 cultures (S2 Fig E), indicating successful isolation of latency pools.

As shown in Fig 8B, analysis of H3K27-me3 in each of the two replicates indeed revealed global enrichment patterns that, in accord with our previous ChIP-qPCR analysis of wt-infected mice, reached similar levels as the endogeneous positive controls (Fig 8C). Again, the region encompassing M13 and (to a lesser degree) the regions downstream of ORF72 showed lower levels of H3K27-me3. Although the limited available material did not allow us to perform ChIP-seq for activation-associated marks, this observation suggests that episomes in long term latency reservoirs share at least some of the H3K4-m3 marks observed in our *in vitro* experiments.

bioRxiv preprint first posted online May. 15, 2019; doi: http://dx.doi.org/10.1101/639898. The copyright holder for this preprint (which was not peer-reviewed) is the author/funder, who has granted bioRxiv a license to display the preprint in perpetuity. It is made available under a CC-BY 4.0 International license.

433 Taken together, although the levels of H3K27-me3 enrichment did not reach those observed for latent
434 KSHV episomes, the widespread distribution of H3K27me3 as well as its partial anti-correlation with
435 H3K4-me3 is highly reminiscent of latent KSHV epigenome patterns. This suggests that polycomb-
436 repression may indeed play a more concise role in *in vivo* latency reservoirs of MHV-68, potentially
437 due to immune pressure that selects for cells harboring silenced episomes.
438
439 **Binding of KDM2B and acquisition of H2AK119-ub during early infection suggest that KSHV attracts**
440 **polycomb repressive complexes via the non-canonical recruitment pathway**
441 Our previous results suggested that KSHV rapidly attracts H3K27-me3, whereas MHV-68 may do so in
442 a manner that proceeds stochastically or with low efficiency, and that cis-acting features underlie the
443 observed differences. We therefore sought to identify sequence features that could potentially explain
444 our observations. Regarding potential recruitment mechanisms in MHV-68, when overlaying
445 normalized H3K27-me3 patterns from all our MHV-68 experiments (Fig 8D) we noticed that the regions
446 flanking the left and right internal repeats (IR1 and -2 in the following) consistently reached the highest
447 enrichment levels. This suggests that PRCs may initially be recruited to the internal repeats (note that,
448 due to their repetitive nature, ChIP-seq reads cannot be mapped to the IR elements themselves) and
449 subsequently spreads into adjacent regions, with the region to the right of IR2 being more refractory
450 to spreading due to the presence of H3K4-me3 marks. In contrast, our previous temporal analysis [8]
451 suggests rapid global acquisition of H3K27-me3 methylation to KSHV genomes, rather than spreading
452 from nucleation sites. When we searched for similarities between the KSHV and the MHV-68 IR
453 elements that are not shared by the remainder of the MHV-68 genome, the prime characteristics that
454 emerged were those of CpG islands. As shown in S5 Fig B, the MHV-68 genome is highly CpG
455 suppressed (suppression index 0.43) and exhibits a general GC content of 47%. Only relatively short
456 regions meet the criteria of CpG Islands, chief among them the two IR regions. In contrast, nearly the
457 entire KSHV genome (average GC content 54%, CpG suppression index 0.84) registers as a single,
458 continuous CpG island (S5 Fig A). This observation was of particular interest since CpG islands have

bioRxiv preprint first posted online May. 15, 2019; doi: http://dx.doi.org/10.1101/639898. The copyright holder for this preprint (which was not peer-reviewed) is the author/funder, who has granted bioRxiv a license to display the preprint in perpetuity. It is made available under a CC-BY 4.0 International license.

459 emerged as the prime PRC recruitment signal in vertebrate cells during the recent years [reviewed in
460 27, 28]. In this pathway, the non-canonical PRC1.1 complex is directly recruited via binding of its
461 subunit KDM2B (a H3K36-specific demthylase [29]) to unmethylated CpGs, followed by ubiquitination
462 of H2A lysine 119 (H2AK119-ub) [30-33] . Given the fact that herpesviruses package epigenetically
463 naive DNA, and that KSHV episomes do not acquire substantial levels of DNA methylation until several
464 weeks post infection [6], we therefore tested the possibility that de novo-infecting KSHV genomes
465 recruit KDM2B and performed ChIP-seq analysis at 24h post infection. As shown in Fig 9A, we indeed
466 detected abundant and global binding of KDM2B to KSHV episomes, at levels that were comparable to
467 those seen on the most significantly enriched positive host loci (Fig 9B). Investigation of the signals
468 across the host genome furthermore confirmed the expected binding patterns at CpG Islands [30].
469 Unfortunately, we were unable to perform similar experiments with MHV-68 infected cells since later
470 lot numbers of the KDM2B antibody did not show expected enrichment patterns on the host genome,
471 rendering the fact that we did not detect any signals on the MHV-68 genome with these antibodies
472 inconclusive. In the absence of a working ChIP-grade KDM2B antibody, we therefore investigated
473 patterns of H3K36-me2, a histone mark that is the direct target of KDM2B's demethylase activity. Given
474 the observed binding to KSHV genomes, we expected that KSHV episomes should exhibit significantly
475 lower levels of H3K36-me2 compared to MHV-68. As shown in the top panels of Fig 9E (KSHV) and F
476 (MHV-68), this is indeed the case: Whereas KSHV exhibits very low signals of this histone mark in SLKp
477 cells, levels on MHV-68 episomes in MLE12:MHV-68Δ50 cells were significantly higher and reach levels
478 that were comparable to those of endogenous positive control loci (see statistical analysis in S7 Fig).
479 Global analysis of H3K36-me2 methylation patterns across the host genome (Fig 9D) furthermore
480 verified general anti-correlation with H3K27-me3 [34], thus confirming the validity of our data.
481 We next investigated global patterns of H2AK119-ub, the ubiquitination mark deposited by PRC1
482 complexes. As shown in the center panel Fig 9F, although a slight enrichment near the CpG-rich left
483 internal repeat unit was noticeable, MHV-68Δ50 genomes overall showed H2A-K119ub levels that
484 were not significantly above those of the host background (S7 Fig). In contrast, as expected KSHV

bioRxiv preprint first posted online May. 15, 2019; doi: http://dx.doi.org/10.1101/639898. The copyright holder for this preprint (which was not peer-reviewed) is the author/funder, who has granted bioRxiv a license to display the preprint in perpetuity. It is made available under a CC-BY 4.0 International license.

485 genomes in SLKp cells were highly enriched for this mark (Fig 9E, center panel). If KSHV genomes
486 acquire H3K27-me3 marks via KDM2B and the non-canonical PRC2 recruitment pathway, then global
487 acquisition of H2AK119-ub would be expected to occur simultaneously with, or even prior to H3K27-
488 me3 accumulation, and should also preclude H3K36-me2 acquisition during early infection. Indeed, a
489 previous report by Toth and colleagues found that binding of RYBP, a component of non-canonical
490 PRC1.1 complexes, precedes that of the PRC2 component EZH2 at a number of investigated loci [7]. To
491 directly compare *de novo* acquisition of PRC1- and PRC2-dependent marks on a global level, we
492 performed ChIP-seq for H2AK119-ub, H3K27-me3 and H3K36-me2 in SLK cells after 24 hours and 5
493 days post of infection. The graphs in Fig 9G show global enrichment of each mark across the viral
494 genome relative to average levels of the 200 most strongly enriched host loci (set to 100%; see S6 and
495 S7 Figs for full coverage plots and results of the statistical analysis). Statistical analysis of data from
496 SLKp and MHV-68Δ50-infected MLE12 cells are shown to the right for comparison. In accord with our
497 previous observation that H3K27-me3 marks require 48-72h to accumulate [8], we observe that
498 average H3K27-me3 levels are very high in SLK cells after 5 d.p.i. or in long-term infected SLKp cells,
499 but that enrichment over cellular background is not yet significant at 24h p.i. (three left plots in Fig
500 9G). In contrast, global enrichment of H2AK119-ub indeed is already highly significant after 24h p.i.,
501 and further increases through the 5d p.i time point. As expected, H3K36-me2 enrichment on KSHV
502 episomes was not observed at any time point, whereas this mark was substantially enriched on MHV-
503 68Δ50 genomes in MLE12 cells (right plot in Fig 9G). Taken together, these data strongly support the
504 hypothesis that KSHV genomes recruit PRC via the non-canonical pathway, likely as a result of their
505 high density of unmethylated CpGs.
506
507

508 ## Discussion

509 The factors determining the epigenetic fate of nuclear viral DNA remain poorly understood.
510 Herpesviruses represent attractive model systems to study such processes, given that they package

bioRxiv preprint first posted online May. 15, 2019; doi: http://dx.doi.org/10.1101/639898. The copyright holder for this preprint (which was not peer-reviewed) is the author/funder, who has granted bioRxiv a license to display the preprint in perpetuity. It is made available under a CC-BY 4.0 International license.

unmethylated and nucleosome-free genomes and thus must newly establish a suitable chromatin landscape upon each round of infection to support either their productive phase or latency. To address the role of polycomb group proteins in this process, we performed a comparative analysis of epigenetic modifications acquired by latent KSHV and MHV-68 genomes. Our comparison involves two viruses which share many evolutionary conserved traits on the genomic and protein level, yet, at least in vitro, show distinct biological behavior after *de novo* infection: whereas KSHV establishes latency in a wide variety of cell types and lines, MHV-68 infected cells are much more prone to undergoing lytic replication. We hypothesized that these differences may be reflected on the epigenetic level and that, if so, our comparative analysis may open new avenues towards elucidating the viral features, which regulate PRC recruitment. Indeed, our initial analysis of S11E cells suggested that MHV-68 attract little, if any, H3K27-me3 marks. Even though these cultures harbored a significant fraction of lytic cells, the fact that H3K27-me3 profiles on latent KSHV genomes remain readily detectable even in lytically-induced BCBL1 cultures [11] suggests that MHV-68 genomes in the latent fraction of cells do not carry abundant H3K27-me3 marks. However, as presence of lytic cells nevertheless complicates interpretation of these observations, we proceeded to investigate the epigenetic landscape of *de novo* infecting MHV-68 genomes that are deficient for the master lytic transactivator encoded by ORF50. At first, it may seem counterintuitive to employ a state of forced latency to investigate the factors which may favor latency in the first place. However, these factors are likely to act prior to lytic cycle entry and ORF50 expression. In support of this, Toth and colleagues recently reported that an ORF50/Rta deficient KSHV attracts H3K27-me3 marks indistinguishably from its wildtype counterpart [13], an observation which is in line with our own unpublished results. Hence, there is every reason to believe that the MHV-68Δ50 mutant provides an appropriate measure of the efficiency with which latently replicating episomes recruit PRCs. Indeed, our results demonstrate that MHV-68Δ50 exhibits a latent expression profile, but nevertheless does not attract abundant H3K27-me3 marks. Importantly, we show that this is independent of the host cellular background, as co-infecting KSHV episomes rapidly acquire H3K27-me3 marks at levels that are on par or above the most significantly enriched host loci.

bioRxiv preprint first posted online May. 15, 2019; doi: http://dx.doi.org/10.1101/639898. The copyright holder for this preprint (which was not peer-reviewed) is the author/funder, who has granted bioRxiv a license to display the preprint in perpetuity. It is made available under a CC-BY 4.0 International license.

Interestingly, although H3K27-me3 levels on MHV-68Δ50 were low, we detected anti-correlation with activation marks, suggesting that a subset of episomes may be targeted by PRC2. Considering this, our finding that H3K27-me3 was acquired to a higher extent in latently infected splenocytes isolated from mice at day 17 post infection indicates that PRC recruitment to MHV-68 episomes is possible, but may result from an inefficient or stochastic process. This suggests a model in which MHV-68 may have evolved to undergo rapid expansion via lytic replication in the lung of infected animals, followed by selection of cells harboring polycomb-repressed episomes in the spleen. Since we detected a low-level transcriptional signature of lytic genes in MHV-68Δ50-infected MLE12 cells, we postulate that stochastic firing of lytic promoters may generate immunogenic pressure for the selection of latently infected cells with tighter repression patterns. Of course, it is also possible that differences in the cellular background of splenocytes may allow MHV-68 to acquire H3K27-me3 more efficiently. If so, however, the fact that we did not observe any H3K27-me3 marks in S11E cells (a B cell line) argues against the hypothesis that it is the epithelial background of MLE12 cells *per se* which prevents acquisition of H3K27-me3. More importantly, we find that co-infecting KSHV episomes efficiently, rapidly and globally attract H3K27-me3 marks in MLE12 cells. Hence, the mechanisms that allow rapid PRC recruitment to KSHV genomes must be fully functional in MLE12 cells, yet do not act upon MHV-68 genomes. This allows us to draw important conclusions with regard to the nature of pathways attracting PRCs to KSHV. However, owing to the limitations of available MHV-68 latency models, it does not permit us to exclude the possibility that MHV-68 may employ different (and potentially splenocyte-specific) mechanisms in authentic *in vivo* latency reservoirs. Given that CpG-dependent pathways have emerged as a fundamental recruitment mechanism in mammals, we propose that the initial recruitment to viral genomes generally proceeds via the non-canonical pathway, but that KSHV's high CpG frequency serves to ensure rapid silencing in a manner that is largely independent of the cellular background, whereas MHV-68 may additionally require, for example, an environment that allows more efficient spreading of PRC from initial seed sites. Certainly, further studies will be required to elucidate the mechanism that may govern PRC-dependent repression of MHV-68 *in vivo*.

bioRxiv preprint first posted online May. 15, 2019; doi: http://dx.doi.org/10.1101/639898. The copyright holder for this preprint (which was not peer-reviewed) is the author/funder, who has granted bioRxiv a license to display the preprint in perpetuity. It is made available under a CC-BY 4.0 International license.

Although MHV-68 and KSHV episomes behave differently regarding PRC recruitment, they both acquire a number of distinct activation marks. Upon in vitro infection, activating histone modifications were acquired within the first days and most (but not all) of the peaks persisted throughout long-term infection, a feature which is reminiscent of observations made previously in the KSHV system [6, 8]. Our transcriptional analysis (S3 Fig, S5 Dataset) suggests that, as in KSHV [11], the activation-marked regions are preferentially associated with immediate early gene promoters. The fact that most activation marks are not associated with abundant transcription suggests that additional viral or host factors (including, but not necessarily limited to, ORF50/Rta) are required to permit full activation. We therefore suspect that the role of persistent activation marks is to keep immediate early promoters in an open chromatin configuration during latency, such that the virus can rapidly respond when such factors become available. Indeed, in methylated DNA immunoprecipitation experiments (MeDIP-seq, see S2 Protocol) we have observed that, while the MHV68 genome is principally subject to DNA methylation in long-term infected MLE12 cells (including, as previously reported [17, 18], at the distal ORF50 promoter), loci harboring persistent H3K4-me3 peaks remain negative. Whether such marks indeed facilitate reactivation from latency, however, remains to be established.

Finally, what are the features which mediate rapid recruitment of PRCs to KSHV episomes, and why does MHV-68 (at least in our model systems) exhibit such fundamentally different behavior? While further experiments will be required to work out the precise details, our study provides a framework which limits the possible options and suggests a potential mechanism. Firstly, our co-infection experiments clearly demonstrate that it is not a lack of specific host factors which preclude rapid PRC recruitment to MHV-68 genomes. At the same time, these data also show that latently expressed, trans-acting viral gene products encoded by MHV-68 do not interfere with efficient acquisition of H3K27-me3 by KSHV. Conversely, we can also conclude that expression of KSHV products is not sufficient to convey rapid PRC recruitment to MHV-68 episomes. We therefore considered two, mutually non-exclusive options: that polycomb recruitment may be regulated by viral cis-acting gene products that only act upon their parental episomes, or by unique genomic features that are present

bioRxiv preprint first posted online May. 15, 2019; doi: http://dx.doi.org/10.1101/639898. The copyright holder for this preprint (which was not peer-reviewed) is the author/funder, who has granted bioRxiv a license to display the preprint in perpetuity. It is made available under a CC-BY 4.0 International license.

589 in the KSHV, but not the MHV-68 genome. A prime candidate for the former was the KSHV-encoded
590 kLANA, given that a recent study [13] reported that a LANA-deficient virus fails to acquire H3K27-me3
591 marks. The study furthermore found kLANA to decorate the entire viral episome (likely via its unspecific
592 chromatin binding activity) and to form high molecular-weight complexes with PRC2 components.
593 Although it is presently unclear whether this complex formation reflects a direct interaction with PRC2
594 components or is a consequence of kLANA's chromatin binding ability per se, this suggests a model in
595 which LANA may directly promote PRC recruitment.
596 Our experiments with recombinant viruses show that substitution of mLANA by kLANA does not
597 convey the ability to rapidly acquire H3K27-me3 marks to MHV-68 genomes. Reciprocally, KSHV
598 episomes that are maintained by mLANA instead of kLANA do not lose this ability. Hence, whatever
599 function of kLANA is required for H3K27-me3 acquisition must be shared with mLANA, but at the same
600 time must be insufficient to mediate rapid PRC recruitment in the context of the MHV-68 genome. This
601 suggests one of the core features of the LANA proteins, such as the ability to support licensed DNA
602 replication, as a pre-requisite for H3K27-me3 acquisition, a hypothesis which we are currently
603 investigating. We would like to point out that such models do not exclude the possibility that
604 interaction of kLANA with PRC2 components may additionally facilitate H3K27-me3 acquisition.
605 However, they suggest that the primary trigger of rapid PRC recruitment is distinct [13]. The fact that
606 LANA has to accumulate in newly infected cells before it can bind to viral chromatin also suggests that
607 other factors are critically involved in the recruitment process.
608 Based on our results, we propose that these factors involve the same genomic sequence features
609 which also mediate PRC recruitment to host loci [reviewed in 27, 28]. Traditionally, polycomb
610 repression has been thought to result from a strictly sequential process: first, binding of PRC2 and
611 EZH2-dependent tri-methylation of H3K27, and second, recognition of H3K27-me3 marks by the PRC1
612 component Cbx and subsequent H2AK119 ubiquitination and transcriptional repression. Certain
613 transcription factors such as YY1 can recruit PRC2 in mammals, but the fact that KSHV genomes acquire
614 H3K27-me3 marks in a gradual and uniform manner argues for a global recruitment process, rather

bioRxiv preprint first posted online May. 15, 2019; doi: http://dx.doi.org/10.1101/639898. The copyright holder for this preprint (which was not peer-reviewed) is the author/funder, who has granted bioRxiv a license to display the preprint in perpetuity. It is made available under a CC-BY 4.0 International license.

than spreading from discrete transcription factor binding sites [8]. Interestingly, the traditional model is increasingly being challenged by studies suggesting that PRC2 binding and H3K27 methylation can also represent a secondary event that is preceded by direct PRC1 recruitment [reviewed in 27, 28, 35]. The prime genomic feature associated with PRC1 recruitment is high density of non-methylated CpG dinucleotides, and CpG density and methylation states are in fact good predictors of PRC2 recruitment in mammals [36]. Accumulating evidence suggests that the H3K36 demethylase KDM2B, a component of the non-canonical PRC1.1 complex which can bind to un-methylated CpG motifs via its CXXC zinc finger domain, is a major factor directing polycomb complexes to CpG islands [30-33]. A recent study furthermore demonstrated that gene silencing triggers efficient recruitment of PRC2 to CpG islands in a genome wide manner, suggesting that PRC2 by default binds to non-transcribed CpG islands [37]. Considering the above, it is intriguing that the prime genomic feature which distinguishes KSHV from MHV-68 is CpG suppression, with MHV-68 showing much more severe suppression compared to KSHV (suppression index of 0.43 and 0.82, respectively). Indeed, when using common definition criteria almost the entire KSHV genome scores as a single, contiguous CpG island, whereas only short interspersed segments meet the requirements in the MHV-68 genome (S5 Fig). The fact that KDM2B efficiently binds to de novo infecting KSHV genomes, and that H3K36-me2 levels are substantially lower on KSHV compared to MHV-68 genomes further supports the hypothesis that CpG frequency may drive rapid accumulation of H3K27-me3 marks on KSHV episomes via the non-canoncial PRC1.1. Certainly, additional studies will be required to investigate the role of KDM2B and non-canonical PRC complexes in latency establishment. For example, thus far we have been unable to generate viable knockout or knockdown cells in which KDM2B levels were substantially reduced, and the overall impact of KDM2B and PRC1.1 activity on H3K27-me3 accumulation and silencing of lytic KSHV genes therefore remains unknown. We are currently targeting other components of PRC1.1 to further investigate this issue. In the meantime, the working model presented in Fig 10 may provide a potential explanation of the observations made in the present study, and may also serve as a basis to inform future studies by our and other groups. We propose that, for KSHV as well as MHV-68, one of the earliest events after

bioRxiv preprint first posted online May. 15, 2019; doi: http://dx.doi.org/10.1101/639898. The copyright holder for this preprint (which was not peer-reviewed) is the author/funder, who has granted bioRxiv a license to display the preprint in perpetuity. It is made available under a CC-BY 4.0 International license.

nuclear entry is the binding of sequence-specific transcription factors of hitherto unknown nature, leading to recruitment of chromatin modifiers (including H3K4 specific methyltransferases such as MLL and SET2) that demark the observed patterns of activation-associated histone modifications on latent genomes. In KSHV, the high density of unmethylated CpG motifs results in rapid acquisition of non-canonical PRC1.1 via its KDM2B component and subsequent PRC2 recruitment. Secondary recruitment of PRC2 has recently been shown to be promoted by H2AK119-ub marks deposited by PRC1 [33], and a similar order of events for KSHV genomes is suggested by the data presented in Fig 9 together with the previous finding that binding of RYBP, a component of non-canonical PRC1 complexes, precedes that of the PRC2 component EZH2 [7]. However, given recent reports of methylation sensitive DNA binding by PRC2-accessory proteins of the Polycomblike family [38-40], PRC2 may also be able to directly bind to non-methylated KSHV DNA.

While the lower CpG frequency of MHV-68 genomes does not allow rapid genome-wide recruitment of PRC complexes, our data suggest that the internal repeat regions may nevertheless serve as seed regions for polycomb acquisition. This hypothesis is also supported by the fact that the left internal repeat region has been previously found to be important for latency amplification in vivo [41]. In the right panel of Fig 10 we have therefore depicted a scenario in which PRC1.1 binds initially at CpG-rich (repeat) regions of the MHV-68 genome in a delayed manner (or as the result of a stochastically rare event), followed by spreading of PRCs and associated histone modifications sites via canonical complexes. As discussed above, whether or not PRC acquisition by MHV-68 is facilitated by splenocyte-specific factors remains to be established.

Given our results, we propose that PRC recruitment may represent a default response to nuclear, epigenetically naive viral genomes that harbor a high density of non-methylated CpG motifs, and that different viruses may have adopted different strategies to exploit, delay or evade this process. In this context, KSHV LANA may have evolved to further stimulate PRC2 binding and thus promote rapid latency establishment, whereas CpG depletion in MHV-68 genomes may reflect a lifestyle that is more prone to initial lytic replication in the lung, followed by selection of repressed genomes in splenic long-

bioRxiv preprint first posted online May. 15, 2019; doi: http://dx.doi.org/10.1101/639898. The copyright holder for this preprint (which was not peer-reviewed) is the author/funder, who has granted bioRxiv a license to display the preprint in perpetuity. It is made available under a CC-BY 4.0 International license.

667 term latency reservoirs. Interestingly, KDM2B was recently also shown to bind to lytic EBV promoters
668 and repress transcription [42], suggesting that EBV may also employ polycomb repression to support
669 latency. Notably, however, the above does not mean that all CpG-rich DNA viruses will undergo
670 polycomb repression, as they may have evolved other mechanisms to actively interfere with PRC
671 recruitment. While it thus should be of great interest to study polycomb repression in other viruses,
672 we expect that the genetically tractable system and evolutionary informed system presented here will
673 be particularly useful in helping to decipher the molecular mechanisms which direct PRC to
674 epigenetically naive, nuclear-invading DNA.
675
676
677 ## Materials and Methods
678
679 **Cell lines and culture conditions**
680 MLE-12 cells (ATCC; CRL-2110) and SLK_P cells (a pool of long-term infected single cell clones derived
681 from SLK cells infected with the BCBL1 KSHV strain) [4] were grown in DMEM High Glucose (Gibco,
682 Darmstadt, Germany) supplemented with 10% FCS, 2 mM L-Glutamine, 100 U/ml Penicillin and 100
683 µg/ml Streptomycin. S11E cells [16] and BCBL1 cells [43] were cultured in RPMI 1640 medium
684 containing 10% FCS, 100 U/ml Penicillin and 100 µg/ml Streptomycin. SLK_P cells are a permanently
685 KSHV positive cell line. The parental cell line SLK has been recently discovered to be a misidentified cell
686 line (Cellosaurus AC: CVCL_9569) and was identified as a contaminating cell line (Caki-1; Cellosaurus
687 AC: CVCL_0234) and is listed in *ICLAC.* Nevertheless, these cells have been shown to efficiently support
688 KSHV latency as stated in several publications throughout the last years and therefore represent a
689 suitable model cell line to study chromatinization of latent KSHV genomes. All cell lines were regularly
690 tested for mycoplasma contaminations using LookOut® Mycoplasma PCR Detection Kit (Sigma-Aldrich,
691 MP0035-1KT). Additionally ChIP-seq reads from input samples were aligned to mycoplasma reference
692 sequences to exclude contamination.

bioRxiv preprint first posted online May. 15, 2019; doi: http://dx.doi.org/10.1101/639898. The copyright holder for this preprint (which was not peer-reviewed) is the author/funder, who has granted bioRxiv a license to display the preprint in perpetuity. It is made available under a CC-BY 4.0 International license.

693

694 **Generation of kLANA/mLANA expressing MLE12 cells**

695 To generate lentiviral expression constructs for kLANA and mLANA, the respective ORFs were PCR
696 amplified from KSHV and from MHV-68. PCR products were cloned into LeGOiC2 vectors [44].
697 Constructs were verified by Sanger sequencing. Lentiviral particles of LeGo-iC2-kLANA and LeGo-iC2-
698 mLANA were produced in LentiX293 cells. These lentiviral particles were used to transduce MLE12
699 cells. During transduction 8 µg/ml polybrene was added. 8h post transduction medium was changes
700 to complete DMEM. Cells were sorted multiple times to achieve a homogenous population of kLANA
701 and mLANA expressing cells. Successful expression of kLANA and mLANA was verified by Western blot
702 (see Fig 7D).

703

704 **Rodents**

705 Female Balb/c mice (6-8 weeks old) were purchased from Charles River Laboratories (Sulzfeld,
706 Germany) and housed in individually ventilated cages (IVC) during the MHV-68 infection period. All
707 animal experiments were in compliance with the German Animal Welfare Act (German Federal Law §8
708 Abs. 1 TierSchG), and the protocol was approved by the local Animal Care and Use Committee (District
709 Government of Upper Bavaria; permit number 124/08).

710

711 **Viruses and infection**

712 *MHV-68:*

713 Wildtype MHV-68 (ATCC; VR-1465) and MHV-68-H2BYFP [26] was propagated in MLE-12 cells by
714 incubation with infectious virus supernatant resulting in a rapid productive lytic infection. Supernatant
715 was harvested and filtered 72 to 96 hours post infection, when cells showed a visible cytopathic effect
716 (CPE). Infection was performed by incubating $5x10^5$ MLE-12cells with 20 µl of prepared virus
717 supernatant in 600 µl medium containing 8 µg/ml polybrene in a 6-well dish. Cells were cultured in
718 EBM-2 medium without supplements (LONZA) for two hours followed by substitution with culture

bioRxiv preprint first posted online May. 15, 2019; doi: http://dx.doi.org/10.1101/639898. The copyright holder for this preprint (which was not peer-reviewed) is the author/funder, who has granted bioRxiv a license to display the preprint in perpetuity. It is made available under a CC-BY 4.0 International license.

719 medium. For in vivo experiments, mice were inoculated intranasally (i.n.) with 5 x 10^4 PFU of wildtype
720 MHV-68 or MHV-68-H2BYFP. Prior to i.n. inoculation, mice were anesthetized with ketamine and
721 xylazine. After 17 days, when latency is usually established in the majority of infected B-cells, mice
722 were sacrificed and single splenocyte suspensions were prepared by forcing the prepared spleens
723 trough a cell strainer into PBS. Cells were treated with RBC lysis buffer (Biolegend: #240301) and either
724 directly fixed for ChIP or stained for dead cells using the Zombi NIR Fixable Viability Kit (Biolegend:
725 #423106) as per the manufacturer's instructions for subsequent FACS sorting (MHV-68-H2BYFP).
726 Sorted cells were subjected to low cell ChIP and low cell RNA-seq analysis.
727
728 An MHV-68 ORF50 deletion mutant (MHV-68Δ50) was generated by ET-cloning of a GFP expressing
729 MHV-68 BAC construct as described previously [45]. For this purpose, ORF50 was first partially replaced
730 with a tetracycline (Tet) resistance gene flanked by FRT sites. Subsequently, the Tet resistance cassette
731 was removed by FLP-mediated recombination, resulting in a deletion of nucleotides 67,957 to 69,326.
732 The BAC-cloned genome was analyzed by restriction enzyme analysis with several restriction enzymes
733 and high-throughput Illumina sequencing.
734 MHV-68ΔORF50 mutant virus was reconstituted on trans-complementing BHK-21 cells (ATCC; CCL-10)
735 stably expressing ORF50. The latter were generated by transfection of BHK-21 cells with the eukaryotic
736 expression vector pCR3 (Invitrogen) containing an EcoRI - AvaI fragment of MHV-68 (nucleotide
737 positions 65,707 to 69,550). After transfection, cells were cultured in the presence of 500 µg/ml G418
738 (PAA). For virus reconstitution, the ORF50 trans-complementing BHK-21 cells were transfected with 2
739 µg of ΔORF50 BAC DNA using FuGENE HD Transfection Reagent (Roche, Mannheim, Germany). When
740 cells showed a visible CPE, the supernatant was harvested and stored. Virus stocks were grown and
741 titrated as described previously [45], except that ΔORF50 mutant virus stock was grown and titrated
742 on the ORF50 trans-complementing BHK-21 cells. Infection was performed as described for MHV-68
743 (wt), however, we used a higher volume of viral supernatants (20 to 250 µl) since the mutant generally
744 grew to lower titers compared to wild type. To investigate long-term infected cultures, MLE-12 cells

bioRxiv preprint first posted online May. 15, 2019; doi: http://dx.doi.org/10.1101/639898. The copyright holder for this preprint (which was not peer-reviewed) is the author/funder, who has granted bioRxiv a license to display the preprint in perpetuity. It is made available under a CC-BY 4.0 International license.

745 were infected with trans-complemented MHV-68Δ50 virus expressing GFP from the BAC cassette [45].
746 Infected GFP-expressing cells were sorted approximately once per week using a FACS-Aria (BD) to
747 maintain an almost 100% positive cell population for subsequent experiments. Loss rates were
748 estimated to be approximately 5-10% per cell generation, as judged from the ratio of green versus
749 non-fluorescent cells and the number of cell doublings (determined by counting cells during the sub-
750 culturing). Note that these loss rates are only estimates as we did not perform FACS analysis at fixed
751 intervals, or determined the fraction of virally infected cells in which the that GFP reporter may have
752 be transcriptionally silenced.
753
754 To generate MHV-68Δ50-kLANA, the same strategy as decribed above for the MHV-68ΔORF50 mutant
755 was used, except that the ORF50 deletion was introduced in the background of a kLANA-expressing
756 MHV-68 mutant recently generated and kindly provided by Habison and colleagues [21]. Virus
757 supernatants were produced similar to MHV-68Δ50. However, as we only achieved low titers with this
758 construct we used higher volumes of the viral supernatants in our infections experiments (500 ul,
759 diluted 1:2 in EBM-2 containing polybrene at a final concentration of 8 µg/ml polybrene, for infection
760 of 5 x10^5 MLE12 cells seeded into one well of a 6-well plate). The resulting cultures were sorted by
761 FACS and either directly subjected to low cell ChIP, or were subcultured and sorted every 5 to 10 days
762 by FACS to maintain a population of almost 100% infected / GFP-positive cells.
763
764 *KSHV:*
765 Infectious wild-type KSHV supernatant was produced by inducing latently infected BCBL1 cells with
766 TPA (Sigma-Aldrich; Cat#P8139-5MG) and sodium butyrate (Sigma-Aldrich; Cat#B5887-1G) followed
767 by 100x concentration by centrifugation as described previously [4]. For infection, concentrated KSHV
768 stock solutions were diluted in 600 µl EBM-2 medium without supplements (LONZA). Target cells were
769 then incubated with virus for two hours followed by substitution with culture medium.
770

bioRxiv preprint first posted online May. 15, 2019; doi: http://dx.doi.org/10.1101/639898. The copyright holder for this preprint (which was not peer-reviewed) is the author/funder, who has granted bioRxiv a license to display the preprint in perpetuity. It is made available under a CC-BY 4.0 International license.

An ORF73 deletion mutant (KSHV-BAC16Δ73) of KSHV-BAC16 [46] was generated by *en passant* mutagenesis [47]. A PCR product consisting of ORF73 homology sites and a kanamycin resistance gene was generated to replace ORF73 in the KSHV-BAC16 by homologous recombination. In a second recombination step the kanamycin resistance gene was removed to obtain a deletion of nucleotides 140,572 to 143,943. The resulting KSHV-BAC16Δ73 was analyzed by restriction enzyme analysis with multiple restriction enzymes and high-throughput Illumina sequencing.

For the reconstitution of KSHV-BAC16Δ73 infectious viral particles, KSHV-BAC16Δ73 was transfected into iSLK cells [48] stably expressing kLANA with lipofectamine 2000 (ThermoFisher, Cat# 11668019). Two days post transfection, hygromycin selection (200 µg/ml) was initiated to select for bacmid containing cells (200 µg/ml). Virus production was performed as previously described [46]. For infection experiments employing KSHV-BAC16Δ73, 5 x 10^5 MLE12-kLANA or MLE12-mLANA cells were seeded into one well of a 6-well plate, respectively. Cells were infected with 1 ml of virus supernatant of KSHV-BAC16Δ73 supplemented with 8 µg/ml polybrene. 2 hours post infection virus supernatant was removed and replaced by complete DMEM. Cells were subcultured in the presence of hygromycin (200 µg/ml) to maintain a homogenous population of 100% infected cells.

Preparation of total RNA and protein extracts

Total RNA was extracted from MHV-68 infected cells using RNA-Bee (Tel-Test, Inc.; Cat#NC9850755) according to the manufacturer's instructions. RIPA-extracts and Western Blot were performed using standard protocols.

Antibodies

For ChIP the following antibodies were used in this study: Rabbit polyclonal anti H3K9/K14-ac (Merck Millipore; Cat#06-599); Rabbit monoclonal anti H3K4-me3 (clone MC315) (Merck Millipore; Cat#04-745); Rabbit polyclonal anti H3K9-me3 (Merck Millipore;Cat#17-625); Rabbit polyclonal H3K36me2 (MerckMillipore; Cat#07-274); Rabbit monoclonal H3K36me3 (Cell Signaling; Cat#4909S); Rabbit

bioRxiv preprint first posted online May. 15, 2019; doi: http://dx.doi.org/10.1101/639898. The copyright holder for this preprint (which was not peer-reviewed) is the author/funder, who has granted bioRxiv a license to display the preprint in perpetuity. It is made available under a CC-BY 4.0 International license.

polyclonal JHDM1B/KDM2B (Merck Millipore; Cat#17-102-64, successfully tested in ChIP-seq: LOT 2135462, tested but non-functional in ChIP-seq: LOT 2756112 and LOT 3096002); Normal rabbit IgG (Merck Millipore;Cat#12-370). For detection of LANA expression the following antibodies were used: anti-kLANA rabbit polyclonal Ab, rabbit mLANA antiserum [49], and anti-ß-Actin mouse monoclonal Ab (Santa Cruz Biotechnology, Cat# sc-47778). The following secondary antibodies conjugated to horseradish peroxidase were used for western blot detection: Anti-rabbit IgG (Santa Cruz Biotechnology, Cat# sc-2004) and anti-mouse IgG (Invitrogen, Cat# 31431).

Chromatin-immunoprecipitation (ChIP)

ChIP was performed essentially as described in detail previously [6]. Briefly, cells were treated with 1 % formaldehyde in PBS for 10 min to crosslink proteins and DNA. Reactions were quenched by addition of glycine to a final concentration of 0.125 M. All buffers contained 1x protease inhibitor cocktail (Roche) and 1 mM PMFS. Cells were incubated in 1 ml buffer 1 (50 mM Hepes-KOH, 140 mM NaCl, 1 mM EDTA, 10% glycerol, 0.5% NP-40, 0.25% Triton X-100) for 10 min on ice to isolate nuclei. After centrifugation (1,350 x g 5 min), nuclei were washed with 1 ml buffer 2 (10 mM Tris-HCl, 200 mM NaCl, 1 mM EDTA, 0.5 mM EGTA). Pelleted nuclei were lysed in 1 ml buffer 3 (1% SDS, 10 mM EDTA, 50 mM Tris-HCl) by multiple pipetting and chromatin was fragmented to approximately nucleosome size using a BioruptorTM (Diagenode). After addition of 100 µl 10% Triton X-100 Cell debris was pelleted (20,000 x g, 4°C) and chromatin containing supernatant was collected. Chromatin of $1x10^6$ cells was diluted 1:10 in dilution buffer (0.01 % SDS, 1.1 % Triton X-100, 1.2 mM EDTA, 16.7 mM Tris-HCl, 167 mM NaCl). 10µg of the respective antibody was added to the sample and incubated for 16 hrs at 4°C rotating. 50 µl BSA-blocked ProteinG sepharose beads (GE Healthcare) were added to precipitate the chromatin-immunocomplexes and incubated for 1 hr at 4°C. Beads were washed once with 1ml of the following buffers: low-salt buffer (0.1 % SDS, 1 % Triton X-100, 2 mM EDTA, 20 mM Tris-HCl, 150 mM NaCl); high-salt buffer (0.1 % SDS, 1 % Triton X-100, 2 mM EDTA, 20 mM Tris-HCl, 500 mM NaCl); LiCl-wash buffer

bioRxiv preprint first posted online May. 15, 2019; doi: http://dx.doi.org/10.1101/639898. The copyright holder for this preprint (which was not peer-reviewed) is the author/funder, who has granted bioRxiv a license to display the preprint in perpetuity. It is made available under a CC-BY 4.0 International license.

(0.25 M LiCl, 1 % Nonidet P-40, 1 % Na-deoxycholate, 1 mM EDTA, 10 mM Tris-HCl). Subsequently, beads were washed two times with TE buffer without protease inhibitors. Chromatin was eluted from the beads by incubation in 210 µl SDS containing elution-buffer (50 mM Tris-HCl pH 8.0, 10 mM EDTA, 1 % SDS) for 30 min at 65°C. Chromatin containing supernatant was separated from the beads by centrifugation. After addition of 8 µl of a 5 M NaCl stock solution chromatin was de-crosslinked at 65°C overnight. Contaminating RNA was degraded by addition of 200µl TE buffer containing 8 µl RNAseA (10 mg/ml) for 2 hrs at 37°C. Subsequently, 7 µl of $CaCl_2$ solution (300 mM $CaCl_2$ in 10 mM Tris-HCl) and 4 µl ProteinaseK (40 mg/ml) were added and incubated for 1h at 55°C to degrade proteins. DNA was purified by phenol-chloroform extraction and ethanol precipitation. Input DNA samples were diluted in 200µl elution buffer and treated identically to the ChIP samples beginning with overnight de-crosslinking. Finally, DNA was recoverd in 10 mM Tris-HCl and was either subjected to ChIP-seq library preparation or was analysed directly by ChIP-qPCR.

For Low cell ChIP we combined different protocols to facilitate efficient fragmentation of low numbers of cross-linked cells and library preparation from spurious amounts of DNA. Cell fixation was performed using the fixation reagents and steps from the Low Cell Chip Kit (Active Motif; Cat#53084) as described in the user manual. Samples were then treated with MNase according to the 'MNase followed by sonication' protocol described earlier [50]. Briefly, 200µl fixated samples containing 2000 to 9000 cells (depending on the sample) were diluted to a total volume of 200µl in dilution buffer supplemented with 3mM $CaCl_2$. After incubation at 37°C for 15 minutes, MNase reaction was stopped by adding EDTA (10 mM final concentration) and EGTA (20 mM final concentration). Samples were sonicated using a Bioruptor similar to the ChIP protocol above for 10 cycles. After addition of Triton X-100 (0.1% final concentration) cell debris was removed via centrifugation. Total supernatant was collected and 400 µl were separated to serve as an input control. Chromatin precipitation was performed essentially as described in the ChIP section above only omitting the addition of $CaCl_2$ during Proteinase K digestion of the input sample to prevent residual MNase activity therein. Sequencing

bioRxiv preprint first posted online May. 15, 2019; doi: http://dx.doi.org/10.1101/639898. The copyright holder for this preprint (which was not peer-reviewed) is the author/funder, who has granted bioRxiv a license to display the preprint in perpetuity. It is made available under a CC-BY 4.0 International license.

848 libraries of low chip samples and input was performed using the library preparation reagents of the
849 Low Cell Chip Kit.

850

851 **ChIP-qPCR**

852 Relative enrichment of ChIP DNA was determined by qPCR and is presented as % of input. All primer
853 used in this study are given in Table 1. Standard curves were generated for all primer sets to ensure
854 efficient amplification. Specificity to the respective target site was assessed by melt curve analysis. All
855 samples were analyzed on a Rotorgene 6000 qPCR machine (QIAgen) using the SensiMix™ SYBR® Hi-
856 ROX Kit (Bioline, Cat#QT605-05).

857 **Table 1. Primers used in this study.**

	Primer1	**Primer2**
kORF23	ACACGACACGATGTTTTCCA	TCATGGAGCGTGCTAACAAC
kORF43	CTACCGTGACCACCCAGTCT	CTGCTTCTCAATGCCATCAA
kORF50-800pro	TCCGAGGTAATGTGCTCTATGAAG	ACAGACACCGGAGCAATACCC
kvIRF3in	AAAAATTCGCCAACAACTGG	CCAGAATGTAGCAGGGGAAT
kvIRF3pro	GCGGTAAGACAAAGGGAGGT	TACCTTGCCCCATTTTACCA
kORF73pro	CCCGTGCTGACATAGTTAGCG	GGTACTGGGTCTGAACCACCAC
kORF75pro	AGCGAGCACCGTCTGTATTT	GCACCGGAGGCTACTATCTG
mMYT1	CAGCCCAATTCTAGCCACAT	CCAAAGCAGGGGAGTAGGAG
mGAPDH	GGTCCAAAGAGAGGGAGGAG	GCCCTGCTTATCCAGTCCTA
mRPL30	AGAACAAACGCCCAGAACC	TGCGAGAGTAGTCTGCGGTA
mPitx3	CCTGGGTTGCCATAAAGTGA	GCTAGCGGAGGAGAGAGTGA
mArid3c	TGGCCAGGAACTGAGGATAG	GATCTCCCTGCACCACTCTC
m1in	CCCTACCAGACACCTGCAAT	AGAAGCCATGGTGGGTAGTG
mORF4	TTGGGCTTCCTGATAACCAG	GCCAAACATGTGAGTCATGG
mORF9	AGGGTGTGGATCTTGTCAGG	AATCAGGGAGACCACGTTTG
mORF11in	GTCTTCACAGCCGTCTTTCC	GCAGCTTCACTGACACCAGA
mM5pro	TTGAAACTTCCCACGGAGTC	GGCACGCTTCAAAAAGTCTC
mORF32	CTGCAACCAAGTGTCCAGTG	GGGCAACAAAGACAGGAGAA
mORF36pro	CTCCGAGCAAGAGGAGAGTG	CTCCATCCTCACCCAATACG
mORF44	TGGGATCTCCAACTCAGACC	TTTGGATCTCGTTCCTTTGG
mRTApro1	ACGGGTTTCAAGGTCCATTT	GCTCTCTCCTCAGCCTTTGA
mRTApro2	AATTGAAACCTGCTGGCAAC	CTGCAGCACATTGTGGGATA
mORF64	AGTCCAGCCCACGTACTCAG	GCAGTATATTCGCGGGACAC
mORF72post2	AATGCGCTTTTTCTGTGAGG	CGGTTAGACCAGGCAAAAAC
mM13	CTACCTGTTTTGGCCCTCAG	GAGGCCCCCTACTAGACACC

858

bioRxiv preprint first posted online May. 15, 2019; doi: http://dx.doi.org/10.1101/639898. The copyright holder for this preprint (which was not peer-reviewed) is the author/funder, who has granted bioRxiv a license to display the preprint in perpetuity. It is made available under a CC-BY 4.0 International license.

859

860 **Library preparation and sequencing**

861 ChIP and respective input libraries were prepared from 2-10 ng DNA using the NEXTflex Illumina ChIP-
862 Seq Library Prep Kit (Bioo Scientific; Cat#5143-02) according to the manufacturer´s instructions. For
863 RNA-seq, quality of extracted total RNA was verified prior to library preparation on a 2100 Bioanalyzer
864 (Agilent). Strand specific Illumina compatible paired end ssRNA-seq libraries were generated using the
865 NextFlex Directional RNA-Seq Kit (Bioo Scientific; Cat#5129-08) as per the manufacturer's
866 recommendations. Low cell RNA-seq libraries (unstranded) wer generated withSMART-Seq v4 Ultra
867 Low Input RNA Kit for Sequencing (Takara/ Clonetech; Cat#634890). All sequencing libraries were
868 sequenced on a HiSeq 2500 system (Illumina) using paired end (2x100bp) or single read (1x50) flow
869 cells for RNA-seq and ChIP, respectively, or on a NextSeq 500 (Illumina) using single read (1x75) flow
870 cells for ChIP and low cell RNA-seq.

871

872

873 **Sequencing data analysis**

874

875 *ChIP-seq*

876 Quality filtered single end reads were aligned to the viral reference genomes of MHV-68 (NC_001826)
877 and KSHV (HQ404500) as well as to the mouse (mm10) and human genomes (hg19) using Bowtie [51]
878 with standard settings and the –m 1 option set to exclude multi mapping reads. Coverage calculation
879 for visualization purpose was performed with IGV-Tools [52]. All coverage datasets used to generate
880 graphs shown in Figs 1, 5, 6, 7, 8, 9, S2 Fig and S6 Fig are provided in S1 Dataset. For visualization
881 purposes, ChIP-seq graphs were adjusted by subtracting the lower 5th percentile to remove
882 background signals [6]. Analysis and heatmap visualization of KDM2B ChIP-seq data as well as global
883 H3K27-me3 and H3K36-me2 anti-correlation analysis was performed with EaSeq (http://easeq.net)
884 [53].

bioRxiv preprint first posted online May. 15, 2019; doi: http://dx.doi.org/10.1101/639898. The copyright holder for this preprint (which was not peer-reviewed) is the author/funder, who has granted bioRxiv a license to display the preprint in perpetuity. It is made available under a CC-BY 4.0 International license.

Statistical analysis of histone modification and KDM2B enrichment on viral genomes

To calculate the relative enrichment of broad histone modifications H3K27-me3, H3K36-me2 and H2AK119-ubon viral genomes in comparison to the respective host genomes, we first detected all regions significantly enriched for the respective histone mark on the host genome against their input samples as controls using SICER/EPIC2 [54]. The 200 most significant (based on p-value) broadly enriched regions median sizes (15 to 40 kb for individual experiments) were selected as host positive regions and are named host pos in Figs 4, 5, 6, 7, 8 and in S7 Fig . The negative regions, which represent the general ChIP background of each individual analysis (host neg in the respective figures), were generated by random selection of regions with the same size distribution as the positive controls. We excluded SICER/EPIC2-positive regions as well as all regions with less than 10 reads per region in the input samples (the latter prevents selection of unmappable regions, e.g. in repetitive elements, in the negative controls) as well as all regions with known mappability bias (blacklists downloaded from ENCODE). Viral sequences were split into segments of 10kb (shifted by 5kb) to reflect broad regions. We counted the reads within each pos, neg and viral region using FeatureCounts. For each individual region we then calculated the ChIP to input read count ratio and normalized all groups to the median of the respective negative control. The resulting values represent relative enrichment of the respective broad histone modification signals over the general ChIP background present in each individual experiment. For quantification of relative KDM2B enrichment on the viral genome in comparison to host target loci (Fig 9), we detected KDM2B-bound sites using MACS peak calling similar to H3K4-me3 peak calling, selected control regions by FDR and performed the same analysis described above using 2kb windows (shifted by 1kb) for the KSHV genome.

Correlation coefficients

Correlation coefficients of ChIP tracks were generated using GraphPad Prism and are presented in S2 Dataset.

bioRxiv preprint first posted online May. 15, 2019; doi: http://dx.doi.org/10.1101/639898. The copyright holder for this preprint (which was not peer-reviewed) is the author/funder, who has granted bioRxiv a license to display the preprint in perpetuity. It is made available under a CC-BY 4.0 International license.

911

912 *RNA-seq analysis*

913 Quality filtered paired end reads were aligned to the MHV-68 sequence (NC_001826), to KSHV
914 (HQ404500) as well as to the mouse genome (mm9) using the spliced read mapper STAR allowing for
915 the detection of novel splice events in combination with FeatureCounts [55, 56]. For visualization
916 purposes, coverage of both strands was calculated individually.
917 For ***expression analysis*** of MHV-68 encoded ORFs (Fig 2B and S2 Fig), all ORFs annotated in NC_001826
918 were assigned as single exons and genes in GFF3 format. Since the precise structure of mRNAs is not
919 available for most ORFs, we evaluated coverage of coding regions to estimate viral transcription of
920 individual gene products. Therefore, we restricted the analysis of viral gene expression by reads
921 matching unique ORF regions only and ignored reads that could not be assigned to specific ORFs.
922 Aligned reads were counted using FeatureCounts. Resulting feature counts of all viral ORFs in individual
923 samples were normalized by the total number of reads that were aligned to the murine genome (mm9)
924 by STAR. At later stages of lytic transcription, this normalization method may lead to an overestimation
925 of general viral transcript levels but not to differences of the expression profile within each individual
926 sample. Resulting data are given in S3 Dataset in raw and normalized format. Fig 2C depicts relative
927 normalized expression data with the detection threshold set to a minimum of 10 reads per ORF.

928

929

930 **Statistical Information**

931 For all figures containing statistical testing, we ensured that use of the respective test was justified as
932 being appropriate and meeting the respective assumptions. For Figs 4, 5B, 6B, 7C, 8C, 9B and S7 Fig,
933 data is presented as box-whisker-plot with 5th-95th percentile and mean (+). Significance was
934 calculated by 1way ANOVA testing using GraphPad Prism. For Fig 5C, ChIP-qPCR data is presented as
935 mean with SEM of three technical replicate ChIP-qPCR datasets normalized to the respective
936 endogenous controls for H3K4-me3 and H3K27-me3 mGAPDH and mMYT1 using the primers given in

bioRxiv preprint first posted online May. 15, 2019; doi: http://dx.doi.org/10.1101/639898. The copyright holder for this preprint (which was not peer-reviewed) is the author/funder, who has granted bioRxiv a license to display the preprint in perpetuity. It is made available under a CC-BY 4.0 International license.

Table 1. This ChIP-qPCR dataset originates from a third independent superinfection experiment that was performed to validate the two biological replicate ChIP-seq datasets of Fig 5B. For Fig 6C and 7A presented error bars represent SEM of at least two replicate experiments (for n see individual figure legends). For Fig 8A, ChIP-qPCR data is presented as mean with SEM of three technical replicate ChIP-qPCR experiments. The two independent datasets were generated from two mice that were de novo infected with MHV-68.

Data Availability

All raw sequencing datasets used in this study will be made available via the European Nucleotide after peer review and formal acceptance of this article.

Acknowledgements

We thank Kenneth M. Kaye and J. Pedro Simas for kindly providing the chimeric MHV68-kLANA bacmid, and Samuel H. Speck for kindly providing MHV-68-H2BYFP. We thank Daniela Indenbirken, Henry Scheibel, Kerstin Reumann and and Beatrix Steer for technical assistance, and Simon Weissmann and Nicole Fischer for helpful discussions and critical reading of the manuscript.

bioRxiv preprint first posted online May. 15, 2019; doi: http://dx.doi.org/10.1101/639898. The copyright holder for this preprint (which was not peer-reviewed) is the author/funder, who has granted bioRxiv a license to display the preprint in perpetuity. It is made available under a CC-BY 4.0 International license.

References

1. Schulz TF, Cesarman E. Kaposi Sarcoma-associated Herpesvirus: mechanisms of oncogenesis. Curr Opin Virol. 2015;14:116-28. doi: 10.1016/j.coviro.2015.08.016. PubMed PMID: 26431609.
2. Dittmer DP, Damania B. Kaposi sarcoma-associated herpesvirus: immunobiology, oncogenesis, and therapy. J Clin Invest. 2016;126(9):3165-75. doi: 10.1172/JCI84418. PubMed PMID: 27584730; PubMed Central PMCID: PMCPMC5004954.
3. Juillard F, Tan M, Li S, Kaye KM. Kaposi's Sarcoma Herpesvirus Genome Persistence. Front Microbiol. 2016;7:1149. doi: 10.3389/fmicb.2016.01149. PubMed PMID: 27570517; PubMed Central PMCID: PMCPMC4982378.
4. Grundhoff A, Ganem D. Inefficient establishment of KSHV latency suggests an additional role for continued lytic replication in Kaposi sarcoma pathogenesis. J Clin Invest. 2004;113(1):124-36. Epub 2004/01/01. doi: 10.1172/JCI17803. PubMed PMID: 14702116; PubMed Central PMCID: PMC300762.
5. Bechtel JT, Liang Y, Hvidding J, Ganem D. Host range of Kaposi's sarcoma-associated herpesvirus in cultured cells. J Virol. 2003;77(11):6474-81. PubMed PMID: 12743304; PubMed Central PMCID: PMCPMC155009.
6. Günther T, Grundhoff A. The epigenetic landscape of latent Kaposi sarcoma-associated herpesvirus genomes. PLoS Pathog. 2010;6(6):e1000935. Epub 2010/06/10. doi: 10.1371/journal.ppat.1000935. PubMed PMID: 20532208; PubMed Central PMCID: PMC2880564.
7. Toth Z, Brulois K, Lee HR, Izumiya Y, Tepper C, Kung HJ, et al. Biphasic euchromatin-to-heterochromatin transition on the KSHV genome following de novo infection. PLoS Pathog. 2013;9(12):e1003813. doi: 10.1371/journal.ppat.1003813. PubMed PMID: 24367262; PubMed Central PMCID: PMCPMC3868514.
8. Günther T, Schreiner S, Dobner T, Tessmer U, Grundhoff A. Influence of ND10 components on epigenetic determinants of early KSHV latency establishment. PLoS Pathog. 2014;10(7):e1004274. Epub 2014/07/18. doi: 10.1371/journal.ppat.1004274. PubMed PMID: 25033267; PubMed Central PMCID: PMC4102598.
9. Hilton IB, Simon JM, Lieb JD, Davis IJ, Damania B, Dittmer DP. The open chromatin landscape of Kaposi's sarcoma-associated herpesvirus. J Virol. 2013;87(21):11831-42. doi: 10.1128/JVI.01685-13. PubMed PMID: 23986576; PubMed Central PMCID: PMCPMC3807352.
10. Sun R, Tan X, Wang X, Wang X, Yang L, Robertson ES, et al. Epigenetic Landscape of Kaposi's Sarcoma-Associated Herpesvirus Genome in Classic Kaposi's Sarcoma Tissues. PLoS Pathog. 2017;13(1):e1006167. doi: 10.1371/journal.ppat.1006167. PubMed PMID: 28118409; PubMed Central PMCID: PMCPMC5291540.
11. Toth Z, Maglinte DT, Lee SH, Lee HR, Wong LY, Brulois KF, et al. Epigenetic analysis of KSHV latent and lytic genomes. PLoS Pathog. 2010;6(7):e1001013. Epub 2010/07/28. doi: 10.1371/journal.ppat.1001013. PubMed PMID: 20661424; PubMed Central PMCID: PMC2908616.
12. Hopcraft SE, Pattenden SG, James LI, Frye S, Dittmer DP, Damania B. Chromatin remodeling controls Kaposi's sarcoma-associated herpesvirus reactivation from latency. PLoS Pathog. 2018;14(9):e1007267. doi: 10.1371/journal.ppat.1007267. PubMed PMID: 30212584; PubMed Central PMCID: PMCPMC6136816.
13. Toth Z, Papp B, Brulois K, Choi YJ, Gao SJ, Jung JU. LANA-Mediated Recruitment of Host Polycomb Repressive Complexes onto the KSHV Genome during De Novo Infection. PLoS Pathog. 2016;12(9):e1005878. doi: 10.1371/journal.ppat.1005878. PubMed PMID: 27606464; PubMed Central PMCID: PMCPMC5015872.
14. Marques S, Efstathiou S, Smith KG, Haury M, Simas JP. Selective gene expression of latent murine gammaherpesvirus 68 in B lymphocytes. J Virol. 2003;77(13):7308-18. Epub 2003/06/14. PubMed PMID: 12805429; PubMed Central PMCID: PMC164786.

bioRxiv preprint first posted online May. 15, 2019; doi: http://dx.doi.org/10.1101/639898. The copyright holder for this preprint (which was not peer-reviewed) is the author/funder, who has granted bioRxiv a license to display the preprint in perpetuity. It is made available under a CC-BY 4.0 International license.

15. Tarakanova VL, Suarez F, Tibbetts SA, Jacoby MA, Weck KE, Hess JL, et al. Murine gammaherpesvirus 68 infection is associated with lymphoproliferative disease and lymphoma in BALB beta2 microglobulin-deficient mice. J Virol. 2005;79(23):14668-79. Epub 2005/11/12. doi: 10.1128/JVI.79.23.14668-14679.2005. PubMed PMID: 16282467; PubMed Central PMCID: PMC1287585.
16. Usherwood EJ, Stewart JP, Nash AA. Characterization of tumor cell lines derived from murine gammaherpesvirus-68-infected mice. J Virol. 1996;70(9):6516-8. Epub 1996/09/01. PubMed PMID: 8709292; PubMed Central PMCID: PMC190690.
17. Gray KS, Allen RD, 3rd, Farrell ML, Forrest JC, Speck SH. Alternatively initiated gene 50/RTA transcripts expressed during murine and human gammaherpesvirus reactivation from latency. J Virol. 2009;83(1):314-28. Epub 2008/10/31. doi: 10.1128/JVI.01444-08. PubMed PMID: 18971285; PubMed Central PMCID: PMC2612301.
18. Yang Z, Tang H, Huang H, Deng H. RTA promoter demethylation and histone acetylation regulation of murine gammaherpesvirus 68 reactivation. PLoS One. 2009;4(2):e4556. Epub 2009/02/24. doi: 10.1371/journal.pone.0004556. PubMed PMID: 19234612; PubMed Central PMCID: PMC2644783.
19. Martinez-Guzman D, Rickabaugh T, Wu TT, Brown H, Cole S, Song MJ, et al. Transcription program of murine gammaherpesvirus 68. J Virol. 2003;77(19):10488-503. Epub 2003/09/13. PubMed PMID: 12970434; PubMed Central PMCID: PMC228380.
20. Zang C, Schones DE, Zeng C, Cui K, Zhao K, Peng W. A clustering approach for identification of enriched domains from histone modification ChIP-Seq data. Bioinformatics. 2009;25(15):1952-8. doi: 10.1093/bioinformatics/btp340. PubMed PMID: 19505939; PubMed Central PMCID: PMCPMC2732366.
21. Habison AC, de Miranda MP, Beauchemin C, Tan M, Cerqueira SA, Correia B, et al. Cross-species conservation of episome maintenance provides a basis for in vivo investigation of Kaposi's sarcoma herpesvirus LANA. PLoS Pathog. 2017;13(9):e1006555. doi: 10.1371/journal.ppat.1006555. PubMed PMID: 28910389; PubMed Central PMCID: PMCPMC5599060.
22. Pires de Miranda M, Quendera AP, McVey CE, Kaye KM, Simas JP. In Vivo Persistence of Chimeric Virus after Substitution of the Kaposi's Sarcoma-Associated Herpesvirus LANA DNA Binding Domain with That of Murid Herpesvirus 4. J Virol. 2018;92(21). doi: 10.1128/JVI.01251-18. PubMed PMID: 30111565; PubMed Central PMCID: PMCPMC6189500.
23. Gupta A, Oldenburg DG, Salinas E, White DW, Forrest JC. Murine Gammaherpesvirus 68 Expressing Kaposi Sarcoma-Associated Herpesvirus Latency-Associated Nuclear Antigen (LANA) Reveals both Functional Conservation and Divergence in LANA Homologs. J Virol. 2017;91(19). doi: 10.1128/JVI.00992-17. PubMed PMID: 28747501; PubMed Central PMCID: PMCPMC5599733.
24. Habison AC, Beauchemin C, Simas JP, Usherwood EJ, Kaye KM. Murine gammaherpesvirus 68 LANA acts on terminal repeat DNA to mediate episome persistence. J Virol. 2012;86(21):11863-76. doi: 10.1128/JVI.01656-12. PubMed PMID: 22915819; PubMed Central PMCID: PMCPMC3486315.
25. De Leo A, Deng Z, Vladimirova O, Chen HS, Dheekollu J, Calderon A, et al. LANA oligomeric architecture is essential for KSHV nuclear body formation and viral genome maintenance during latency. PLoS Pathog. 2019;15(1):e1007489. doi: 10.1371/journal.ppat.1007489. PubMed PMID: 30682185; PubMed Central PMCID: PMCPMC6364946.
26. Collins CM, Speck SH. Tracking murine gammaherpesvirus 68 infection of germinal center B cells in vivo. PLoS One. 2012;7(3):e33230. doi: 10.1371/journal.pone.0033230. PubMed PMID: 22427999; PubMed Central PMCID: PMCPMC3302828.
27. van Kruijsbergen I, Hontelez S, Veenstra GJ. Recruiting polycomb to chromatin. Int J Biochem Cell Biol. 2015;67:177-87. doi: 10.1016/j.biocel.2015.05.006. PubMed PMID: 25982201; PubMed Central PMCID: PMCPMC4564301.

bioRxiv preprint first posted online May. 15, 2019; doi: http://dx.doi.org/10.1101/639898. The copyright holder for this preprint (which was not peer-reviewed) is the author/funder, who has granted bioRxiv a license to display the preprint in perpetuity. It is made available under a CC-BY 4.0 International license.

28. Laugesen A, Hojfeldt JW, Helin K. Molecular Mechanisms Directing PRC2 Recruitment and H3K27 Methylation. Mol Cell. 2019;74(1):8-18. doi: 10.1016/j.molcel.2019.03.011. PubMed PMID: 30951652; PubMed Central PMCID: PMCPMC6452890.
29. He J, Kallin EM, Tsukada Y, Zhang Y. The H3K36 demethylase Jhdm1b/Kdm2b regulates cell proliferation and senescence through p15(Ink4b). Nat Struct Mol Biol. 2008;15(11):1169-75. doi: 10.1038/nsmb.1499. PubMed PMID: 18836456; PubMed Central PMCID: PMCPMC2612995.
30. Farcas AM, Blackledge NP, Sudbery I, Long HK, McGouran JF, Rose NR, et al. KDM2B links the Polycomb Repressive Complex 1 (PRC1) to recognition of CpG islands. Elife. 2012;1:e00205. doi: 10.7554/eLife.00205. PubMed PMID: 23256043; PubMed Central PMCID: PMCPMC3524939.
31. Wu X, Johansen JV, Helin K. Fbxl10/Kdm2b recruits polycomb repressive complex 1 to CpG islands and regulates H2A ubiquitylation. Mol Cell. 2013;49(6):1134-46. doi: 10.1016/j.molcel.2013.01.016. PubMed PMID: 23395003.
32. He J, Shen L, Wan M, Taranova O, Wu H, Zhang Y. Kdm2b maintains murine embryonic stem cell status by recruiting PRC1 complex to CpG islands of developmental genes. Nat Cell Biol. 2013;15(4):373-84. doi: 10.1038/ncb2702. PubMed PMID: 23502314; PubMed Central PMCID: PMCPMC4078788.
33. Blackledge NP, Farcas AM, Kondo T, King HW, McGouran JF, Hanssen LL, et al. Variant PRC1 complex-dependent H2A ubiquitylation drives PRC2 recruitment and polycomb domain formation. Cell. 2014;157(6):1445-59. doi: 10.1016/j.cell.2014.05.004. PubMed PMID: 24856970; PubMed Central PMCID: PMCPMC4048464.
34. Streubel G, Watson A, Jammula SG, Scelfo A, Fitzpatrick DJ, Oliviero G, et al. The H3K36me2 Methyltransferase Nsd1 Demarcates PRC2-Mediated H3K27me2 and H3K27me3 Domains in Embryonic Stem Cells. Mol Cell. 2018;70(2):371-9 e5. doi: 10.1016/j.molcel.2018.02.027. PubMed PMID: 29606589.
35. Schwartz YB, Pirrotta V. Ruled by ubiquitylation: a new order for polycomb recruitment. Cell Rep. 2014;8(2):321-5. doi: 10.1016/j.celrep.2014.07.001. PubMed PMID: 25061856.
36. Lee TI, Jenner RG, Boyer LA, Guenther MG, Levine SS, Kumar RM, et al. Control of developmental regulators by Polycomb in human embryonic stem cells. Cell. 2006;125(2):301-13. doi: 10.1016/j.cell.2006.02.043. PubMed PMID: 16630818; PubMed Central PMCID: PMCPMC3773330.
37. Riising EM, Comet I, Leblanc B, Wu X, Johansen JV, Helin K. Gene silencing triggers polycomb repressive complex 2 recruitment to CpG islands genome wide. Mol Cell. 2014;55(3):347-60. doi: 10.1016/j.molcel.2014.06.005. PubMed PMID: 24999238.
38. Perino M, van Mierlo G, Karemaker ID, van Genesen S, Vermeulen M, Marks H, et al. MTF2 recruits Polycomb Repressive Complex 2 by helical-shape-selective DNA binding. Nat Genet. 2018;50(7):1002-10. doi: 10.1038/s41588-018-0134-8. PubMed PMID: 29808031.
39. Li H, Liefke R, Jiang J, Kurland JV, Tian W, Deng P, et al. Polycomb-like proteins link the PRC2 complex to CpG islands. Nature. 2017;549(7671):287-91. doi: 10.1038/nature23881. PubMed PMID: 28869966; PubMed Central PMCID: PMCPMC5937281.
40. Choi J, Bachmann AL, Tauscher K, Benda C, Fierz B, Muller J. DNA binding by PHF1 prolongs PRC2 residence time on chromatin and thereby promotes H3K27 methylation. Nat Struct Mol Biol. 2017;24(12):1039-47. doi: 10.1038/nsmb.3488. PubMed PMID: 29058710.
41. Thakur NN, El-Gogo S, Steer B, Freimuller K, Waha A, Adler H. A gammaherpesviral internal repeat contributes to latency amplification. PLoS One. 2007;2(8):e733. doi: 10.1371/journal.pone.0000733. PubMed PMID: 17710133; PubMed Central PMCID: PMCPMC1939874.
42. Vargas-Ayala RC, Jay A, Manara F, Maroui MA, Hernandez-Vargas H, Diederichs A, et al. Interplay between the epigenetic enzyme lysine (K)-specific demethylase 2B and Epstein-Barr virus infection. J Virol. 2019. doi: 10.1128/JVI.00273-19. PubMed PMID: 30996097.
43. Renne R, Zhong W, Herndier B, McGrath M, Abbey N, Kedes D, et al. Lytic growth of Kaposi's sarcoma-associated herpesvirus (human herpesvirus 8) in culture. Nat Med. 1996;2(3):342-6. Epub 1996/03/01. PubMed PMID: 8612236.

bioRxiv preprint first posted online May. 15, 2019; doi: http://dx.doi.org/10.1101/639898. The copyright holder for this preprint (which was not peer-reviewed) is the author/funder, who has granted bioRxiv a license to display the preprint in perpetuity. It is made available under a CC-BY 4.0 International license.

44. Weber K, Bartsch U, Stocking C, Fehse B. A multicolor panel of novel lentiviral "gene ontology" (LeGO) vectors for functional gene analysis. Mol Ther. 2008;16(4):698-706. doi: 10.1038/mt.2008.6. PubMed PMID: 18362927.
45. Adler H, Messerle M, Wagner M, Koszinowski UH. Cloning and mutagenesis of the murine gammaherpesvirus 68 genome as an infectious bacterial artificial chromosome. J Virol. 2000;74(15):6964-74. Epub 2000/07/11. PubMed PMID: 10888635; PubMed Central PMCID: PMC112213.
46. Brulois KF, Chang H, Lee AS, Ensser A, Wong LY, Toth Z, et al. Construction and manipulation of a new Kaposi's sarcoma-associated herpesvirus bacterial artificial chromosome clone. J Virol. 2012;86(18):9708-20. doi: 10.1128/JVI.01019-12. PubMed PMID: 22740391; PubMed Central PMCID: PMCPMC3446615.
47. Tischer BK, Smith GA, Osterrieder N. En passant mutagenesis: a two step markerless red recombination system. Methods Mol Biol. 2010;634:421-30. doi: 10.1007/978-1-60761-652-8_30. PubMed PMID: 20677001.
48. Myoung J, Ganem D. Generation of a doxycycline-inducible KSHV producer cell line of endothelial origin: maintenance of tight latency with efficient reactivation upon induction. J Virol Methods. 2011;174(1-2):12-21. doi: 10.1016/j.jviromet.2011.03.012. PubMed PMID: 21419799; PubMed Central PMCID: PMCPMC3095772.
49. Paden CR, Forrest JC, Tibbetts SA, Speck SH. Unbiased mutagenesis of MHV68 LANA reveals a DNA-binding domain required for LANA function in vitro and in vivo. PLoS Pathog. 2012;8(9):e1002906. doi: 10.1371/journal.ppat.1002906. PubMed PMID: 22969427; PubMed Central PMCID: PMCPMC3435236.
50. Skene PJ, Henikoff S. A simple method for generating high-resolution maps of genome-wide protein binding. Elife. 2015;4:e09225. doi: 10.7554/eLife.09225. PubMed PMID: 26079792; PubMed Central PMCID: PMCPMC4480131.
51. Langmead B, Trapnell C, Pop M, Salzberg SL. Ultrafast and memory-efficient alignment of short DNA sequences to the human genome. Genome Biol. 2009;10(3):R25. Epub 2009/03/06. doi: 10.1186/gb-2009-10-3-r25. PubMed PMID: 19261174; PubMed Central PMCID: PMC2690996.
52. Thorvaldsdottir H, Robinson JT, Mesirov JP. Integrative Genomics Viewer (IGV): high-performance genomics data visualization and exploration. Brief Bioinform. 2013;14(2):178-92. Epub 2012/04/21. doi: 10.1093/bib/bbs017. PubMed PMID: 22517427; PubMed Central PMCID: PMC3603213.
53. Lerdrup M, Johansen JV, Agrawal-Singh S, Hansen K. An interactive environment for agile analysis and visualization of ChIP-sequencing data. Nat Struct Mol Biol. 2016;23(4):349-57. doi: 10.1038/nsmb.3180. PubMed PMID: 26926434.
54. Stovner EB, Saetrom P. epic2 efficiently finds diffuse domains in ChIP-seq data. Bioinformatics. 2019. doi: 10.1093/bioinformatics/btz232. PubMed PMID: 30923821.
55. Dobin A, Davis CA, Schlesinger F, Drenkow J, Zaleski C, Jha S, et al. STAR: ultrafast universal RNA-seq aligner. Bioinformatics. 2013;29(1):15-21. doi: 10.1093/bioinformatics/bts635. PubMed PMID: 23104886; PubMed Central PMCID: PMCPMC3530905.
56. Liao Y, Smyth GK, Shi W. featureCounts: an efficient general purpose program for assigning sequence reads to genomic features. Bioinformatics. 2014;30(7):923-30. doi: 10.1093/bioinformatics/btt656. PubMed PMID: 24227677.
57. Cheng BY, Zhi J, Santana A, Khan S, Salinas E, Forrest JC, et al. Tiled microarray identification of novel viral transcript structures and distinct transcriptional profiles during two modes of productive murine gammaherpesvirus 68 infection. J Virol. 2012;86(8):4340-57. Epub 2012/02/10. doi: 10.1128/JVI.05892-11. PubMed PMID: 22318145; PubMed Central PMCID: PMC3318610.

bioRxiv preprint first posted online May. 15, 2019; doi: http://dx.doi.org/10.1101/639898. The copyright holder for this preprint (which was not peer-reviewed) is the author/funder, who has granted bioRxiv a license to display the preprint in perpetuity. It is made available under a CC-BY 4.0 International license.

Supporting Information

S1 Fig. ChIP-seq coverage across the MHV-68 genome in S11E cells or the MHV-68Δ50 BAC cassette in MLE12 cells.

Shown are coverage data from ChIP-seq experiments performed with the the indicated antibodies for (A) the MHV-68 genome in S11E cells or (B) the bacmid backbone at the leftmost end of the genome in MHV-68Δ50 BAC-infected MLE12 cells. For the latter, ChIP-seq data from the same samples shown in Figure 3B were mapped to the MHV-68 reference genome including the sequence of the BAC-cassette. For further details please refer to the legends of Figs 1 and 3.

S2 Fig. RNA-seq analysis of MHV-68 infected S11E and MLE12 cells.

(A) RNA-seq analysis of persistently infected S11E cells (upper panel) or *de novo* MHV-68 infected MLE12 cells at 12, 24 and 48 hours post infection (lower panels). (B) RNA-seq analysis of two independent GFP-sorted MLE12 cell cultures which had been infected with MHV-68Δ50 for more than 3 weeks. (C) RNA-seq analysis of two splenocyte pools isolated from MHV-68-H2BYFP infected mice (3 mice per pool) at 17 days post infection. RNA sequencing for A and B was performed using a strand-specific sequencing protocol, for C a non-strand-specific, ultra-low input kit was used. Paired-end RNA-seq reads and single reads (for the low cell RNA-seq) were mapped to the MHV-68 reference sequence (NC_001826) using the splice-sensitive STAR pipeline (see Material and Methods for details). Coverage tracks depict mean coverage across 100 bp binning windows. For strand-specific data in A and B, forward and reverse strand coverage is shown in the upper and lower plots of each panel. Plots in C show coverage across both strands.

(D) Heatmaps and hierarchal clustering (see tree at top) of normalized feature counts across individual MHV-68 ORFs annotated in the NC_001826 GenBank entry for the experiments shown in A, B and C.

bioRxiv preprint first posted online May. 15, 2019; doi: http://dx.doi.org/10.1101/639898. The copyright holder for this preprint (which was not peer-reviewed) is the author/funder, who has granted bioRxiv a license to display the preprint in perpetuity. It is made available under a CC-BY 4.0 International license.

S3 Fig. H3K4-me3 is enriched at putative mRNA start sites of immediate-early genes.

(A) Black and dark grey arrows depict the predicted coding transcripts located downstream of an H3K4-me3 peak (as observed in MHV-68Δ50 infected MLE-12 cells) within a maximum distance of 250bp of their TSS. Transcripts downstream of peaks that are detected at 5 dpi but not in long-term infection are shown in gray. Tracks above transcripts reproduce the H3K4-me3 coverage from Fig 3 (top and bottom track correspond to data from 5 days p.i. or long term infected cultures, respectively) as a heat map, including the location of peaks detected by MACS14 (indicated by black bars underneath the tracks). (B, C) For each of the 4 expression kinetics clusters (I-IV) defined by Cheng and colleagues [57] for de novo infected fibroblasts (left graphs in each panel) or reactivated B-cells (right graphs) we calculated the percentage of ORFs encoded by transcripts located downstream of H3K4-me3 peaks observed after (B) 5 days of infection or in (C) long-term infected MLE-12 cells (dark grey columns in each graph). Light grey columns and associated error bars represent mean values and standard deviations of analyses repeated 100,000 times with randomly shuffled peaks. Cases with significant (<=0.05) p-values for the hypothesis that the number of ORFs observed with authentic peaks was significantly above that expected by chance (see S1 Protocol for further details) are indicated.

S4 Fig. Immgen GeneSet analysis of 200 highly expressed genes in sorted infected B-cells.

Immgen GeneSet analysis (http://www.immgen.org) of the top 200 expressed genes (as judged by STAR transcriptome analysis) from ultra-low input RNA-seq data of 1000 pooled splenocytes isolated from mice infected with MHV-68-H2BYFP 17 days post infection (see results and material & methods sections for details). The heatmap indicates the RNA-seq based row mean normalized expression values of the respective gene ID list for all immune cells within the Immgen database. Germinal center B-cells are indicated with an arrow.

bioRxiv preprint first posted online May. 15, 2019; doi: http://dx.doi.org/10.1101/639898. The copyright holder for this preprint (which was not peer-reviewed) is the author/funder, who has granted bioRxiv a license to display the preprint in perpetuity. It is made available under a CC-BY 4.0 International license.

S5 Fig. Analysis of CpG frequency/suppression and CpG island prediction in the genomes of KSHV and MHV-68.

Graphs show GC content (black dashed line, right y-axis) and CpG supression index (red solid line, left y-axis) in a window of 500bp shifted in 250bp steps across the RefSeq genome sequences of (A) KSHV (GenBank accession NC_009333) or (B) MHV-68 (GenBank accession NC_001826). Overall CpG supression index and GC-content is indicated above the graph in each panel. The distribution of CpG motifs is shown in a map underneath the graphs, where the position of each individual motif is indicated by a vertical light-red line. The total number of CpG motifs is given to the right of the map. Blue bars below the CpG map indicate regions which register as CpG islands when employing the same criteria commonly used to designate host cell CpG islands (length >= 200bp, GC-content >= 50%, CpG suppression index >= 0.6). CpG islands were predicted by shifting a 200bp window in steps of 100bp across the viral genomes. Adjacent positive windows were then iteratively joined as long as the qualification criteria were satisfied by the merged region. The overall percentage of the viral genome that qualifies as a CpG Island is given to the right.

S6 Fig. KSHV genomes acquire early H2AK199-ub marks upon infection of SLK cells

ChIP-seq coverage across the KSHV genome for (top) H2AK119-ub, (2nd from top) H3K27-m3, (2nd from bottom) or(bottom in each panel) input in SLK cells 24 hours (A) or 5 days (B) after infection with KSHV.

S7 Fig. Statistical analysis of ChIP-seq data in de novo KSHV-infected SLK cells and MHV-68Δ50 infected MLE-12 cells

Enrichment of H2AK119-ub, H3K27-me3 and H3K36-me2 was analyzed using the statistical method described in the legend to Figure 4 and the materials and methods section. Data from MLE12 and SLKp

bioRxiv preprint first posted online May. 15, 2019; doi: http://dx.doi.org/10.1101/639898. The copyright holder for this preprint (which was not peer-reviewed) is the author/funder, who has granted bioRxiv a license to display the preprint in perpetuity. It is made available under a CC-BY 4.0 International license.

cells correspond to those shown in Figs 9E and F for H2AK119-ub and H3K36-me2, or those in Fig 4 for H3K27-me3. Coverage tracks for SLK cells at 24 h.p.i and 5 d.p.i. are provided in S6 Fig.

S8 Fig. Analysis of CpG methylation by MeDIP-seq in long-term MHV-68Δ50-infected cells.

DNA methylation levels were detected by MeDIP-seq using highly pure genomic DNA extracted from long-term MHV-68Δ50-infected MLE12 cells. We generated a positive control sample by in vitro methylation of MHV-68-BAC DNA that was spiked into genomic DNA from MLE12 cells to reflect authentic episome copy numbers in infected cells, as estimated by qPCR. Likewise, we used MLE12 DNA supplemented with unmethylated MHV-68-BAC DNA as negative control. Read coverage was normalized by total mapped read counts and viral input DNA to generate directly comparable tracks. (A) Episome-wide MeDIP-seq analysis. The three lower heat map tracks (in red) indicate relative MeDIP-seq coverage (normalized to the positive control) in the individual samples. The upper track (in green) reproduces the H3K4-me3 coverage data from Fig 3B. Boxes at the top of the panel indicate H3K4-me3 peaks detected by MACS in MHV-68Δ50-infected MLE12 cells. Filled boxes represent stable peaks which persist in long-term infected cells, whereas open boxes indicate transient peaks which are only observed at 5 days post infection. The peak positions are furthermore indicated by dashed frames overlaying the heat map panels. Hashed boxes in the genome map at the bottom indicate repetitive regions unsuitable for analysis and the dotted box marks the ORF50 deletion. (B) Quantification of relative DNA methylation levels (in percent of the positive control) from A in regions which do not acquire any H3K4-me3 peaks (none), or in stable or transient peaks (see legend to panel A for further information). Only persistent peaks protect viral DNA from methylation in long-term infected cells. Data are presented as mean ± SEM. (C) Detailed view of the ORF50 promoter region. The proximal and distal ORF50 promoters are marked by rectangles. The dotted box marks the deletion in the ORF50 coding region.

bioRxiv preprint first posted online May. 15, 2019; doi: http://dx.doi.org/10.1101/639898. The copyright holder for this preprint (which was not peer-reviewed) is the author/funder, who has granted bioRxiv a license to display the preprint in perpetuity. It is made available under a CC-BY 4.0 International license.

S1 Dataset. ChIP-seq, RNA-seq and MeDIP-seq coverage tracks.

This dataset contains all sequencing coverage tracks of MHV-68 and KSHV as presented in Figs 1, 2, 3, 5, 6, 7, 8, 9, S1, S2, and S6.

S2 Dataset. Correlation coefficients.

Correlation coefficients of all analyzed ChIP-seq data (S1 Dataset) were calculated using Graph Pad Prism.

S3 Dataset. FeatureCounts data.

This dataset contains raw and normalized results of STAR/FeatureCounts analysis of RNA-seq data. This data is presented in Fig 2C.

S4 Dataset. H3K4-me3 peak data as detected by MACS14.

S5 Dataset. MHV-68 polyA-sites, splice-junctions, predicted primary transcripts / processed transcripts.

This dataset provides all polyA-sites as well as splice junctions and frequencies observed in our RNA-seq analyses, along with a prediction of primary and processed transcripts. For the latter, the dataset further provides coding potential and proximity to H3K4-me3 peaks, as well as an estimate of relative abundance values in individual samples.

S1 Protocol. Bioinformatic analysis of MHV-68 transcription units and correlation with activation-associated histone marks.

S2 Protocol. MeDIP-seq protocol.

bioRxiv preprint first posted online May. 15, 2019; doi: http://dx.doi.org/10.1101/639898. The copyright holder for this preprint (which was not peer-reviewed) is the author/funder, who has granted bioRxiv a license to display the preprint in perpetuity. It is made available under a CC-BY 4.0 International license.

Figure Legends

Fig. 1: ChIP-seq analysis of MHV-68 and KSHV epigenomes in tumor-derived B-cell lines.

ChiP-seq coverage for H3K4-me3 and H3K27-me3, or corresponding input coverage across the KSHV genome in BCBL1 (A) or the MHV-68 genome in S11E cells (B) for the indicated antibodies. Regions on the MHV-68 genome enriched for H3K4-me3 as detected using MACS14 are indicated by black bars. Asterisks indicate likely false positives also present in the IgG control (S1A Fig). Hashed boxes indicate repetitive regions (including the terminal repeats) that were excluded from the analysis as they do not allow unique read mapping.

Fig. 2: RNA-seq analysis of S11E and de novo infected MLE12 cells.

(A) RNA-seq analysis of persistently infected S11E cells (upper panel), *de novo* MHV-68 infected MLE12 cells at 12 hours post infection (center panel) or GFP-sorted MLE12 cells which had been infected with MHV-68Δ50 for more than 3 weeks (lower panel). RNA sequencing was performed using a strand-specific sequencing protocol and resulting paired-end RNA-seq reads were mapped to the MHV-68 reference sequence (NC_001826) using the splice-sensitive STAR pipeline (see Material and Methods for details). Coverage tracks depict mean coverage across 100 bp binning windows. Forward and reverse strand coverage is shown in the upper and lower plots of each panel.

(B) Heatmaps depicting normalized read coverage across individual MHV-68 ORFs annotated in the NC_001826 GenBank entry for the experiments shown in A.

Fig. 3: ChIP-seq analysis of KSHV and MHV-68Δ50 epigenomes in SLKp or MLE12 cells.

ChIP-seq results from (A) KSHV infected SLK_P cells or (B) long-term MHV-68Δ50 infected MLE12 cells and (C) MLE12 cells at day 5 post infection with MHV-68Δ50. Solid bars underneath H3K4-me3 plots indicate peak regions as detected by MACS14. Regions that were uniquely enriched at either day five or in long-term latency are marked with an asterisk (*) in each panel. Hashed boxes above the MHV-

bioRxiv preprint first posted online May. 15, 2019; doi: http://dx.doi.org/10.1101/639898. The copyright holder for this preprint (which was not peer-reviewed) is the author/funder, who has granted bioRxiv a license to display the preprint in perpetuity. It is made available under a CC-BY 4.0 International license.

68 and KSHV genomes map indicate repetitive regions excluded from the analysis, and the dotted box above MHV-68 indicates the deletion of ORF50 coding sequences in MHV-68Δ50.

Fig. 4: Statistical analysis of H3K27-me3 levels acquired by viral episomes.

Shown is an analysis of two biological replicates collected from MHV-68Δ50-infected MLE12 cells (left panels) or KSHV-infected SLKp cells (right panels) each. The graphs depict average enrichment of H3K27-me3 levels in positive and negative control regions of the host genomes, relative to average enrichment across the viral genome. H3K27-me3 positive (host pos) and negative (host neg) host regions (200 each) were detected by SICER/EPIC2, and enrichment across viral sequences was calculated using a 10kb sliding window (see methods section for details). For each region we individually calculated the H3K27-me3 to input read count ratio and normalized all groups to the average of the respective negative control. Data are shown as box-whisker-plots with 5th-95th percentile and median (+). Significance was calculated by 1way ANOVA testing (MLE-12: $F = 64.36$, $df = 817$; SLK_P: $F = 341$, $df = 770$). Significance is indicated by asterisks or ns (not significant).

Fig. 5: ChIP-seq analysis of KSHV and MHV-68Δ50 epigenomes in superinfected MLE12 cells.

(A) H3K4-me3 and H3K27 ChIP-seq coverage across MHV-68Δ50 (top) and KSHV (bottom) genomes in long-term MHV-68Δ50-infected MLE12 cells superinfected with KSHV for five days. Read counts in all samples were normalized to input DNA to correct for differences among KSHV and MHV-68Δ50 episome copy numbers per cell. (B) Statistical analysis of H3K27-me3 enrichment in two replicates of MHV-68Δ50-positive MLE12 cells superinfected with KSHV. Analysis was performed analogous to that shown in Fig 4. Data are shown as box-whisker-plots with 5th-95th percentile and median (+). Significance was calculated by 1way ANOVA testing ($F = 270.8$, $df = 889$). Significance is indicated by asterisks or ns (not significant). (C) Confirmatory ChIP-qPCR using KSHV-, MHV-68- and mouse-specific primers as indicated (n=3). Positive controls were as follows: H3K4-me3: GAPDH, RPL30; H3K27-me3:MYT1; H3K4-me3/H3K27-me3 (bivalent chromatin): PITX1. Data are represented as mean ± SEM.

bioRxiv preprint first posted online May. 15, 2019; doi: http://dx.doi.org/10.1101/639898. The copyright holder for this preprint (which was not peer-reviewed) is the author/funder, who has granted bioRxiv a license to display the preprint in perpetuity. It is made available under a CC-BY 4.0 International license.

Fig. 6: kLANA-expressing MHV-68Δ50 genomes do not gain the ability to rapidly recruit H3K27-me3 marks

(A) H3K27-me3 ChIP-seq coverage across the MHV-68Δ50 genome in MLE12 cells sorted for GFP expression at day 5 post infection with MHV-68Δ50-kLANA (top) or MHV-68Δ50 (bottom). Due to the low titers of the MHV-68Δ50-kLANA virus, ChIP-seq was performed for both cultures using a low-cell ChIP protocol as described in the material and methods section.

(B) Relative H3K27-me3 enrichment analysis for the data shown in panel A, performed as described in the legend to Fig 4. Significance was calculated by 1way ANOVA testing (F = 640.7, df = 781) and is indicated by asterisks or ns (not significant).

(C) Confirmatory ChIP-qPCR analysis of MHV-68Δ50-kLANA or MHV-68Δ50-infected MLE12 cells at 5 days post infection (n=1, top panel), or after a 35 day period during which cells were repeatedly sorted to achieve a population of 100% GPF positive cells (n=2, bottom panel). Data are represented as mean ± SEM.(D) Western blot analysis of mLANA and kLANA expression in cells infected with MHV-68Δ50-kLANA or MHV-68Δ50, respectively. Unspecific bands are indicated by asterisks.

Fig. 7: KSHV-BAC16Δ73 genomes trans-complemented by mLANA do not lose the ability to rapidly recruit H3K27-me3 marks

(A) ChIP-qPCR analysis of H3K4-me3 and H3K27-me3 in KSHV-BAC16Δ73-infected MLE12 cells that had been stably transduced with lentiviral mLANA or kLANA expression constructs. Cells were cultured in the presence of hygromycin to enrich for KSHV-BAC16Δ73-infected cells and ChIP was performed at day 5 (n>=2, top panel) or day 33 post infection (n>=2, bottom panel). Data are represented as mean ± SEM.

(B) H3K27-me3 and H3K4-me3 ChIP-Seq analysis of material harvested after 33 days from KSHV-BAC16Δ73-infected kLANA (top panels) or mLANA (bottom panels)-expressing MLE12 cultures. Lower input coverage across the left half of the KSHV genome in MLE12-mLANA cells (see bottom panel)

bioRxiv preprint first posted online May. 15, 2019; doi: http://dx.doi.org/10.1101/639898. The copyright holder for this preprint (which was not peer-reviewed) is the author/funder, who has granted bioRxiv a license to display the preprint in perpetuity. It is made available under a CC-BY 4.0 International license.

suggests loss of sub-genomic material from a fraction of episomes, similar to what has recently been observed with KSHV mutants expressing an oligomerization-deficient kLANA protein [25]. For visualization purposes ChIP-seq tracks were therefore normalized for using mean input coverage values. Non-normalized coverage data as used for statistical analysis is given in S1 Dataset.

(C) Statistical analysis of H3K27-me3 enrichment on BAC16Δ73 episomes calculated as described in the legend to figure 4. Significance was calculated by 1way ANOVA testing (F = 431.2, df = 838). The difference between BAC16ΔLANA in kLANA vs. mLANA expressing cells was not significant (ns).

(D) Western blot analysis of mLANA and kLANA expression in stably transduced MLE12 cells.

Fig. 8: Histone-modification patterns of latent MHV-68 genomes *in vivo*.

(A) ChIP-qPCR analysis of H3K27-me3 (top), H3K4-me3 (center) or IgG (negative control, bottom) in splenocytes harvest from two mice (#1 and #2) that had been intranasally infected with wildtype MHV-68 for 17 days, using MHV-68 or endogenous control primers as indicated. Data are represented as mean ± SEM of three independent ChIP replicates performed with the isolated chromatin from each mouse.

(B) H3K27-me3 ChIP-seq coverage across the MHV-68 genome in two pools of splenocytes isolated from a total of six mice that had been intranasally infected with MHV-68-H2BYFP for 17 days. Splenocytes were FACS sorted for YFP expression prior to analysis. Due do the low number of positive cells, YFP-positive cells from three mice were pooled to generate pools #1 and #2. Approximately 5000 cells were subjected to low cell ChIP-seq using an H3K27-me3 specific antibody. Hashed boxes above the MHV-68 map indicate the position of repetitive regions (left and right internal repeat regions, as well as terminal repeat sequences) which had to be masked since they do not allow unique read mapping.

(C) Relative enrichment of H3K27-me3 at viral episomes in splenocyte pools #1 and #2 was assessed using the same statistical method as described in the legend to Figure 4.

bioRxiv preprint first posted online May. 15, 2019; doi: http://dx.doi.org/10.1101/639898. The copyright holder for this preprint (which was not peer-reviewed) is the author/funder, who has granted bioRxiv a license to display the preprint in perpetuity. It is made available under a CC-BY 4.0 International license.

(D) Normalized mean H3K27-m3 and input coverage from all MHV-68 ChIP-seq experiments performed in our study. Quantile normalized mean values and standard deviation (colored area) of H3K27-me3 and input tracks were generated from all MHV68-specific coverage tracks as given in S1 Dataset (ChIP MHV-68).

Fig. 9: KDM2B recruitment and acquisition of PRC1-associated histone modifications by KSHV and MHV-68Δ50 genomes.

(A) KDM2B ChIP-seq coverage (top) or input (bottom) profiles across the KSHV genome in SLK cells at 24 hours post-infection.

(B) Relative enrichment of KDM2B on *de novo* infecting KSHV episomes measured at 24 hours post infection. Enrichment was quantified similar to method described in the legend to Figure 4. KDM2B enriched human positive control regions were detected by MACS peak calling. Significance was calculated by 1way ANOVA testing (F = 372.5, df = 508).

(C) Heatmap of KDM2B enrichment at transcriptional start sites (TSS) of human genes generated from KDM2B ChIP-seq data at 24 hours post infection with KSHV infection. The Y-axis represents 70,474 individual length normalized annotated transcripts (from TSS to TTS) of human genes, and the X-axis represents the 200 % surrounding of the length-normalized genes. Data was sorted according to decreasing KSM2B signal at the TSS.

(D) Global anti-correlation of cellular H3K27-me3 and H3K36-me2 patterns across the human genome. The 2D histogram shows the number of genomic 10000 bp windows with the combination of the number of reads described on the axes in SLKp cells. The colored bar to the right side illustrates the number of windows with each combination of reads in the two datasets.

(E+F) ChIP-seq coverage for H3K36-me2 (top) and H2AK119-ub (center) or input (bottom in each panel) from (E) stably KSHV-infected SLK_P cells or (F) long-term MHV-68Δ50-infected MLE12 cells.

(G) Analysis of significant enrichment of H2AK119ub, H3K27me3 and H3K36me3 on KSHV genomes in (left panel) SLK cells after 24 hours of infection, (2nd panel from left) SLK cells after 5 days of infection

bioRxiv preprint first posted online May. 15, 2019; doi: http://dx.doi.org/10.1101/639898. The copyright holder for this preprint (which was not peer-reviewed) is the author/funder, who has granted bioRxiv a license to display the preprint in perpetuity. It is made available under a CC-BY 4.0 International license.

or (2nd panel from right) SLKp cells, or (right panel) MHV68 genomes in long-term MHV68-Δ50-infected MLE12 cells. Based on the statistical method described in the legend to Figure 4, normalized enrichment was calculated relative to the median value of the host loci that showed strongest and weakest enrichment (set to 100% and 0%, respectively) for each modification. Significance indicators (asterisks) are shown for those modifications for which median enrichment along the viral genome was significantly above levels observed for the cellular background. 'nd' (not detectable) demarks modifications in which enrichment was not significantly different from (or signficantly lower) than in the negative control regions. Data from MLE12 and SLKp cells correspond to those shown in E and F above, or (for H3K27-me3) those in Fig 4. Coverage tracks for SLK cells at 24 h.p.i and 5 d.p.i. are provided in S6 Fig. Non-normalized statistical data for each of the modifications and cell lines shown in this figure are provided in S7 Fig.

Fig. 10: Model of PRC1 and -2 recruitment to KSHV and MHV-68 genomes

Immediately after nuclear entry, sequence-specific transcription factors bind to KSHV as well as MHV-68 genomes and lead to deposition of activation-associated H3K4-me3 marks. In KSHV (left panel), high density of unmethylated CpG motifs mediates rapid acquisition of the non-canonical PRC1.1 complex, followed by PRC2 recruitment as a secondary event (alternatively, PRC2 might also be directly recruited to CpG-rich DNA). Owing to the lower CpG frequency of MHV-68 genomes (right panel), only relatively short sequence segments which exhibit characteristics of CpG islands (such as the internal repeat regions) are initially acquire PRC1.1 complexes in a delayed (depicted) or stochastic manner. Once established, canonical PRC occupancy and associated histone modifications may slowly spread from these sites.

Fig 1

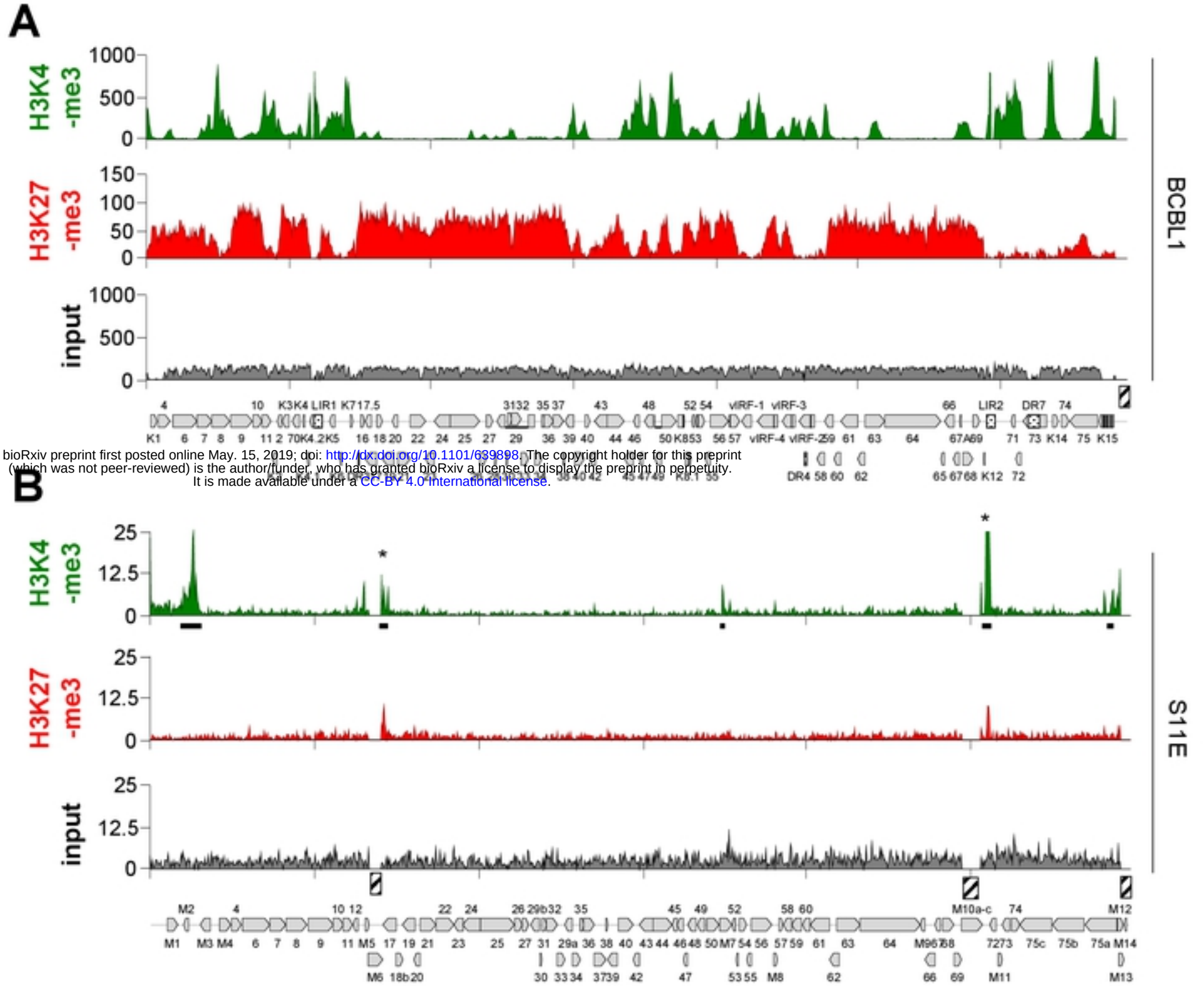

bioRxiv preprint first posted online May. 15, 2019; doi: http://dx.doi.org/10.1101/639898. The copyright holder for this preprint (which was not peer-reviewed) is the author/funder, who has granted bioRxiv a license to display the preprint in perpetuity. It is made available under a CC-BY 4.0 International license.

Fig 2

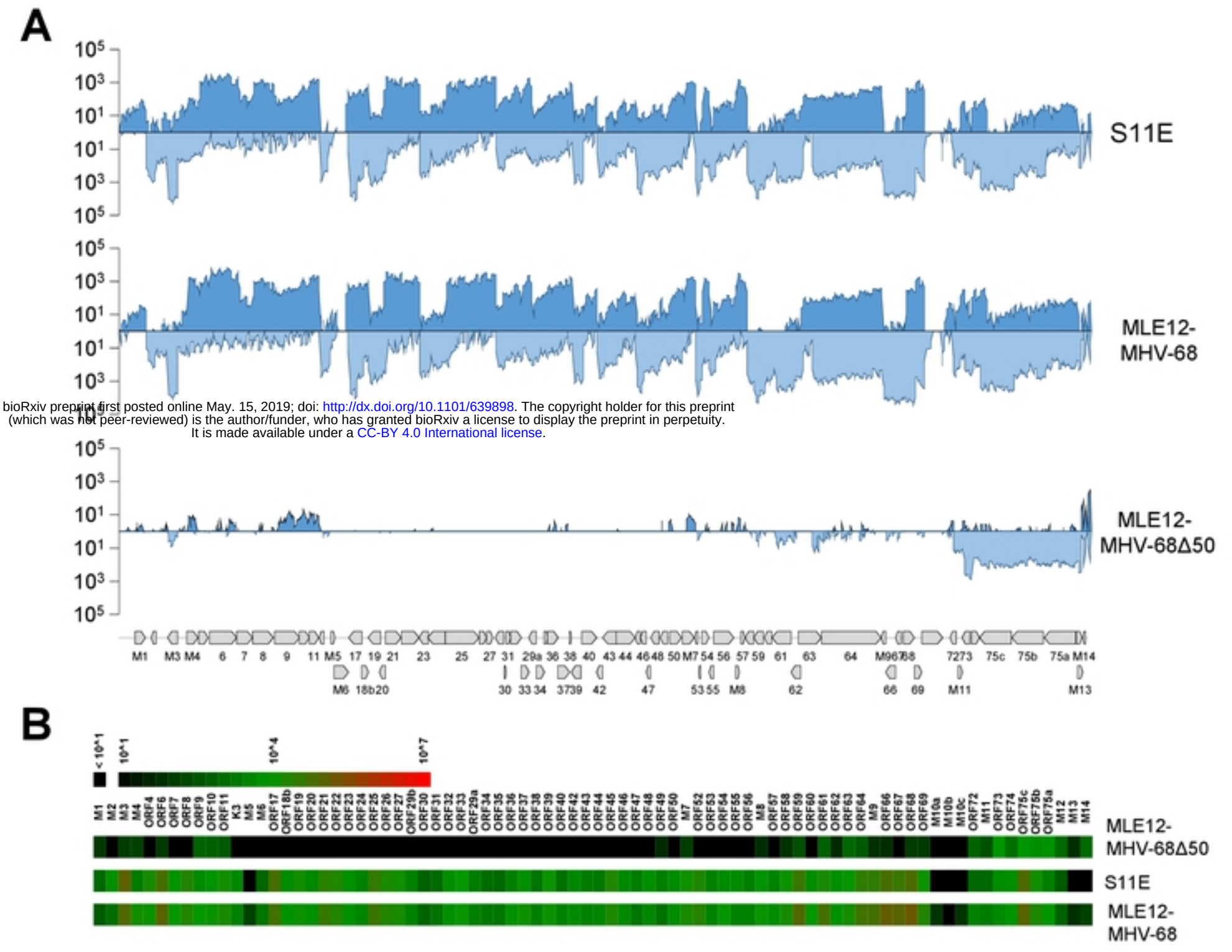

bioRxiv preprint first posted online May. 15, 2019; doi: http://dx.doi.org/10.1101/639898. The copyright holder for this preprint (which was not peer-reviewed) is the author/funder, who has granted bioRxiv a license to display the preprint in perpetuity. It is made available under a CC-BY 4.0 International license.

Fig 3

bioRxiv preprint first posted online May. 15, 2019; doi: http://dx.doi.org/10.1101/639898. The copyright holder for this preprint (which was not peer-reviewed) is the author/funder, who has granted bioRxiv a license to display the preprint in perpetuity. It is made available under a CC-BY 4.0 International license.

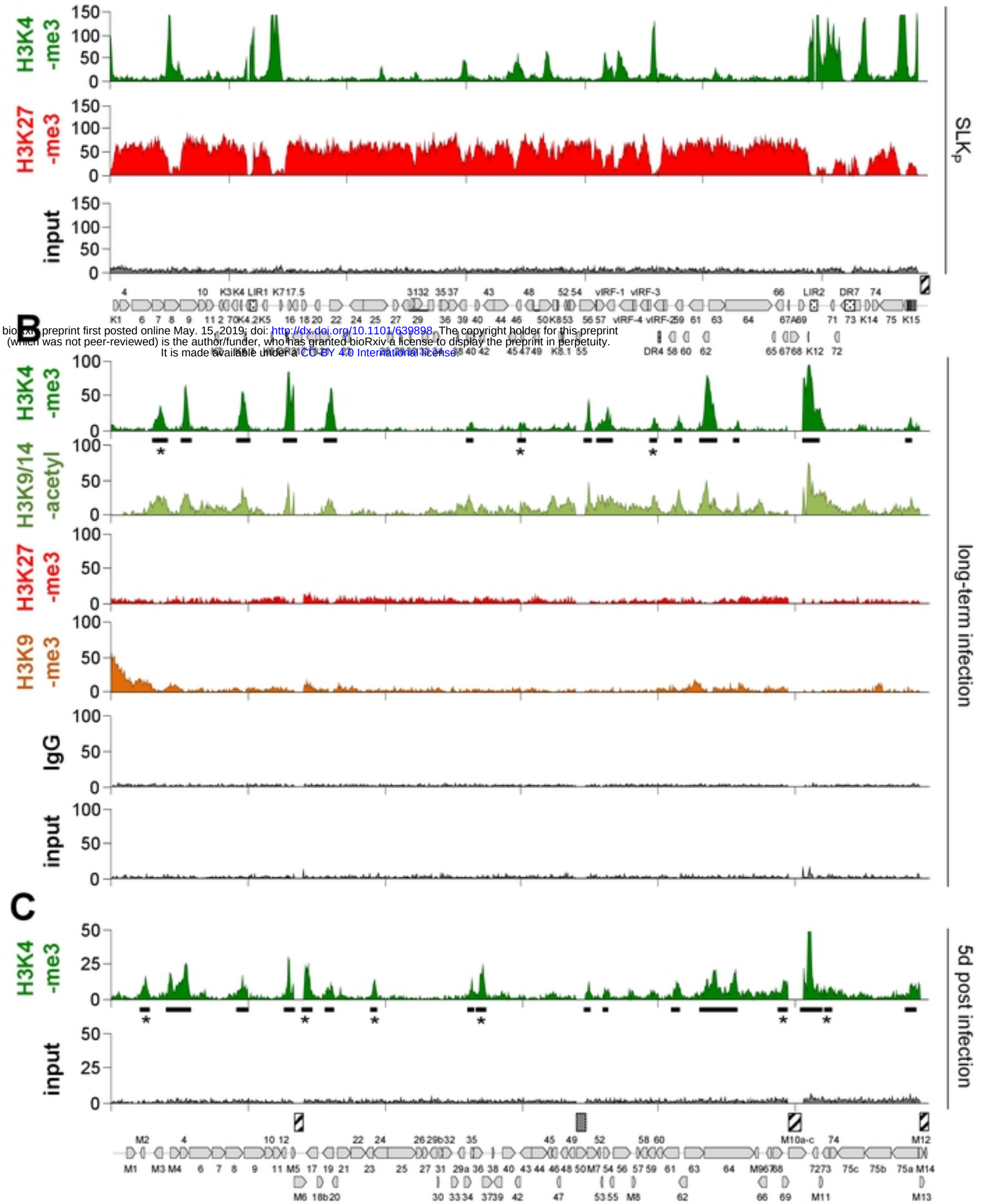

Fig 4

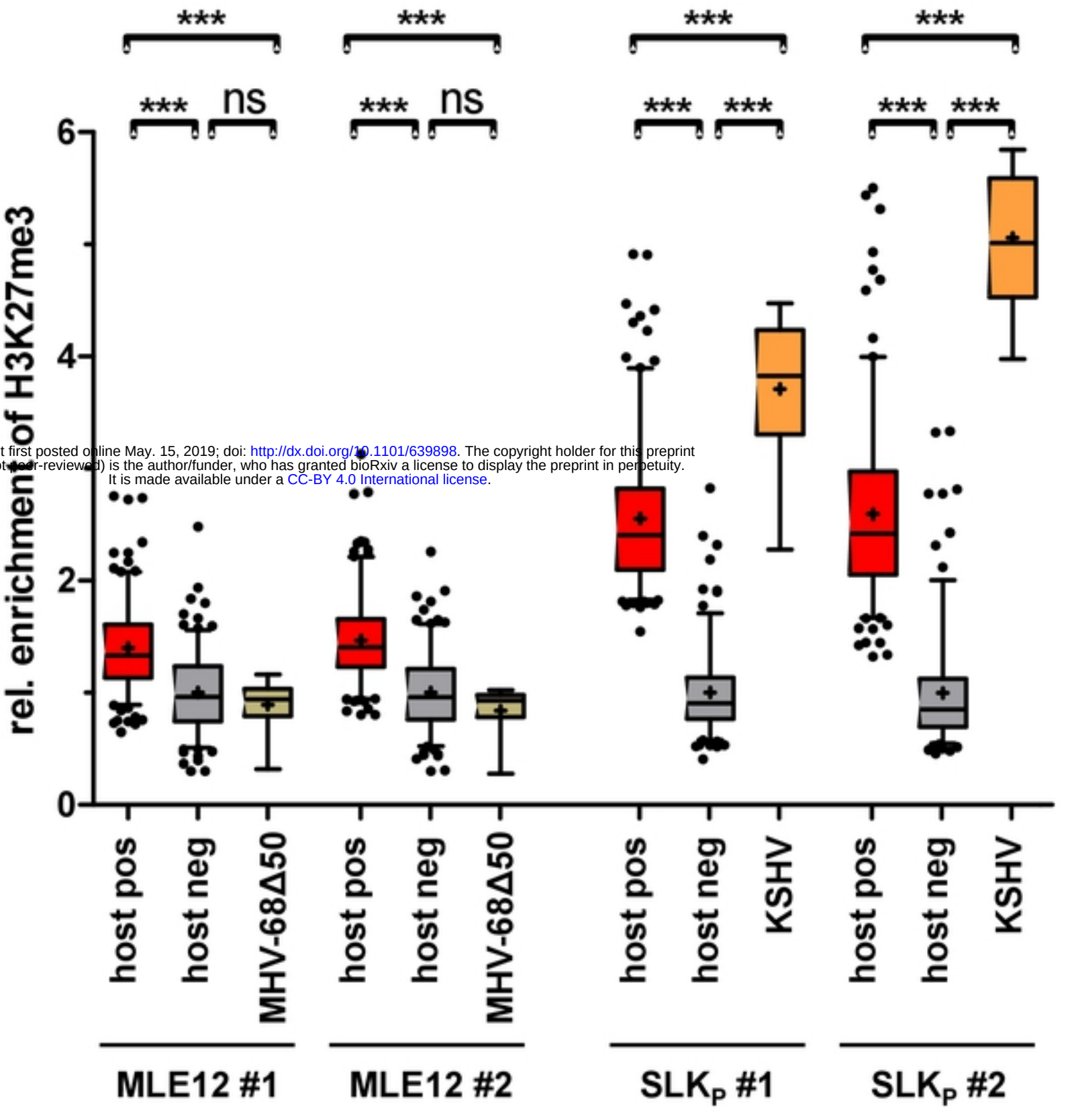

bioRxiv preprint first posted online May. 15, 2019; doi: http://dx.doi.org/10.1101/639898. The copyright holder for this preprint (which was not peer-reviewed) is the author/funder, who has granted bioRxiv a license to display the preprint in perpetuity. It is made available under a CC-BY 4.0 International license.

Fig 5

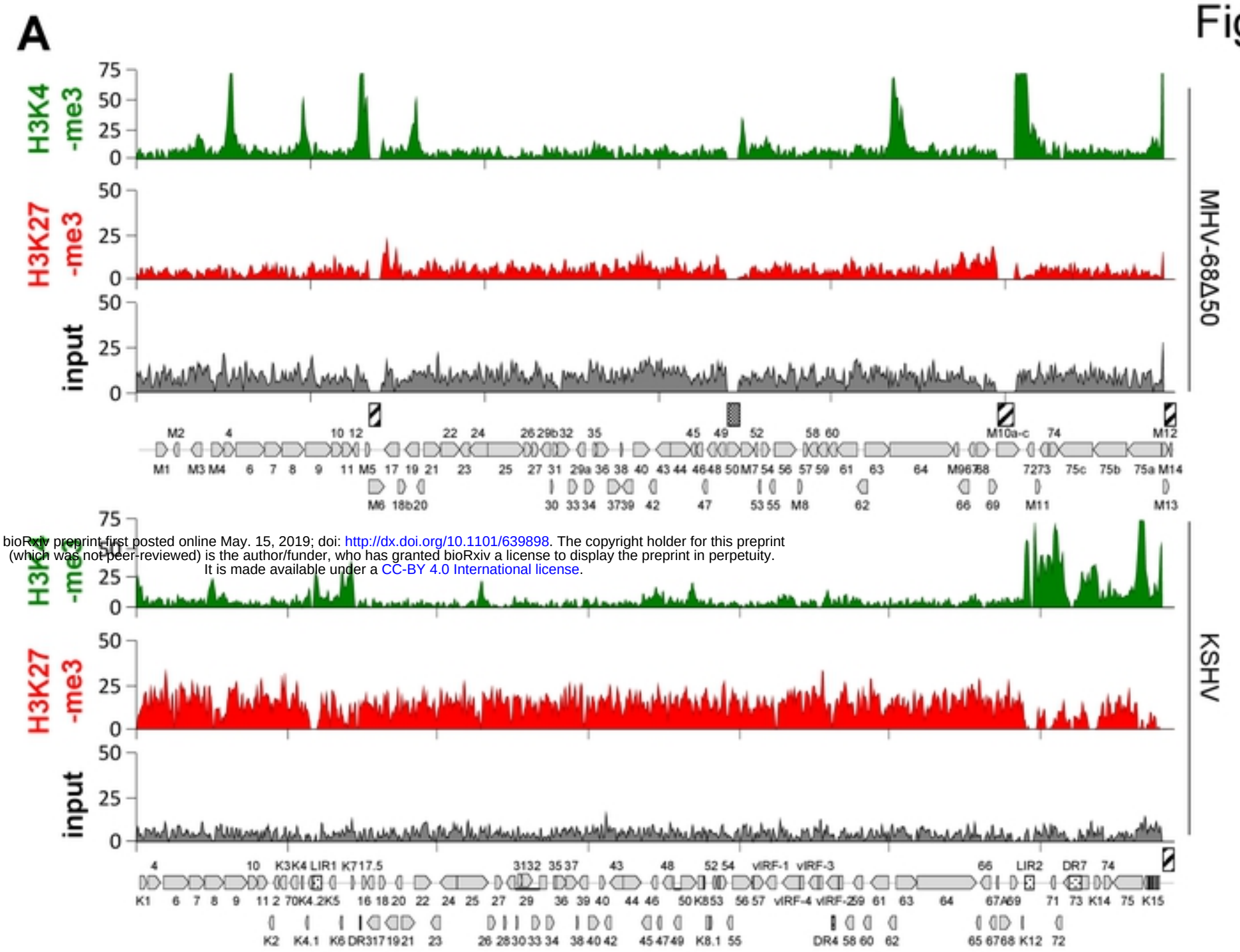

bioRxiv preprint first posted online May. 15, 2019; doi: http://dx.doi.org/10.1101/639898. The copyright holder for this preprint (which was not peer-reviewed) is the author/funder, who has granted bioRxiv a license to display the preprint in perpetuity. It is made available under a CC-BY 4.0 International license.

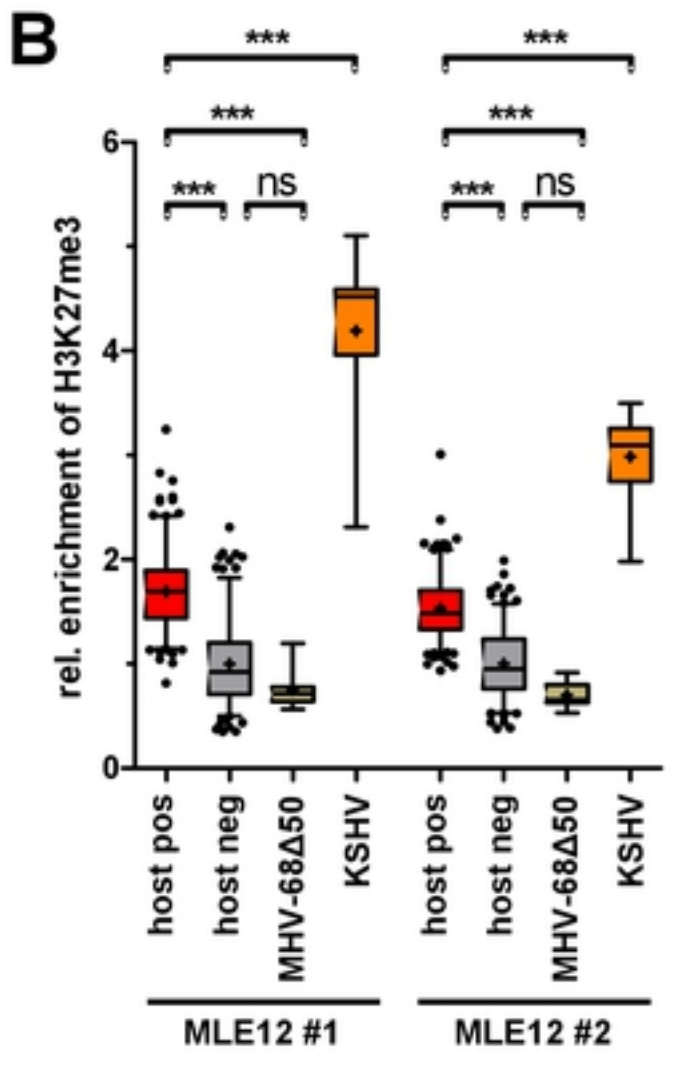

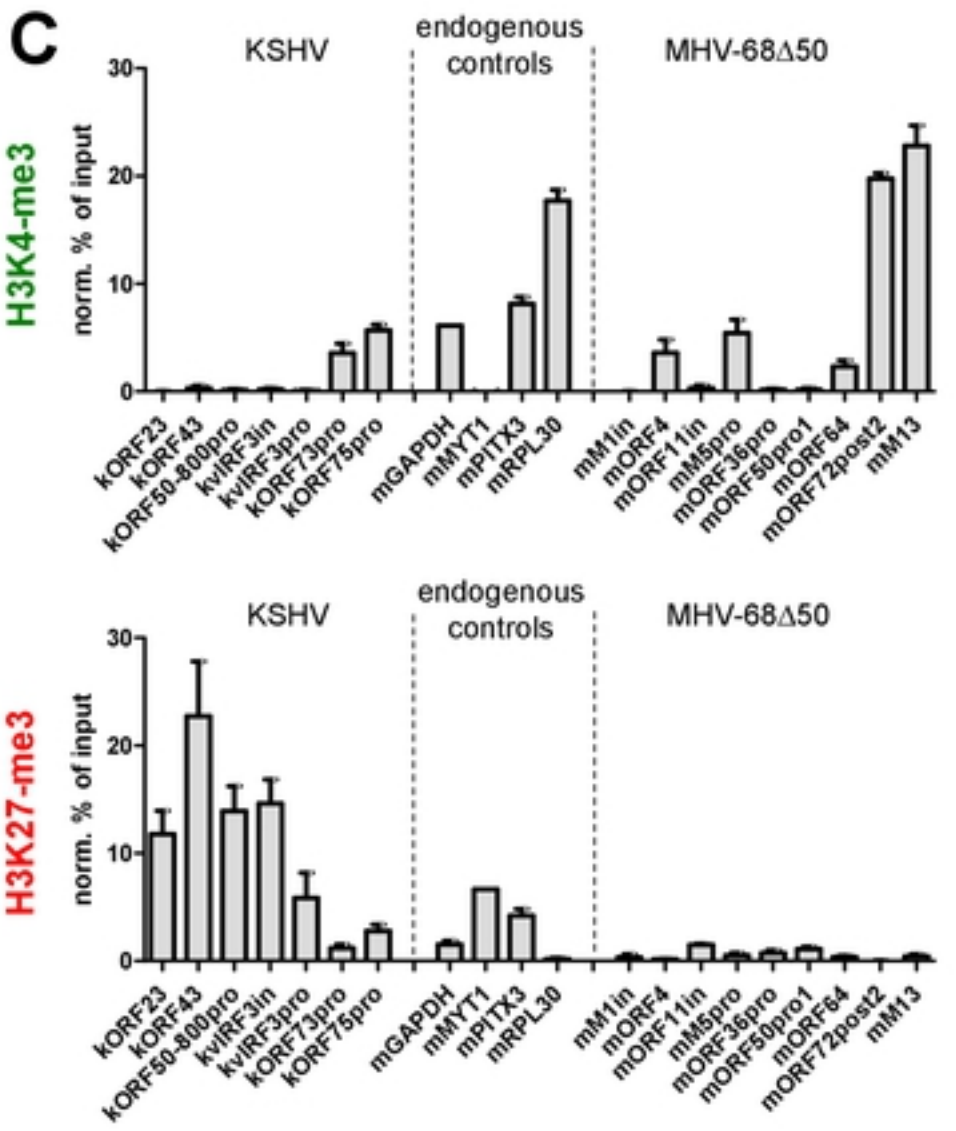

Fig 6

bioRxiv preprint first posted online May. 15, 2019; doi: http://dx.doi.org/10.1101/639898. The copyright holder for this preprint (which was not peer-reviewed) is the author/funder, who has granted bioRxiv a license to display the preprint in perpetuity. It is made available under a CC-BY 4.0 International license.

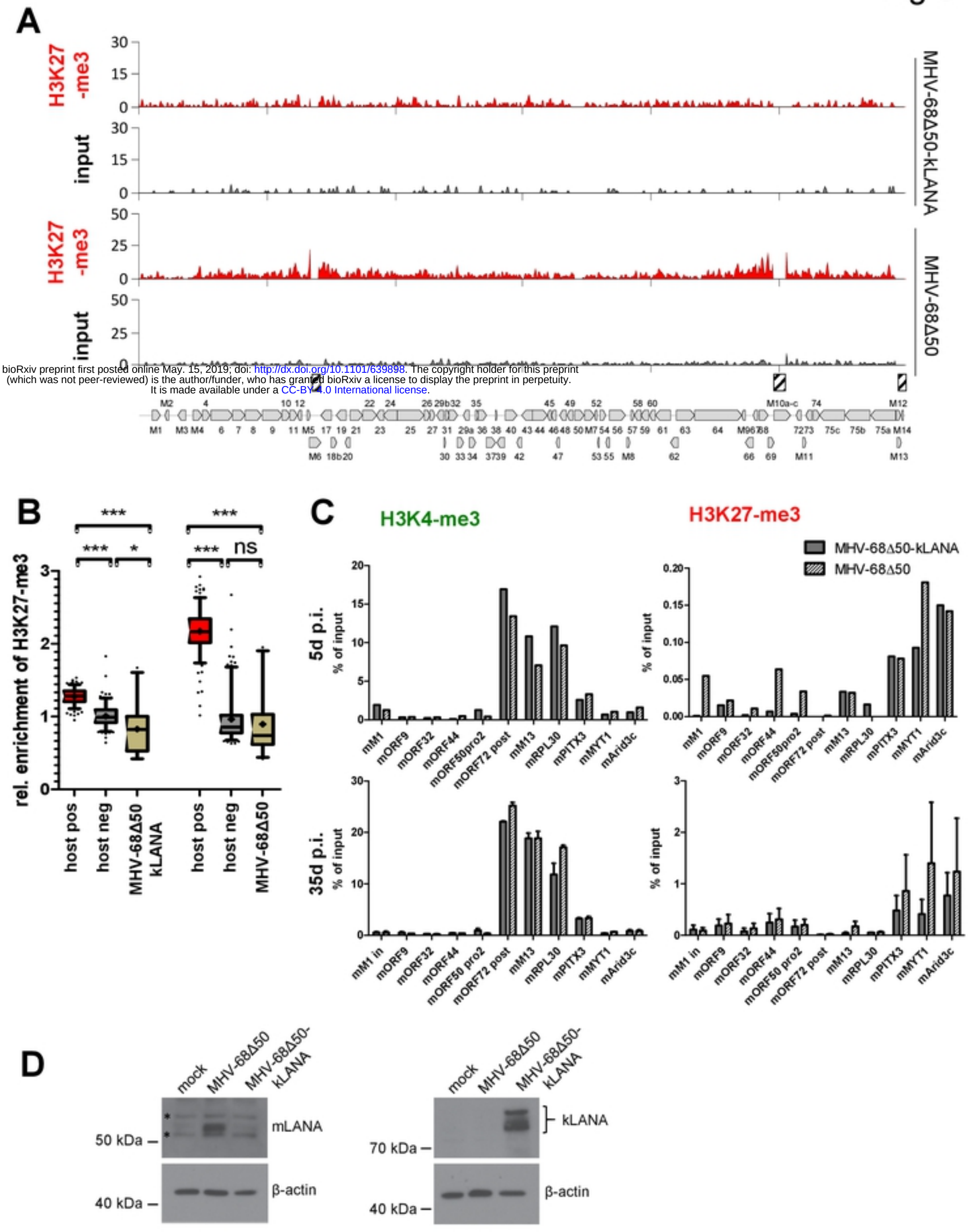

Fig 7

bioRxiv preprint first posted online May. 15, 2019; doi: http://dx.doi.org/10.1101/639898. The copyright holder for this preprint (which was not peer-reviewed) is the author/funder, who has granted bioRxiv a license to display the preprint in perpetuity. It is made available under a CC-BY 4.0 International license.

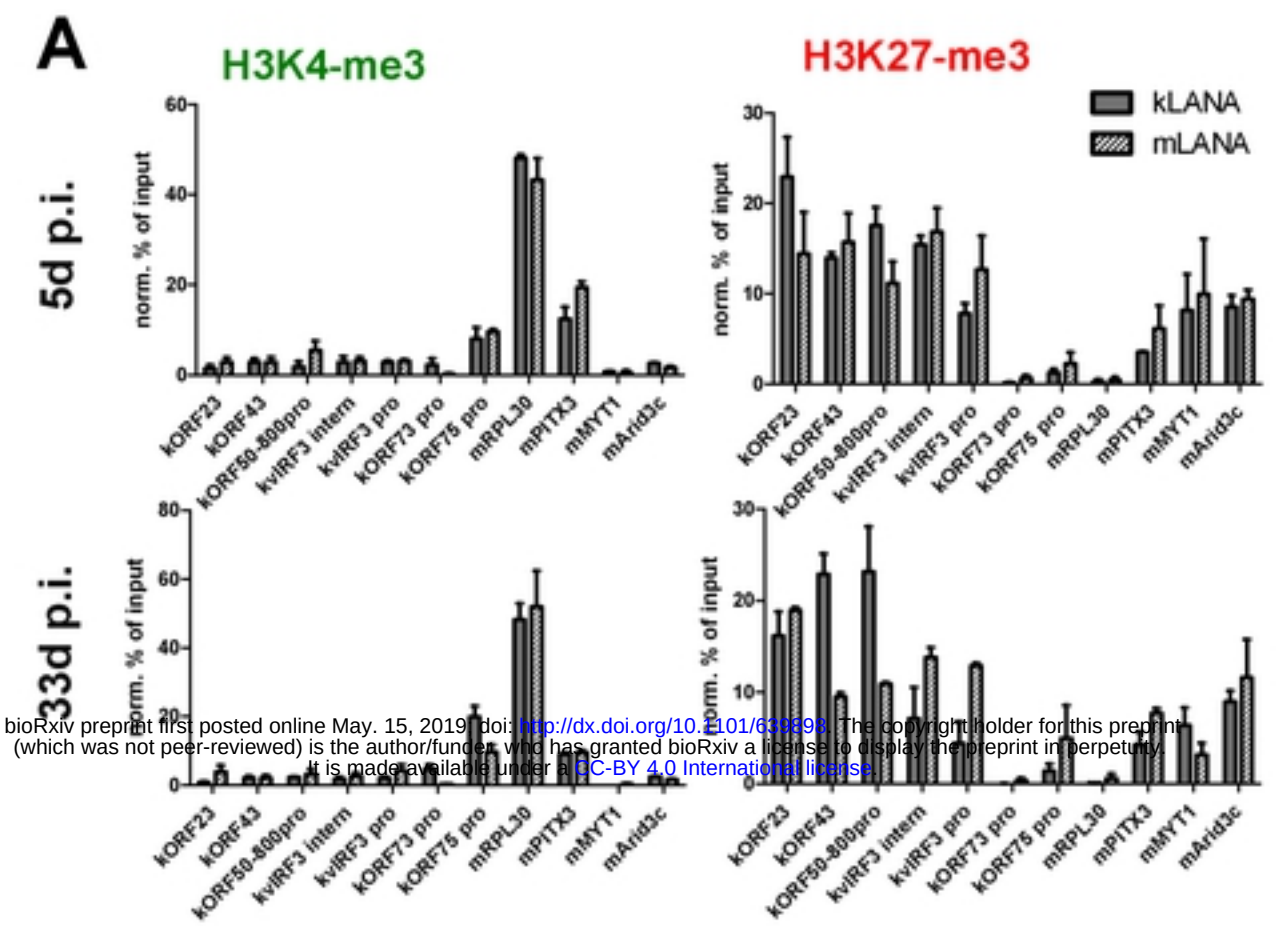

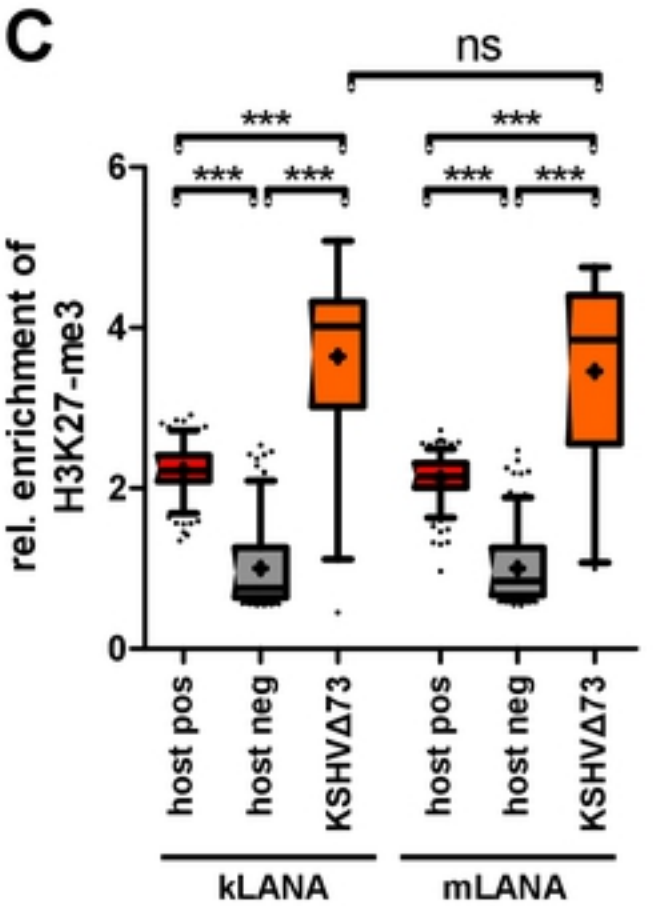

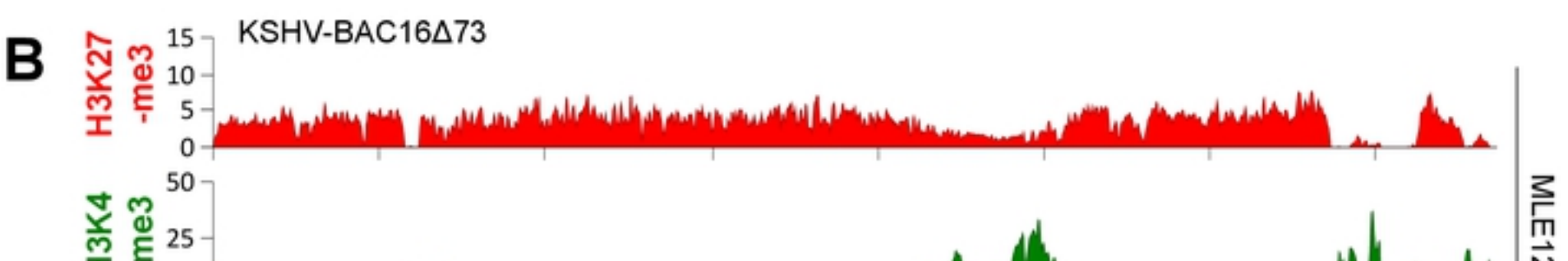

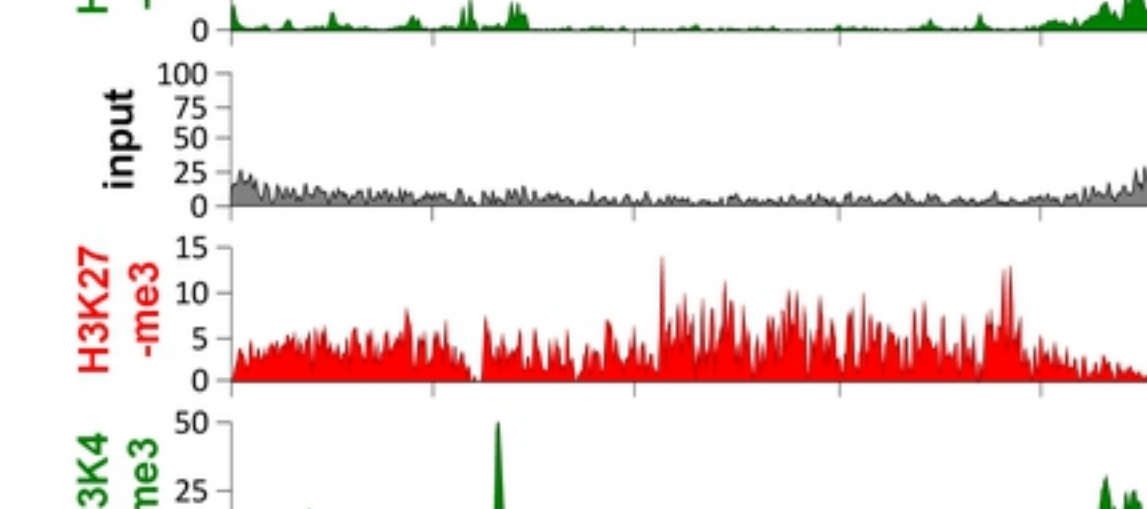

Fig 8

bioRxiv preprint first posted online May. 15, 2019; doi: http://dx.doi.org/10.1101/639898. The copyright holder for this preprint (which was not peer-reviewed) is the author/funder, who has granted bioRxiv a license to display the preprint in perpetuity. It is made available under a CC-BY 4.0 International license.

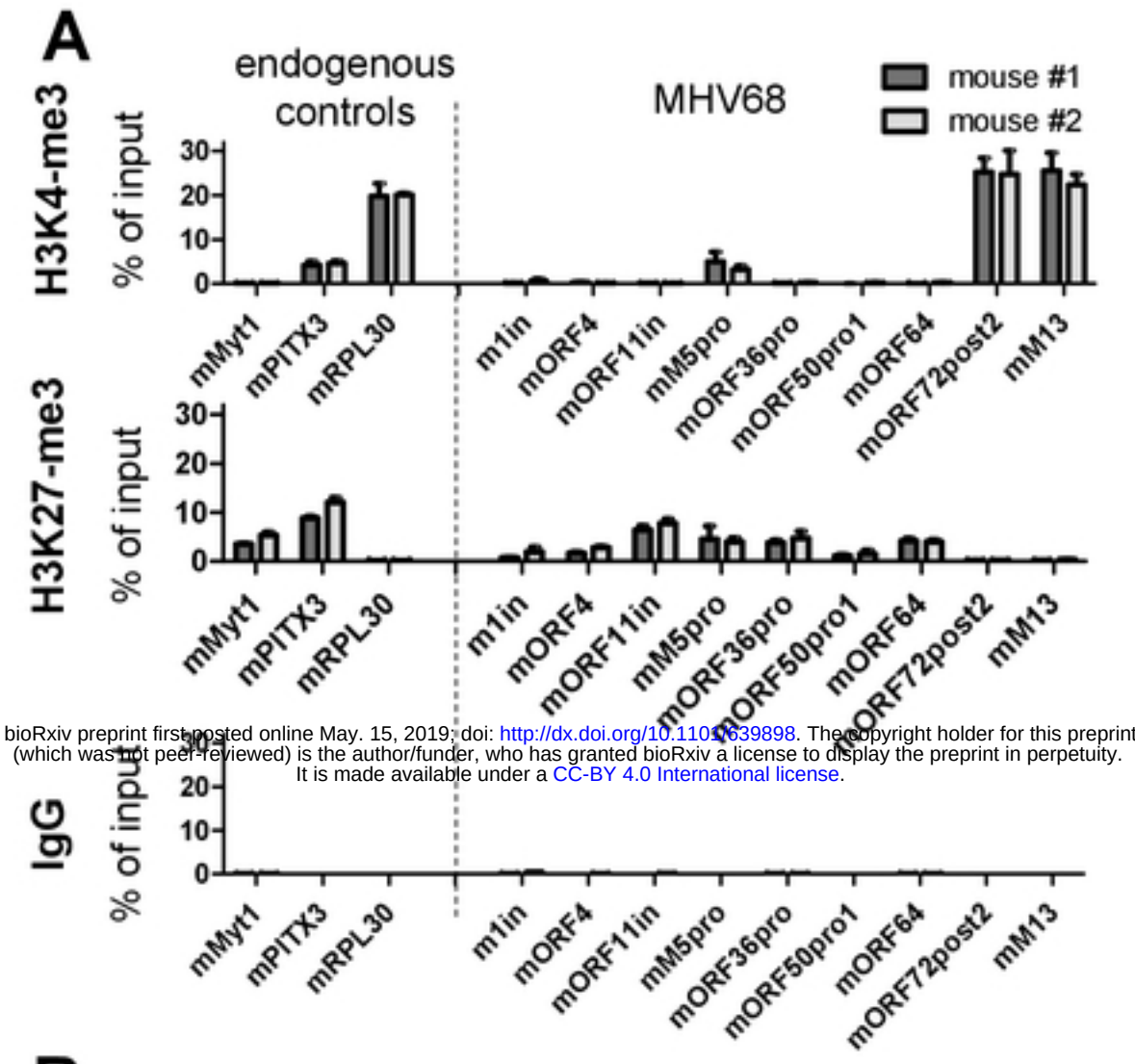

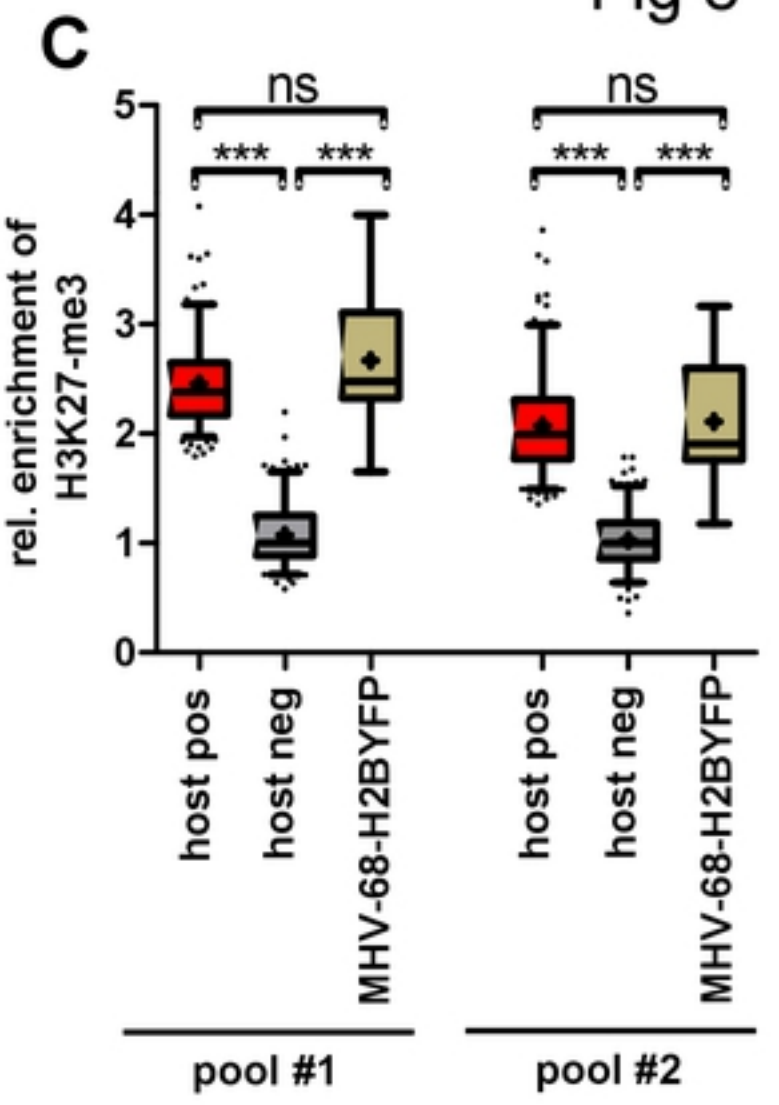

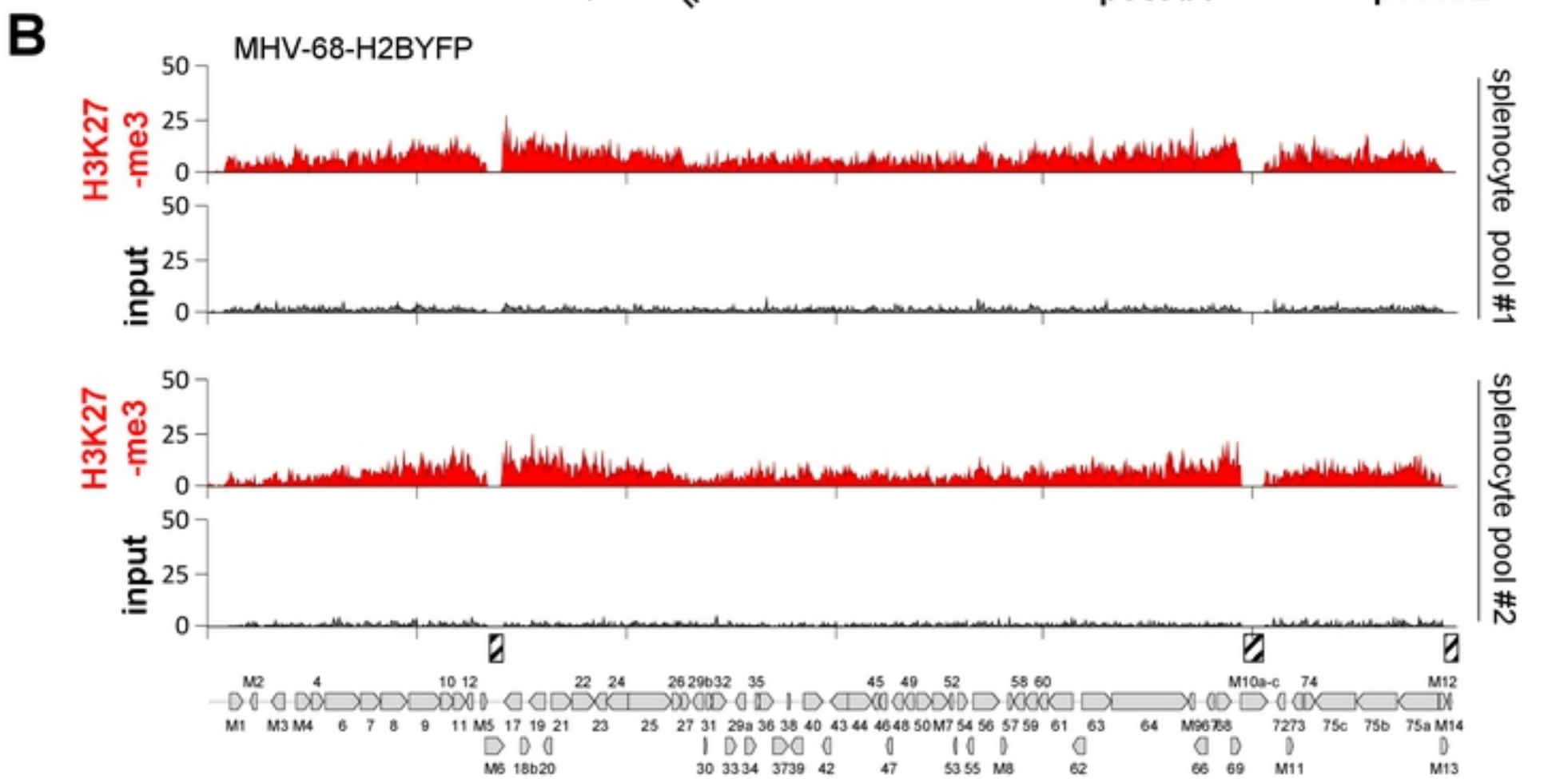

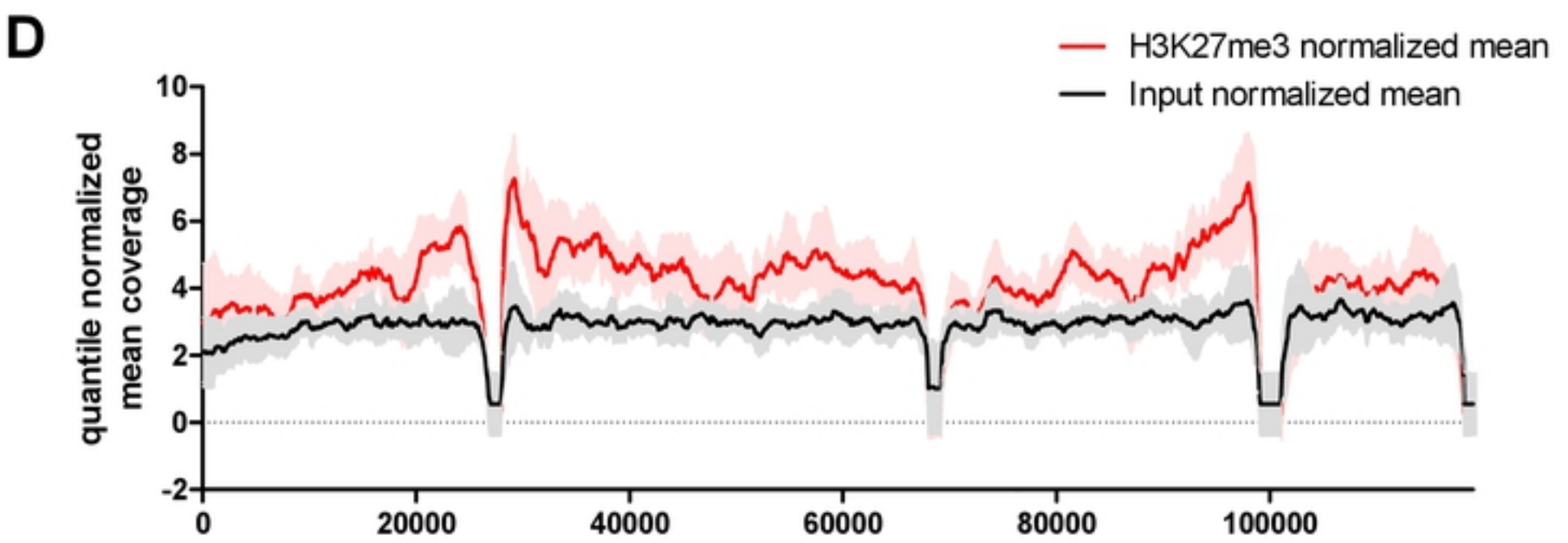

bioRxiv preprint first posted online May. 15, 2019; doi: http://dx.doi.org/10.1101/639898. The copyright holder for this preprint (which was not peer-reviewed) is the author/funder, who has granted bioRxiv a license to display the preprint in perpetuity. It is made available under a CC-BY 4.0 International license.

Fig 9

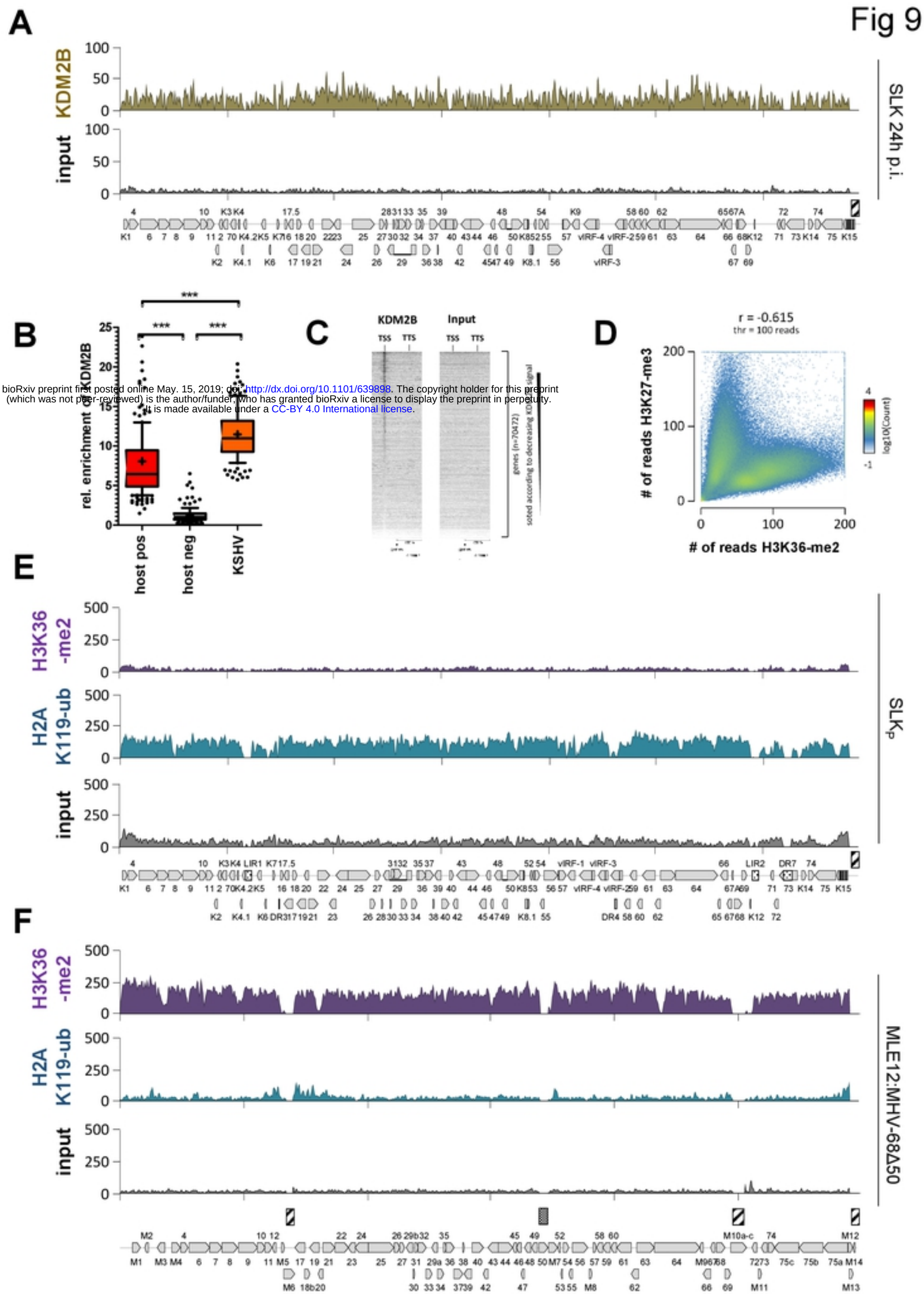

bioRxiv preprint first posted online May. 15, 2019; doi: http://dx.doi.org/10.1101/639898. The copyright holder for this preprint (which was not peer-reviewed) is the author/funder, who has granted bioRxiv a license to display the preprint in perpetuity. It is made available under a CC-BY 4.0 International license.

Fig 9

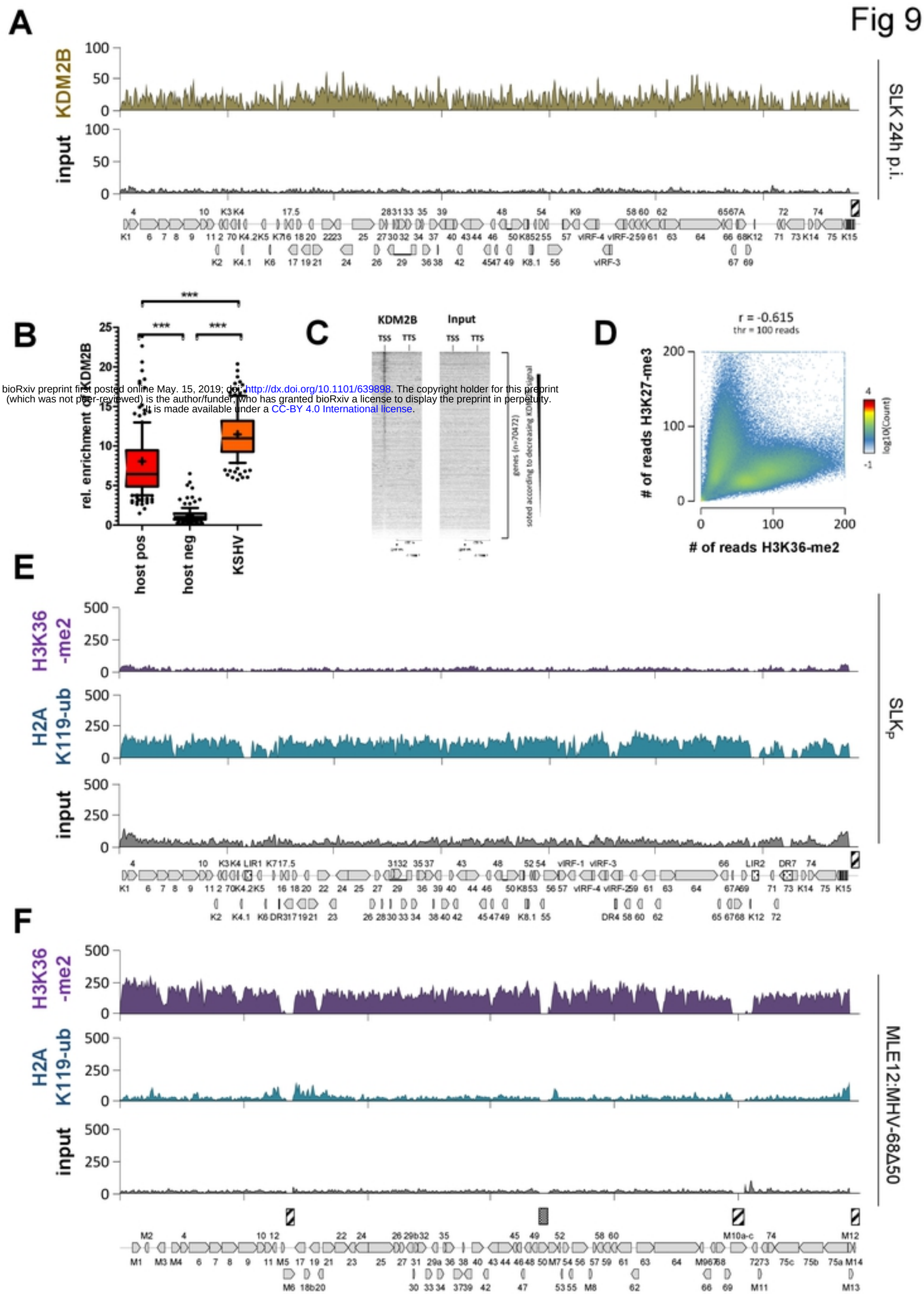

Fig 9
continued

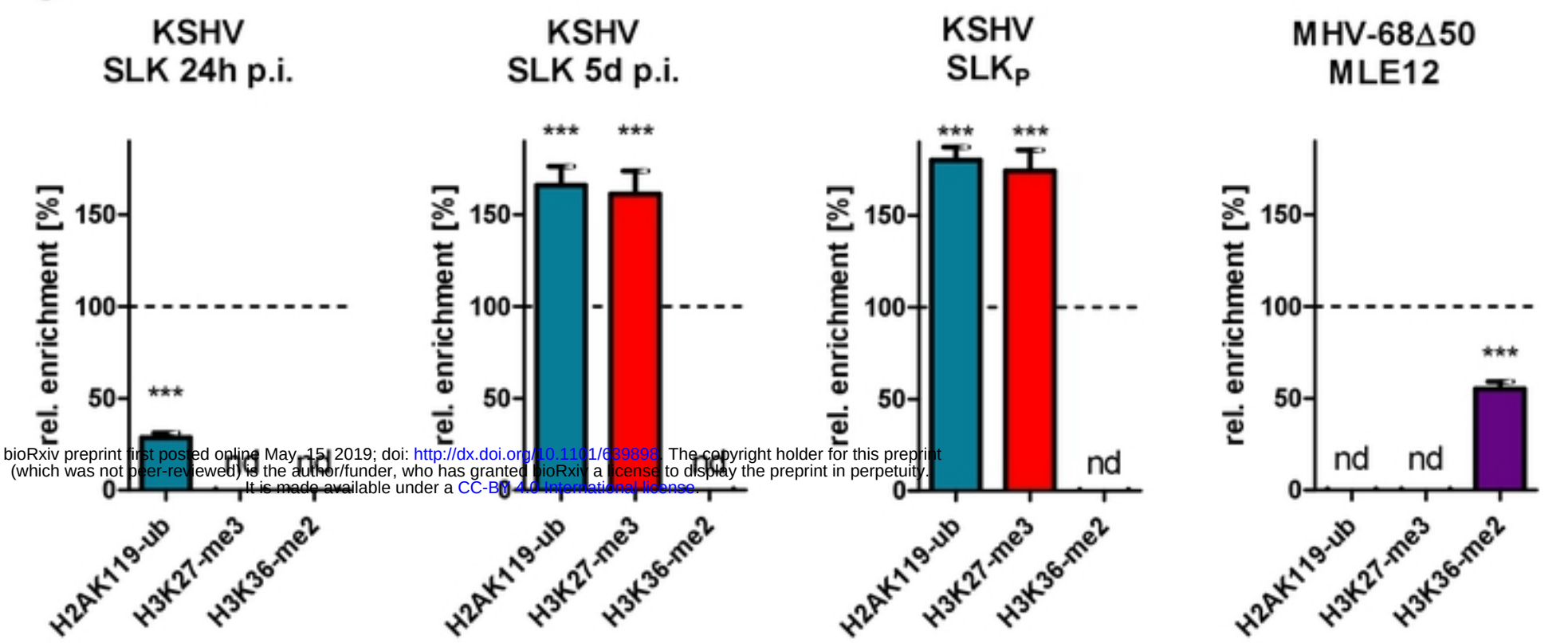

bioRxiv preprint first posted online May. 15, 2019; doi: http://dx.doi.org/10.1101/639898. The copyright holder for this preprint (which was not peer-reviewed) is the author/funder, who has granted bioRxiv a license to display the preprint in perpetuity. It is made available under a CC-BY 4.0 International license.

Fig 10

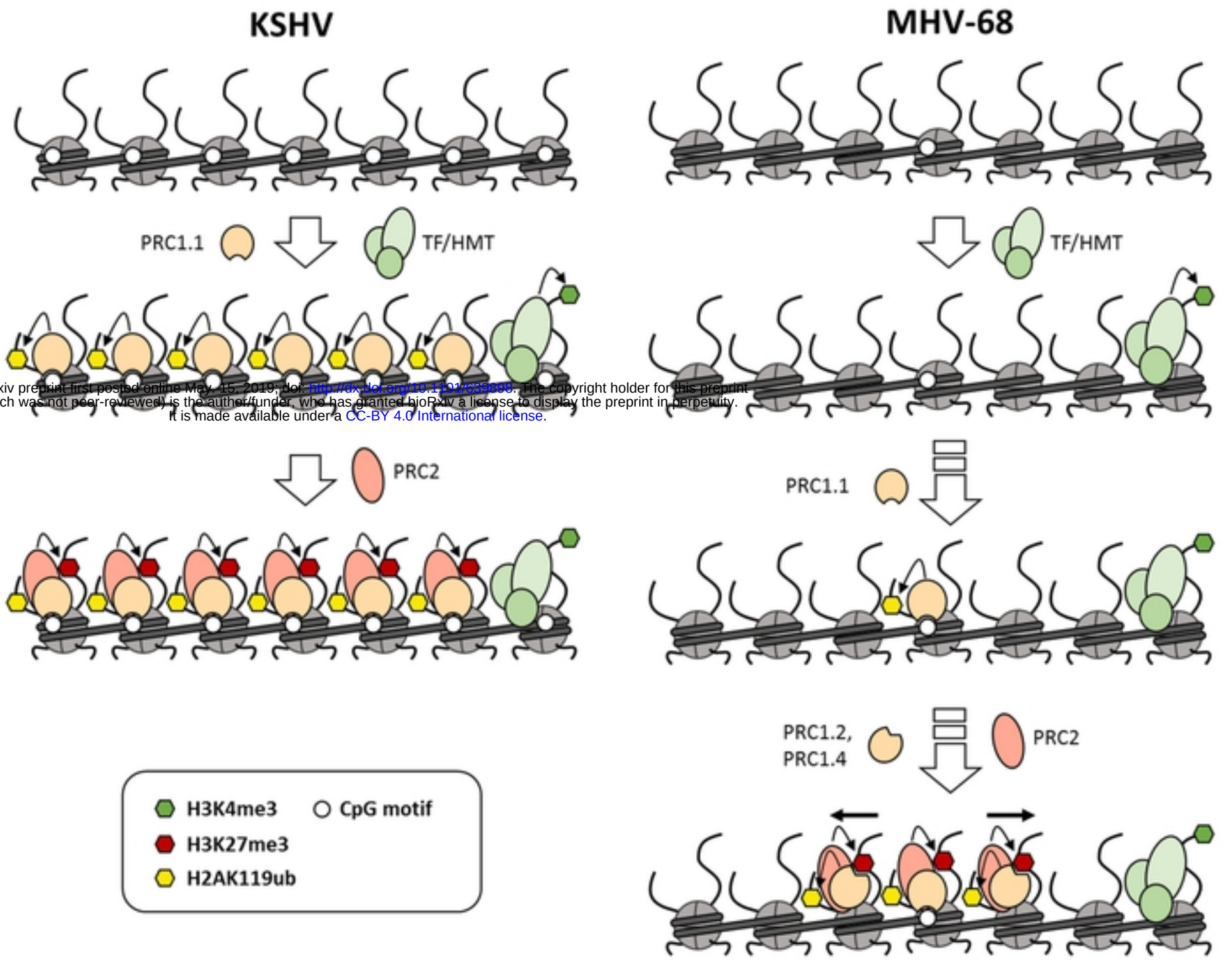

bioRxiv preprint first posted online May. 15, 2019; doi: http://dx.doi.org/10.1101/638898. The copyright holder for this preprint (which was not peer-reviewed) is the author/funder, who has granted bioRxiv a license to display the preprint in perpetuity. It is made available under a CC-BY 4.0 International license.

S1 Fig

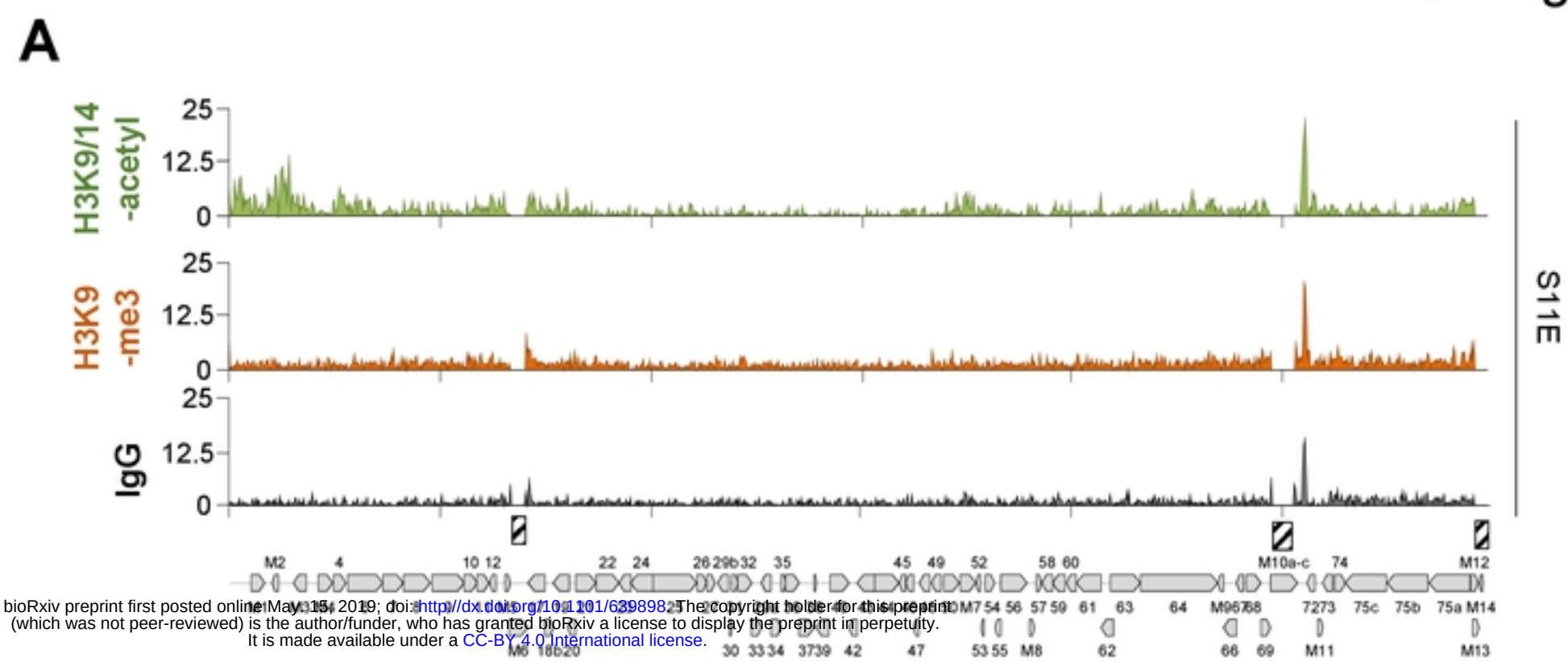

bioRxiv preprint first posted online May. 15, 2019; doi: http://dx.doi.org/10.1101/639898. The copyright holder for this preprint (which was not peer-reviewed) is the author/funder, who has granted bioRxiv a license to display the preprint in perpetuity. It is made available under a CC-BY 4.0 International license.

S2 Fig

bioRxiv preprint first posted online May. 15, 2019; doi: http://dx.doi.org/10.1101/639898. The copyright holder for this preprint (which was not peer-reviewed) is the author/funder, who has granted bioRxiv a license to display the preprint in perpetuity. It is made available under a CC-BY 4.0 International license.

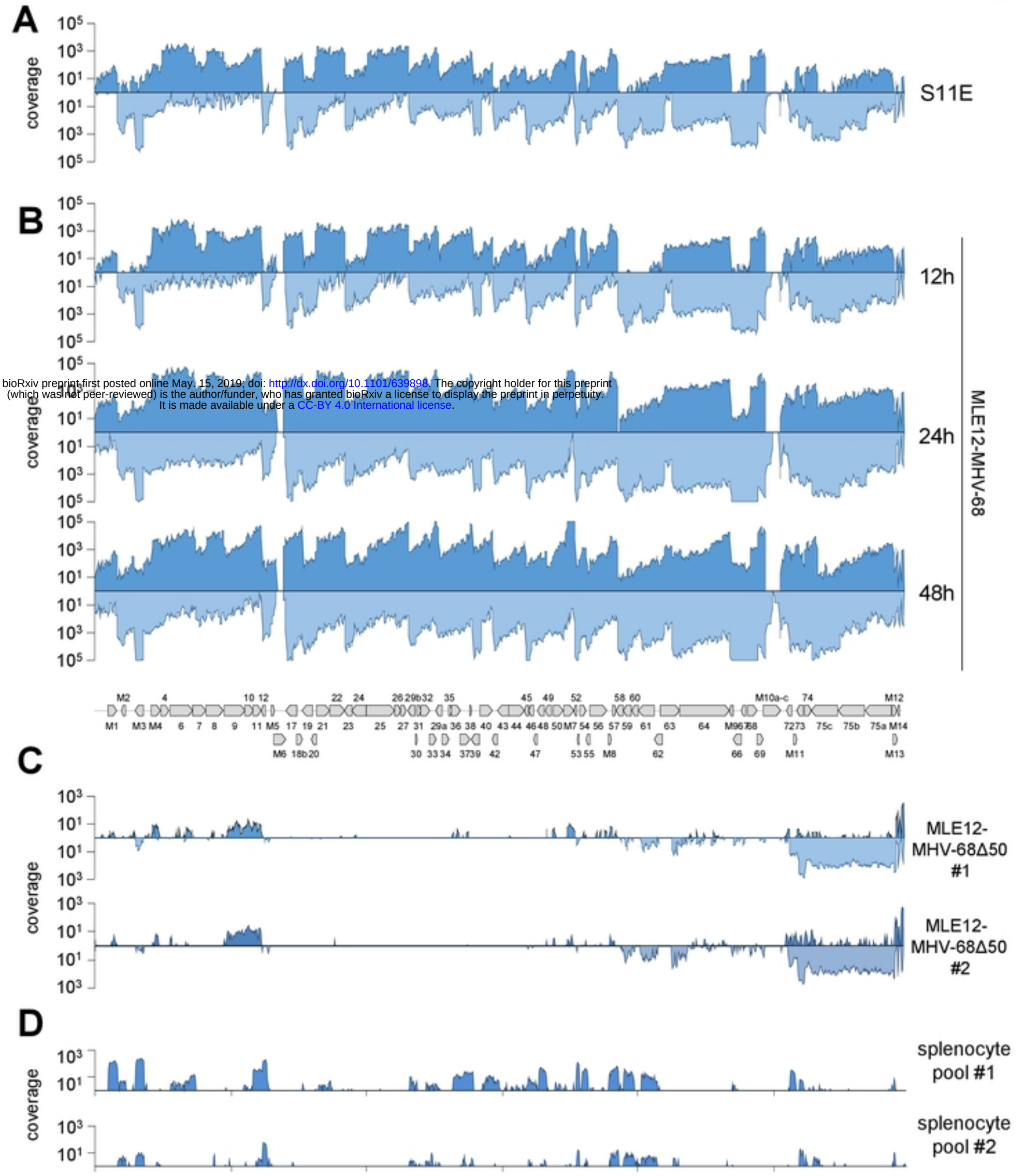

S2 Fig
continued

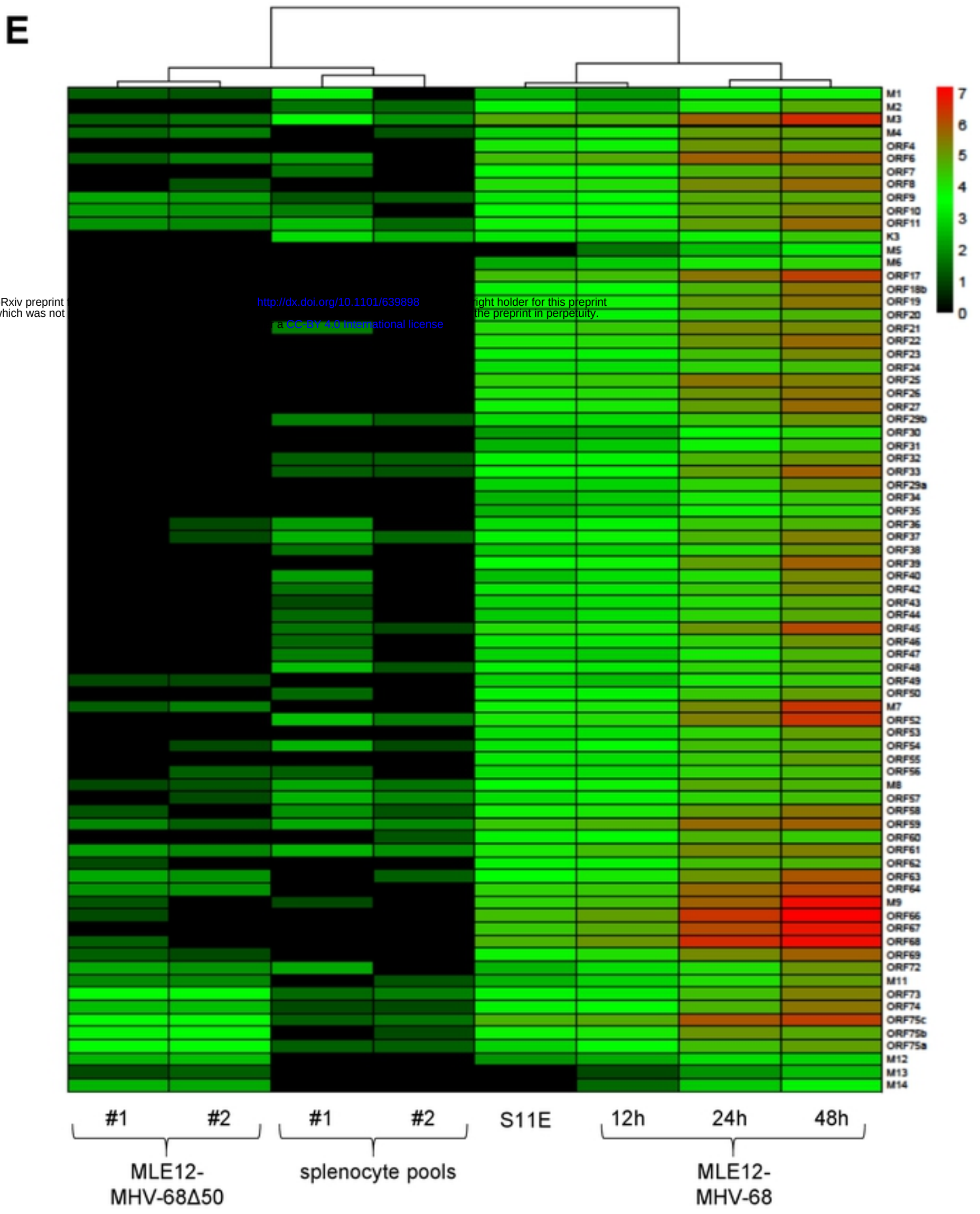

bioRxiv preprint
(which was not
http://dx.doi.org/10.1101/639898
ight holder for this preprint
the preprint in perpetuity.
a CC-BY 4.0 International license

S3 Fig

bioRxiv preprint first posted online May. 15, 2019; doi: http://dx.doi.org/10.1101/630988. The copyright holder for this preprint (which was not peer-reviewed) is the author/funder, who has granted bioRxiv a license to display the preprint in perpetuity. It is made available under a CC-BY 4.0 International license.

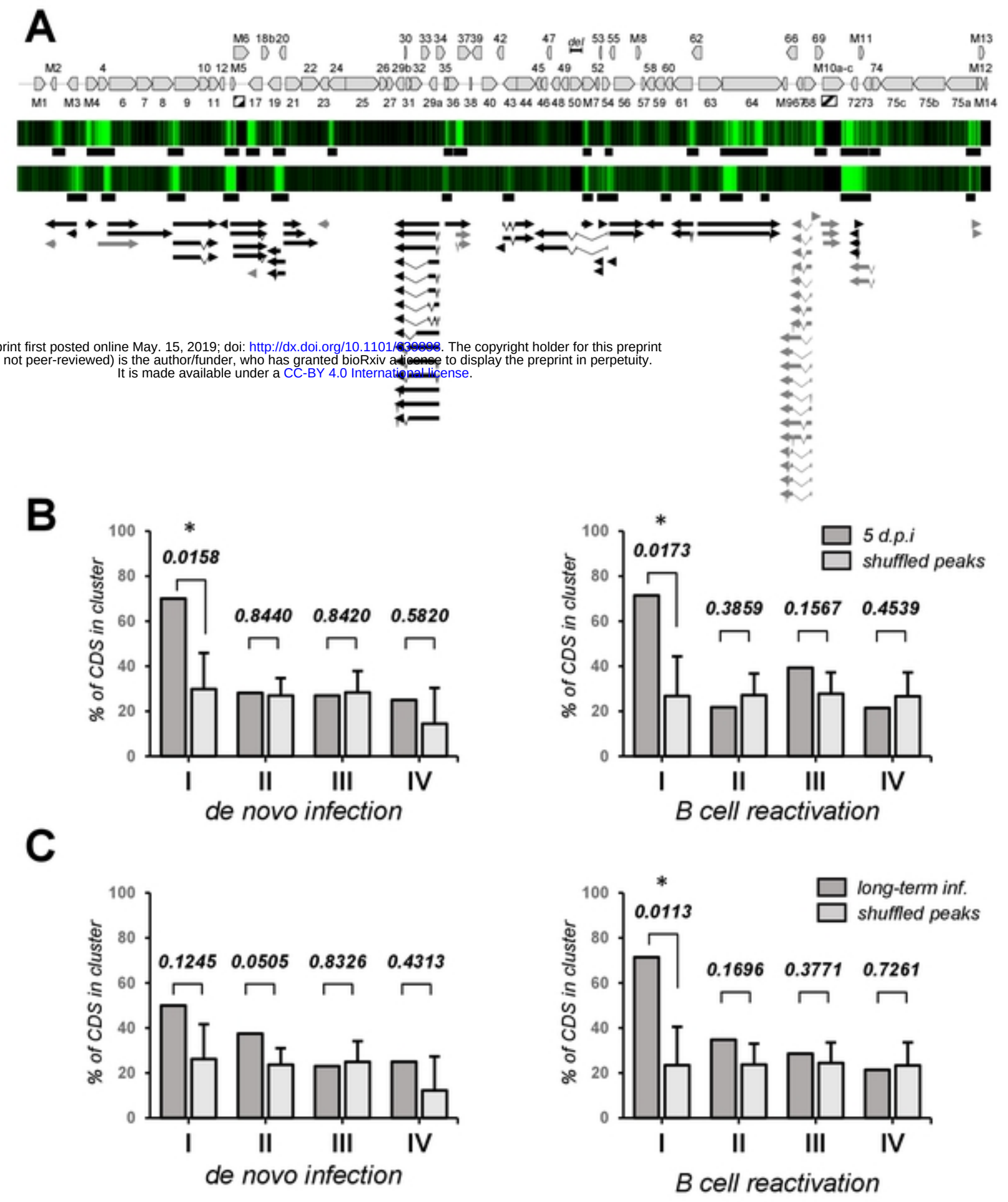

S4 Fig

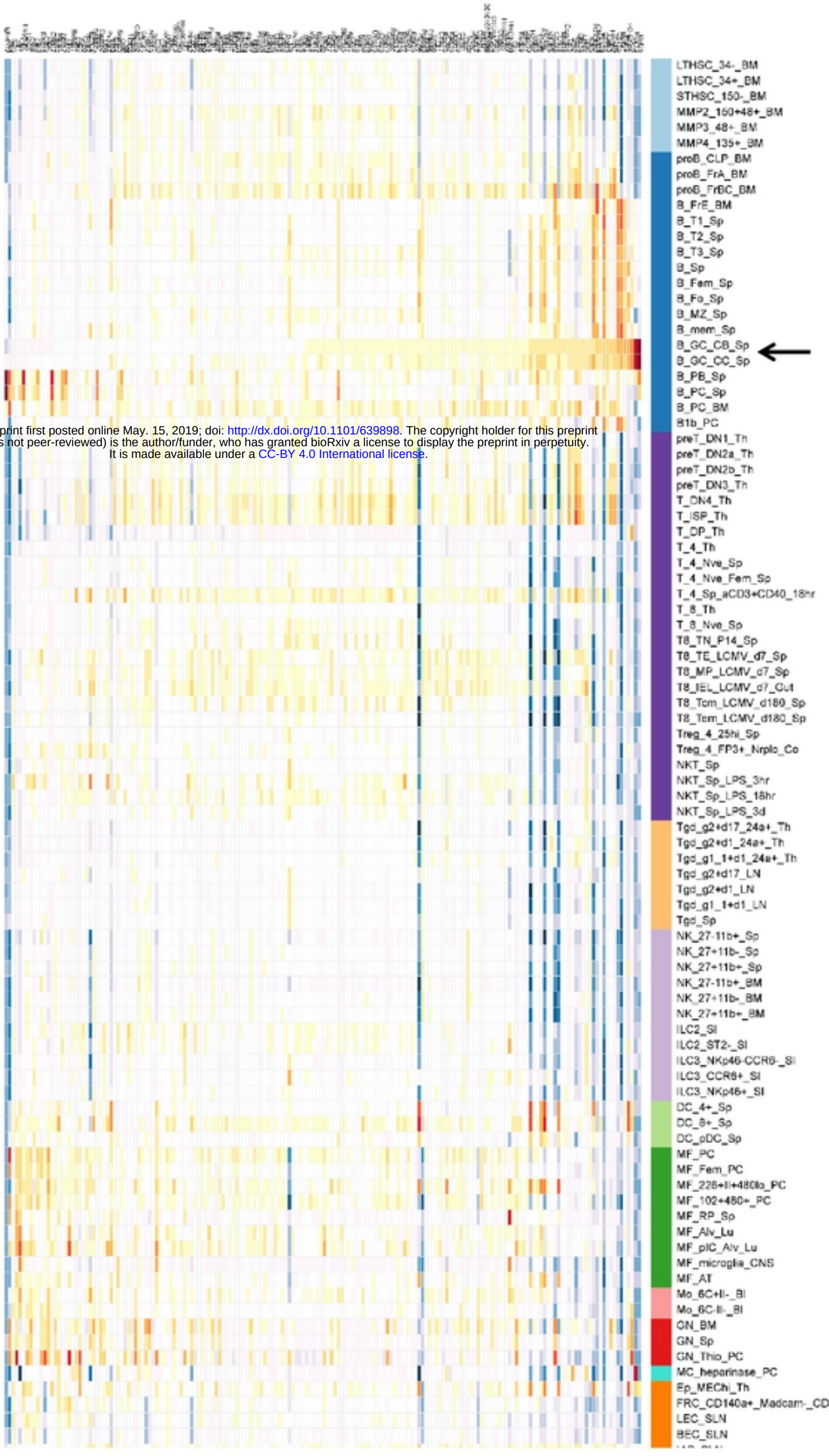

bioRxiv preprint first posted online May. 15, 2019; doi: http://dx.doi.org/10.1101/639898. The copyright holder for this preprint (which was not peer-reviewed) is the author/funder, who has granted bioRxiv a license to display the preprint in perpetuity. It is made available under a CC-BY 4.0 International license.

S5 Fig

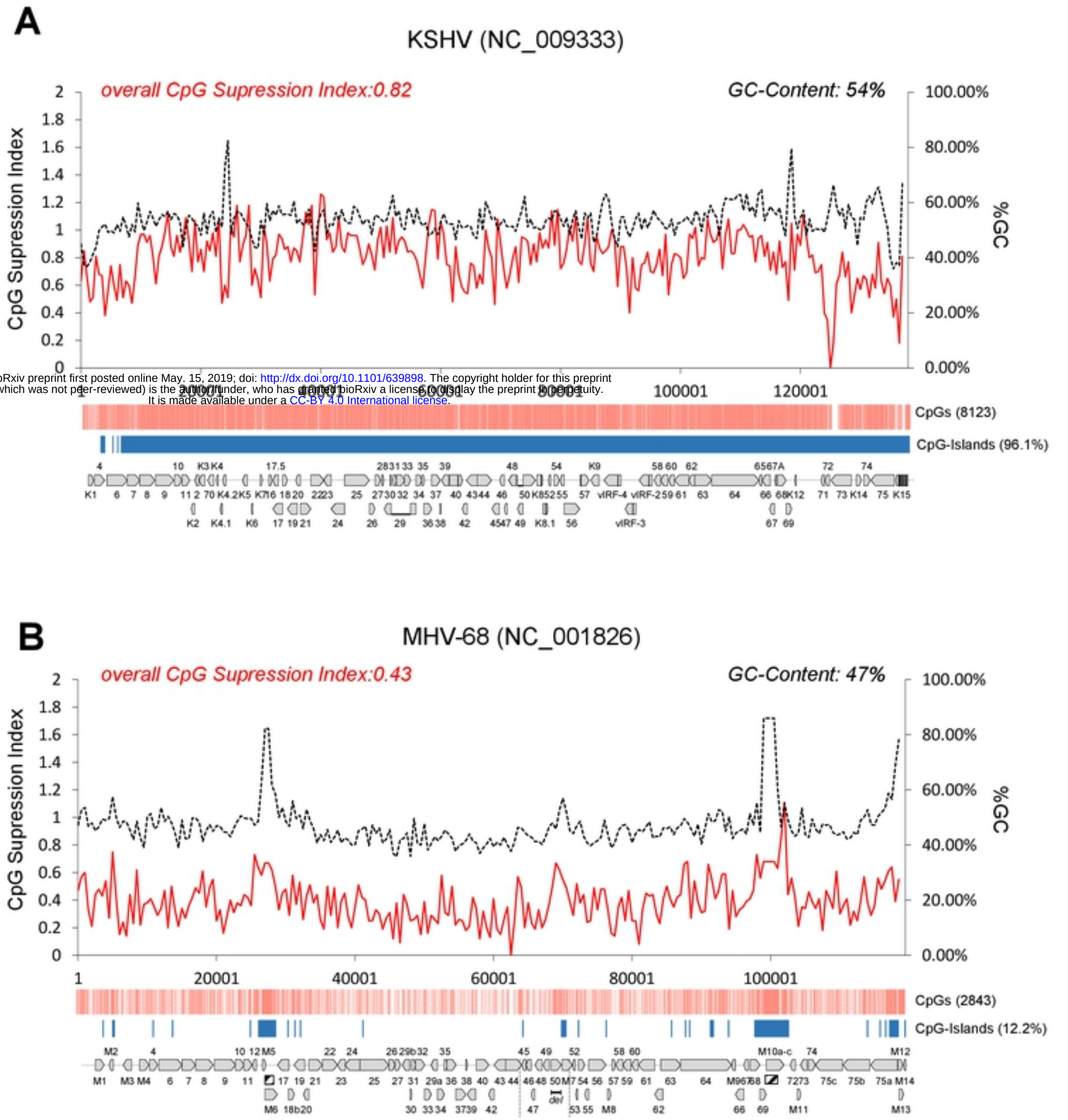

bioRxiv preprint first posted online May. 15, 2019; doi: http://dx.doi.org/10.1101/639898. The copyright holder for this preprint (which was not peer-reviewed) is the author/funder, who has granted bioRxiv a license to display the preprint in perpetuity. It is made available under a CC-BY 4.0 International license.

S6 Fig

bioRxiv preprint first posted online May. 15, 2019; doi: http://dx.doi.org/10.1101/639898. The copyright holder for this preprint (which was not peer-reviewed) is the author/funder, who has granted bioRxiv a license to display the preprint in perpetuity. It is made available under a CC-BY 4.0 International license.

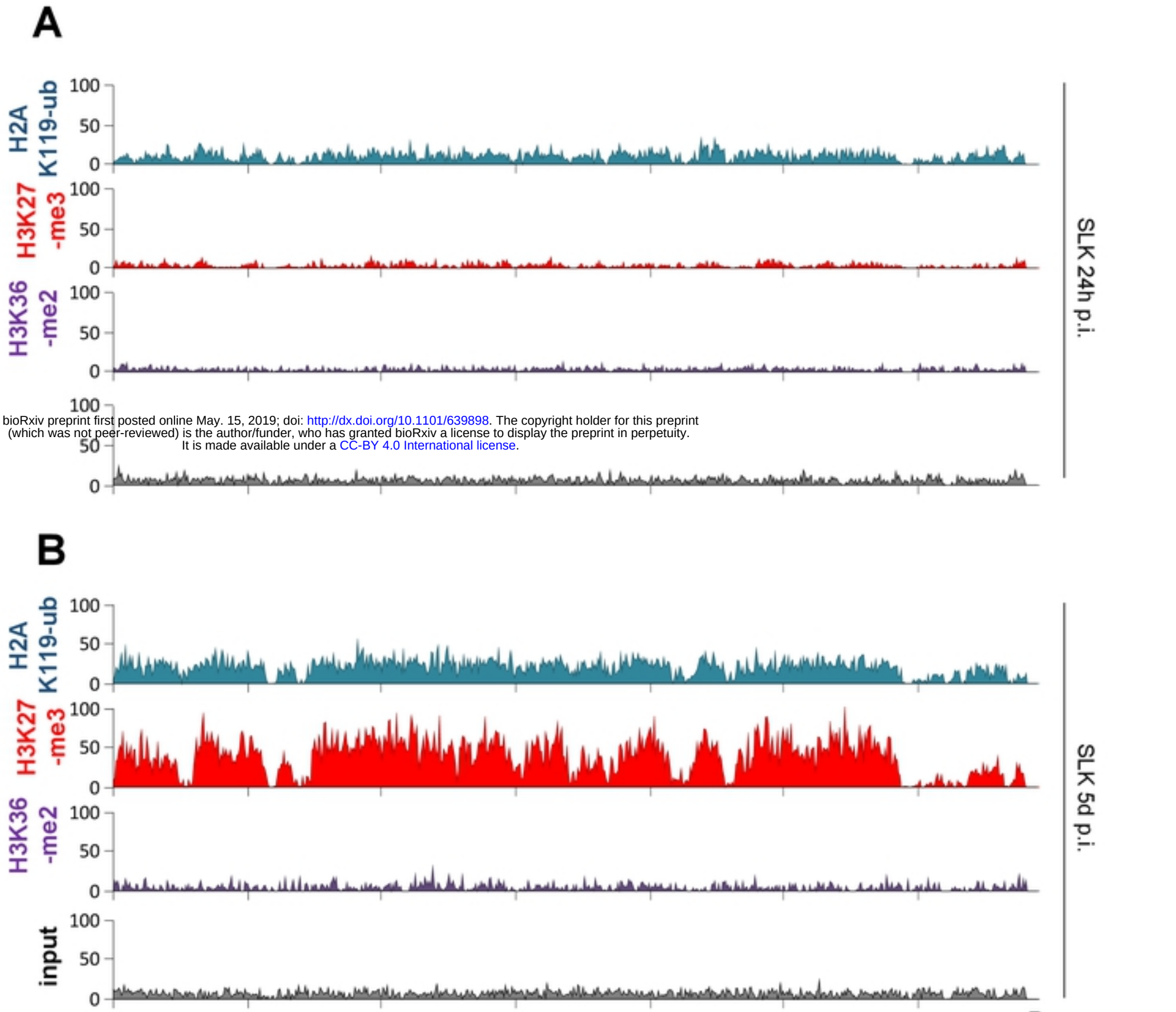

S7 Fig

bioRxiv preprint first posted online May. 15, 2019; doi: http://dx.doi.org/10.1101/639898. The copyright holder for this preprint (which was not peer-reviewed) is the author/funder, who has granted bioRxiv a license to display the preprint in perpetuity. It is made available under a CC-BY 4.0 International license.

KSHV SLK 24h p.i.

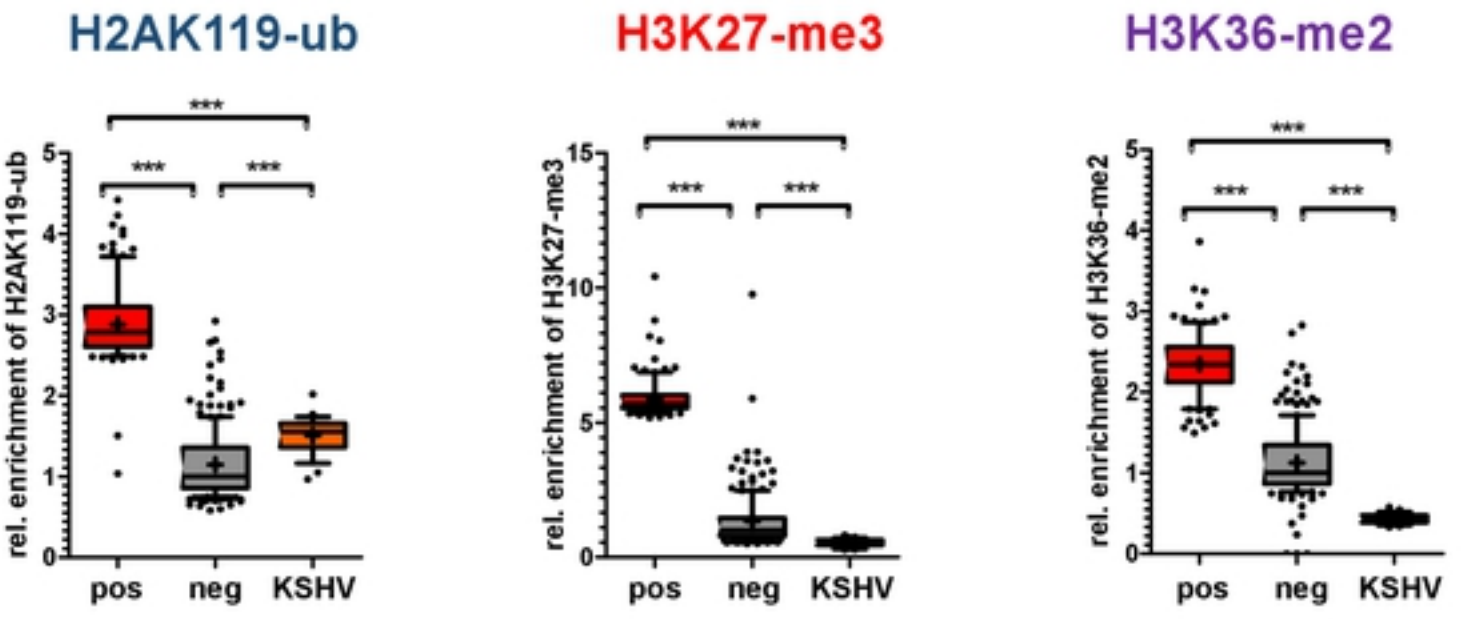

KSHV SLK 5d p.i.

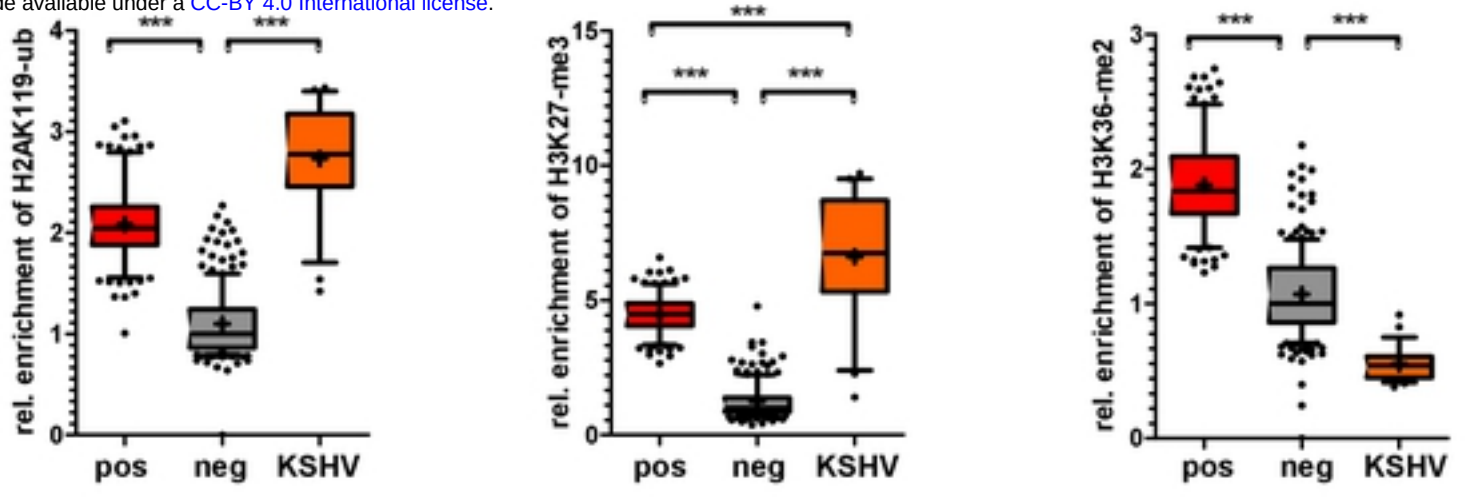

KSHV SLKp

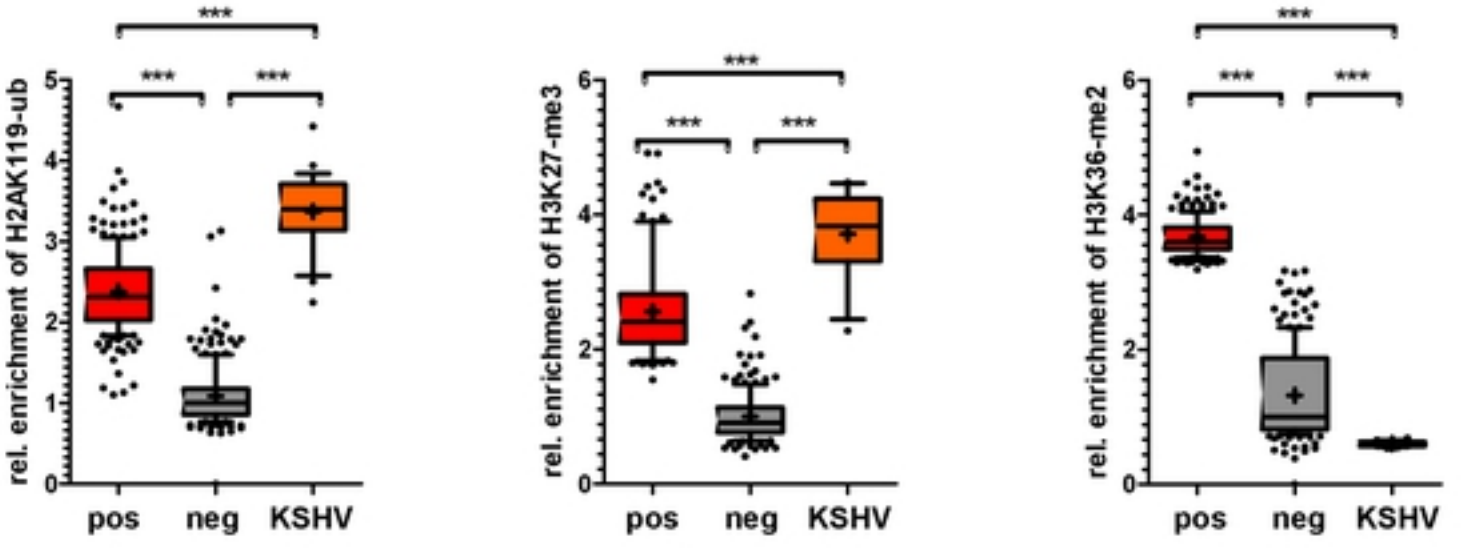

MHV68-Δ50 MLE12

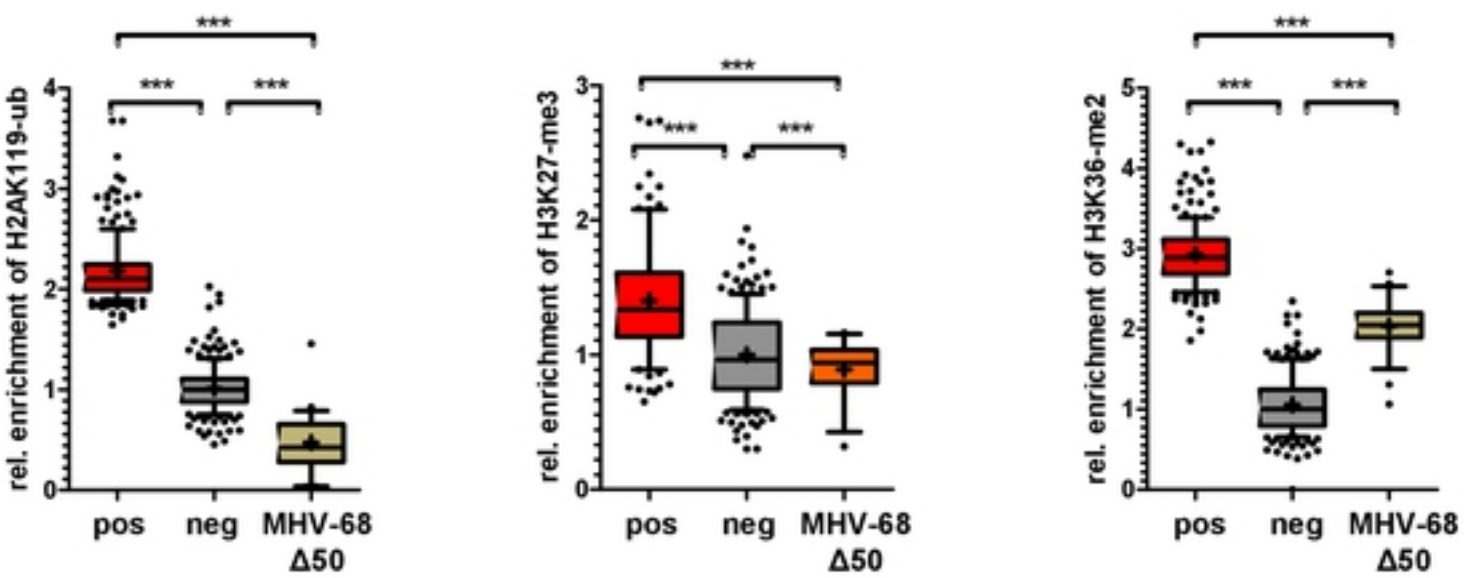

S8 Fig

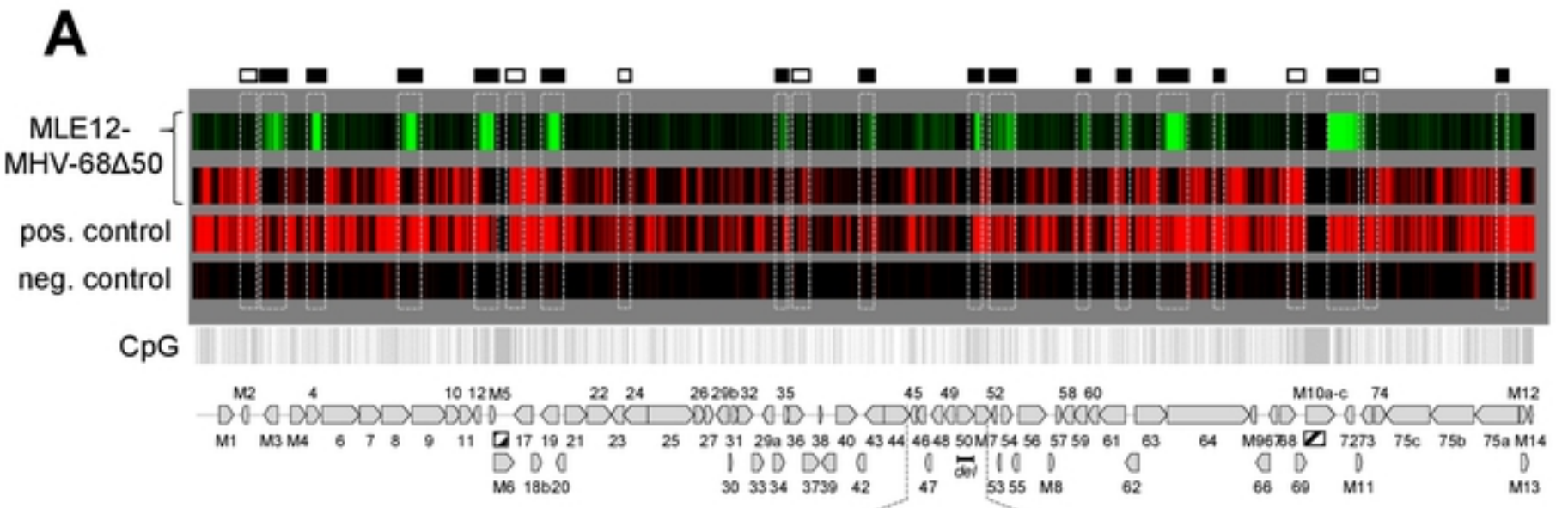

bioRxiv preprint first posted online May. 15, 2019; doi: http://dx.doi.org/10.1101/639898. The copyright holder for this preprint (which was not peer-reviewed) is the author/funder, who has granted bioRxiv a license to display the preprint in perpetuity. It is made available under a CC-BY 4.0 International license.